

Vilde Solberg

# Numerical and experimental investigations of hydrodynamic loads on catamaran type floating solar island

Master's thesis in Marine Technology  
Supervisor: Professor Trygve Kristiansen  
June 2023



Norwegian University of  
Science and Technology



Vilde Solberg

# **Numerical and experimental investigations of hydrodynamic loads on catamaran type floating solar island**

Master's thesis in Marine Technology  
Supervisor: Professor Trygve Kristiansen  
June 2023

Norwegian University of Science and Technology  
Faculty of Engineering  
Department of Marine Technology







DEPARTMENT OF MARINE TECHNOLOGY

MASTER THESIS

---

**Numerical and experimental  
investigations of hydrodynamic  
loads on catamaran type floating  
solar island**

---

*Author:*  
Vilde Solberg

June, 2023

---

# Preface

This thesis is the final work of my Master of Science in Marine Hydrodynamics in Marine Technology (IMT) at the Norwegian University of Science and Technology (NTNU) in Trondheim, Norway.

This thesis investigates the hydrodynamic interaction between two barges, simulating catamaran-shaped floaters, in forced harmonic oscillatory flow. The topic has relevance towards multi-modular floating solar islands, where the hydrodynamic interaction between the pontoons due to waves, current, and wind is expected. There is sparse knowledge of this topic, and the industrial and academic relevance is a strong motivation. Solar energy has the potential to be an essential part of the transition to green energy. Before the solar islands can be implemented in commercial green energy farming, the significant environmental loads affecting the structure must be accounted for.

---

## Acknowledgments

I want to thank the many people who have offered their generous assistance and guidance while writing this Master's Thesis.

First of all, I would like to express my deep gratitude to my supervisor Professor Trygve Kristiansen. He has been nothing but encouraging throughout the entire semester. His knowledge and enthusiasm regarding this field has been of the most appreciated. Trygve Kristiansen has shaped the scope of my research and provided invaluable insight that has contributed to the quality and depth of this work. He has provided intriguing discussions and challenged my way of thinking. This semester would be significantly more challenging without his guidance.

Next, I would like to thank the team that has made the experimental part of this thesis possible. Robert Opland, Terje Rosten, Trond Innset and Ole Erik Vinje. Each member of this team has contributed with their expertise and made the experiment of top quality. Their generous help and knowledge have been utmost crucial to the success of my experiment.

I would also like to thank Ph.D. candidate Maël Korentin Ivan Moreau for guidance and expertise related to my numerical work. He has provided insight and valuable help in learning new software.

Finally, I would like to thank my good friends at office B.366, Sophie Holme Stokker and Marie Schrader Bordal, for helpful discussions, laughter, and encouragement. The process of writing would not have been the same without you.

# Abstract

There is an increasing demand for clean energy, and floating solar islands can be a sufficient solution to contribute to this. In writing time, most floating solar installations are situated in sheltered areas, such as near shorelines, dams, or lakes, benefiting from relatively mild weather conditions. This allows for simpler structures as it experiences lighter weather conditions. However, there is a growing interest in deploying these floating structures in more exposed areas, necessitating a comprehensive investigation into their hydrodynamic behavior.

The presented work, investigates the hydrodynamic forces between catamaran-shaped floaters in harmonic oscillatory flow in three dimensions. Both numerical and experimental analysis is conducted. Specifically, the investigation explores the effect of two factors: the increased gap distance between the catamaran models and the increased draft.

The numerical analysis is performed using the numerical solver WAMIT. Three gap distance configurations and two height configurations are tested. The results are converted to nondimensional values and presented across a range of Kaulegan-Carpenter (KC) numbers. The numerical analysis is based on potential flow theory, assuming ideal fluid.

The experiment is conducted in the Lader tank at the Center of Marine Technology in Trondheim, Norway. This experiment investigates the hydrodynamic forces of catamaran-shaped models in oscillating flow. Three gap distance configurations and two height configurations are tested. The numerical and experimental findings are then briefly compared to a summary of a previous experiment conducted in the Autumn of 2022, which studied various square-shaped cylinder configurations under oscillating flow conditions.

The numerical results are compared with the DNV standard '*DNV-RP-C205*' and evaluated with respect to estimated sloshing modes. Lastly, highlights for scaling to full-scale structures are discussed.

This master's thesis aims to comprehensively and thoroughly investigate the hydrodynamic interactions affecting catamaran-shaped floaters. The findings contribute to a better understanding of the floating solar island dynamics.

# Sammendrag

Det er en økende etterspørsel etter grønn energi. Flytende soløyer kan være en potensiell kilde til å bidra til dette. I skrivende tid, er de fleste flytende soløykonstruksjonene plassert i beskyttede områder, eksempelvis nær kystlinjer, demninger eller innsjøer. Disse lokasjonene kan nytte av relativt milde værforhold. Dette tillater enklere strukturer, da de utsettes for mildere værforhold. Imidlertid er det økende interesse for å implementere disse flytende strukturene i mer utsatte områder, noe som krever en grundig undersøkelse av deres hydrodynamiske atferd.

Det presenterte arbeidet undersøker de hydrodynamiske kreftene mellom katamaranformede flotasjonslegemer i harmonisk oscillerende strøm tredimensjonalt. Både numeriske og eksperimentelle analyser er utført. Spesielt er fokuset på effekten av to følgende faktorer: økt avstand mellom katamaranmodellene og økt neddykking av katamaranen.

Den numeriske analysen utføres ved hjelp av det numeriske løsningsprogrammet WAMIT. Tre konfigurasjoner av avstand mellom flotasjonslegemene for to høydekonfigurasjoner testes. Resultatene konverteres til dimensjonsløse verdier og presenteres over en rekke Kaulegan-Carpenter (KC)-numre. Den numeriske analysen er basert på potensialstrømteori og forutsetter ideell væske.

Eksperimentet er utført i Lader-tanken ved Senter for Marin Teknologi i Trondheim, Norge. Dette eksperimentet undersøker de hydrodynamiske kreftene på katamaranformede modeller i oscillerende strøm. Tre konfigurasjoner av avstand mellom flyterne med to høydekonfigurasjoner testes. De numeriske og eksperimentelle resultatene blir deretter sammenlignet i korte trekk med en oppsummering av et tidligere eksperiment gjennomført om høsten 2022, som studerte ulike konfigurasjoner av kvadratiske sylindere under oscillerende strømforhold.

De numeriske resultatene sammenlignes med DNV-standarden "DNV-RP-C205" og vurderes med hensyn til estimerte sloshing-moder. Til slutt diskuteres høydepunkter for skalering til fullskalastrukturer.

Denne masteroppgaven har som mål å gi en grundig og omfattende undersøkelse av de hydrodynamiske interaksjonene som påvirker katamaranformede flotasjonslegemer. Funnene bidrar til en bedre forståelse av dynamikken til flytende soløyer.

# Nomenclature

|           |                                      |
|-----------|--------------------------------------|
| $\beta$   | Ratio                                |
| $\eta_a$  | Amplitude of oscillation             |
| KC        | Keulegan-Carpenter number            |
| Re        | Reynolds number                      |
| $\mu$     | Dynamic viscosity                    |
| $\nu$     | Kinematic viscosity                  |
| $\omega$  | Natural frequency/Harmonic frequency |
| $\rho$    | Fluid density                        |
| $\varphi$ | Velocity potential                   |
| $\xi$     | Body motions                         |
| $\zeta_a$ | Wave amplitude                       |
| $A$       | Added mass force                     |
| $a_w$     | Acceleration                         |
| $B$       | Damping force                        |
| $B$       | Width                                |
| $b$       | Gap distance                         |
| $B_q$     | Quadratic damping                    |
| $C_A$     | Added mass coefficient               |
| $C_B$     | Damping coefficient                  |
| $C_D$     | Drag coefficient                     |
| $D$       | Characteristic length                |
| $F$       | Force                                |
| $f$       | Frequency [Hz]                       |

---

|            |                            |
|------------|----------------------------|
| $F^\omega$ | Harmonic force             |
| $g$        | Gravitational acceleration |
| $H$        | Height of draft            |
| $I_{ij}$   | Moment of inertia          |
| $k$        | Stiffness                  |
| $L$        | Length                     |
| $L^k$      | ULEN-parameter             |
| $m$        | Mass or meter              |
| $r_{ij}$   | Radii of gyration          |
| $S_b$      | Mean wetted surface area   |
| $S_f$      | Spectral density           |
| $T$        | Period                     |
| $u$        | Fluid velocity vector      |
| $U_m$      | Amplitude velocity         |
| $u_w$      | Velocity                   |

# Table of Contents

|          |  |           |
|----------|--|-----------|
| <b>1</b> | <b>Introduction</b>  | <b>1</b>  |
| 1.1      | Motivation . . . . .   | 1         |
| 1.2      | Literature review . . . . .                                    | 3         |
| 1.3      | Previous Work - Project Thesis . . . . .                       | 5         |
| 1.4      | Scope of Work and Objectives . . . . .                         | 5         |
| <b>2</b> | <b>Theory</b>  | <b>7</b>  |
| 2.1      | Terminology . . . . .  | 7         |
| 2.1.1    | The multi-modular concept . . . . .                            | 8         |
| 2.2      | Governing equations . . . . .                                  | 9         |
| 2.2.1    | Navier-Stokes equation . . . . .                               | 9         |
| 2.2.2    | Bernoulli and Laplace . . . . .                                | 9         |
| 2.3      | Parameters and coefficients . . . . .                          | 9         |
| 2.4      | Hydrodynamic force . . . . .                                   | 10        |
| 2.4.1    | Exciting forces of a submerged body . . . . .                  | 11        |
| 2.4.2    | Exciting forces of a submerged catamaran-shaped body . . . . . | 12        |
| 2.4.3    | Damping . . . . .  | 12        |
| 2.4.4    | The Morison equation . . . . .                                 | 13        |
| 2.4.5    | Sloshing modes . . . . .                                       | 13        |
| 2.5      | Nondimensionalization . . . . .                                | 14        |
| <b>3</b> | <b>Experiment</b>  | <b>15</b> |
| 3.1      | The Lader tank - Lab facilities . . . . .                      | 15        |



---

|          |   |           |
|----------|---|-----------|
| 3.2      | Previous work - square-shaped cylinders . . . . .     | 16        |
| 3.2.1    | Model description . . . . .                           | 16        |
| 3.2.2    | Test program - Cylinders . . . . .                    | 17        |
| 3.2.3    | Summary of the findings . . . . .                     | 18        |
| 3.3      | Experimental setup . . . . .                          | 19        |
| 3.3.1    | The test rig . . . . .                                | 19        |
| 3.3.2    | Model description - Catamarans . . . . .              | 20        |
| 3.3.3    | Test program - Catamarans . . . . .                   | 22        |
| 3.4      | Instrumentation and Calibration . . . . .             | 22        |
| 3.4.1    | Calibration of sensors . . . . .                      | 23        |
| 3.4.2    | Hammer test . . . . .                                 | 23        |
| 3.5      | Sources of Error . . . . .                            | 23        |
| <b>4</b> | <b>Numerical analysis</b>                             | <b>25</b> |
| 4.1      | WAMIT . . . . .                                       | 25        |
| 4.2      | Theory . . . . .                                      | 27        |
| 4.2.1    | The boundary-value problem in WAMIT . . . . .         | 27        |
| 4.2.2    | Added mass and damping coefficients . . . . .         | 27        |
| 4.2.3    | Exciting forces . . . . .                             | 28        |
| 4.2.4    | Body motion and free surface elevation . . . . .      | 28        |
| 4.3      | Input and output files . . . . .                      | 28        |
| 4.3.1    | Mesh and the <i>'gdf'</i> input file . . . . .        | 29        |
| 4.3.2    | Mass matrix and the <i>'frc'</i> input file . . . . . | 30        |
| 4.4      | Refinement study . . . . .                            | 31        |
| 4.4.1    | Mesh refinement . . . . .                             | 32        |
| 4.4.2    | Wave refinement . . . . .                             | 33        |
| 4.5      | Verification of numerical results . . . . .           | 34        |
| 4.5.1    | Sloshing modes . . . . .                              | 34        |
| 4.5.2    | Added mass DNV . . . . .                              | 35        |

---

|          |  |           |
|----------|--|-----------|
| <b>5</b> | <b>Post-Processing</b>                     | <b>37</b> |
| 5.1      | Hammer test . . . . .                      | 37        |
| 5.1.1    | Comparing outer and inner plate . . . . .  | 38        |
| 5.1.2    | Empty plate . . . . .                      | 38        |
| 5.1.3    | Small- and large-draft models . . . . .    | 39        |
| <b>6</b> | <b>Result and discussion</b>               | <b>41</b> |
| 6.1      | Numerical analysis - WAMIT . . . . .       | 41        |
| 6.1.1    | Added mass coefficient . . . . .           | 42        |
| 6.1.1.1  | Small-draft models . . . . .               | 42        |
| 6.1.1.2  | Large-draft models . . . . .               | 43        |
| 6.1.2    | Damping coefficients . . . . .             | 44        |
| 6.1.2.1  | small-draft models . . . . .               | 44        |
| 6.1.2.2  | Large-draft models . . . . .               | 45        |
| 6.1.3    | Exciting forces . . . . .                  | 45        |
| 6.1.3.1  | Case 1 - small-draft models . . . . .      | 46        |
| 6.2      | Experimental results . . . . .             | 48        |
| 6.2.1    | Added mass and drag coefficients . . . . . | 49        |
| 6.2.1.1  | Small-draft models . . . . .               | 50        |
| 6.2.1.2  | Large-draft models . . . . .               | 51        |
| 6.2.2    | Higher $\omega$ -forces . . . . .          | 53        |
| 6.2.2.1  | Small-draft models . . . . .               | 53        |
| 6.2.2.2  | Large-draft models . . . . .               | 54        |
| 6.3      | Additional notes . . . . .                 | 56        |
| 6.3.1    | Full scale . . . . .                       | 56        |
| <b>7</b> | <b>Conclusion and further work</b>         | <b>58</b> |
| 7.1      | Conclusions . . . . .                      | 58        |
| 7.2      | Further work . . . . .                     | 59        |
| <b>A</b> | <b>Literature review</b>                   | <b>63</b> |

---

---

|          |   |           |
|----------|---|-----------|
| A.1      | Pannell, Griffiths and Coales circular wire experiment . . . . .  | 63        |
| A.2      | Biermann and Herrnstein wind tunnel experiment . . . . .  | 64        |
| A.3      | Hori's experiment on the pressure disturbance around two cylinders .  | 65        |
| A.4      | Garbis H. Keulegan and Lloyd H. Carpenter's figure for drag<br>coefficient form their experimental and numerical study of <i>forces on<br/>cylinders and plated in an oscillating fluid</i> . . . . . | 66        |
| A.5      | Onsrud's Master thesis model . . . . .  | 67        |
| A.6      | Fredrik Mentzoni's added mass and damping coefficients form his<br>paper: <i>numerical modeling of perforated plates in oscillating flow</i> . . .  | 68        |
| <b>B</b> | <b>The calculation of exciting forces of a submerged body</b>   | <b>69</b> |
| B.1      | Foude Krylov force . . . . .  | 69        |
| B.2      | Diffraction force . . . . .   | 70        |
| <b>C</b> | <b>A visualization of grids used in WAMIT</b>   | <b>72</b> |
| C.1      | Grid refinement G2, large-draft model . . . . .   | 72        |
| C.2      | Grid refinement G4, large-draft model . . . . .   | 73        |
| C.3      | Grid refinement G8, large-draft model . . . . .   | 73        |
| C.4      | Grid refinement G15, large-draft model . . . . .  | 74        |
| C.5      | Grid refinement G22, large-draft model . . . . .  | 74        |
| <b>D</b> | <b>Using DNV-RP-C205 to calculating added mass coefficient</b>  | <b>75</b> |
| D.1      | Calculation procedure . . . . .   | 76        |
| D.2      | Correcting for 3-dimensional effects . . . . .  | 77        |
| D.3      | Summary . . . . .   | 77        |
| <b>E</b> | <b>Added mass coefficients in 6 Degrees Of Freedom (DOF)</b>  | <b>78</b> |
| E.1      | Small-draft models . . . . .  | 78        |
| E.2      | Large-draft models . . . . .  | 81        |
| <b>F</b> | <b>Damping coefficients in 6 Degrees Of Freedom (DOF)</b>   | <b>85</b> |
| F.1      | Small-draft models . . . . .  | 85        |
| F.2      | Large-draft models . . . . .  | 88        |

---

---

|          |  |            |
|----------|--|------------|
| <b>G</b> | <b>Exciting forces</b>   | <b>92</b>  |
| G.1      | Small-draft models . . . . .   | 92         |
| G.2      | Large-draft models . . . . .   | 96         |
| <b>H</b> | <b>Force component, <math>F^\omega</math>s with unit Newton [N]</b>  | <b>99</b>  |
| H.1      | Case 1, small-draft models . . . . .   | 99         |
| H.2      | Case 1, large-draft models . . . . .   | 100        |
| H.3      | Case 2, small-draft models . . . . .   | 100        |
| H.4      | Case 2, large-draft models . . . . .   | 101        |
| H.5      | Case 3, small-draft models . . . . .   | 101        |
| H.6      | Case 3, large-draft models . . . . .   | 102        |
| <b>I</b> | <b>The added mass component <math>C_A</math> and the drag coefficient <math>C_D</math><br/>measured with small-draft models, plotted for <math>KC = [1, 16]</math></b> | <b>103</b> |
| I.1      | Case 1 . . . . .   | 103        |
| I.2      | Case 2 . . . . .   | 104        |
| I.3      | Case 3 . . . . .   | 104        |
| <b>J</b> | <b>Frequency spectra of the Hammer test</b>  | <b>105</b> |
| J.1      | Plates without models . . . . .  | 105        |
| J.2      | Plates with small-draft models . . . . .   | 114        |
| J.3      | Plates with large-draft models . . . . .   | 122        |

# Chapter 1

## Introduction

In this thesis, a study is conducted investigating the interaction and hydrodynamic forces between the floating elements of a catamaran type of floating solar module. The catamaran-shaped floaters are tested in forced oscillating flow. The catamaran-shaped floaters are experimentally and numerically tested for three cases, with two drafts per case. The Keulegan-Carpenter number KC number, determines the hydrodynamic forces on the module in oscillating flow. The KC number compares the inertia and drag term in oscillating flow and can be written as

$$\text{KC} = \frac{U_m T}{D} = \frac{2\pi\eta_a}{D} \quad (1.1)$$

where  $U_m$  is the amplitude velocity,  $T$  is the period,  $D$  is the characteristic length and  $\eta_a$  is the amplitude of the oscillation. The KC number is explained further in Section 2.3.

This thesis presents one experiment and one numerical analysis are presented. WAMIT version 7.4 is used for conducting the numerical analysis of added mass, damping, and exciting forces in different degrees of freedom (DOF). The experiment is conducted in the Lader Tank placed at the Centre of Marine Technology in Trondheim, Norway.

In the autumn of 2022, co-students Petter Grudt Hals and Kristian Mikkelsen conducted an experiment investigating three cases of square-shaped cylinders with three heights in forced oscillatory flow. The experiment in 2022 is used as a source of comparison. The experimental setup of both the experiment conducted in 2022 regarding square-shaped cylinders and the experiment conducted for this master thesis is described in chapter 3.

### 1.1 Motivation

Along with the green shift, there is an increase in demand for renewable energy. Floating solar panels are an increasingly popular and expanding concept in renewable energy. For these structures, large areas are exposed to the free surface.

---

Consequently, large areas are exposed to hydrodynamic forces. The geometry of the floating elements is essential for how these forces affect the structure. This thesis studies the hydrodynamic forces acting on small-volume pontoons shaped as cylinders. These small-volume pontoons make the structure stable, and free surface disturbances are minor. Consequently, the structure is dominated by viscous effects due to flow separation. For the concept studies in this thesis, the floating solar panels are connected by a hinge, making this concept a multi-modular structure [1].

To make solar panels float, the structure needs some floating devices, usually pontoons. The hydrodynamic forces on the structure vary with the floater shape and configuration of the floater chosen floater. Moss Maritime has since 2016 worked on an offshore concept consisting of four circulate cylinders attached to each panel [2]. Ocean sun is working on a concept that is based on attaching solar panels to a thin, flexible membrane that floats near-shore sites or at reservoirs [3]. There are some hybrid concepts that combine everything from ocean energy systems, wind, and hybrid floating solar [4]. All these have different floating configurations and are subjected to various hydrodynamic forces.

Magnus Onsrud did his Master's Thesis on the concept of Moss Maritime. His master's thesis contributes with valuable insights into the concept [2]. The concept to be studied for this thesis is similar to the concept of Moss Maritime. The pontoon-supported modules are connected by hinges, allowing them to move with the wave elevation. There is high stress concentration in the hinges. This is studied in this thesis, and should be studied separately. If the pontoons are small and slender, flow separation is expected to dominate the wave-and current loads. Since the pontoons are placed closely together for the concept studied in this thesis, it is expected that interaction occurs between them, causing increased stress in the hinges. A sketch of the three modules connected by hinges is presented in Figure 1.1.

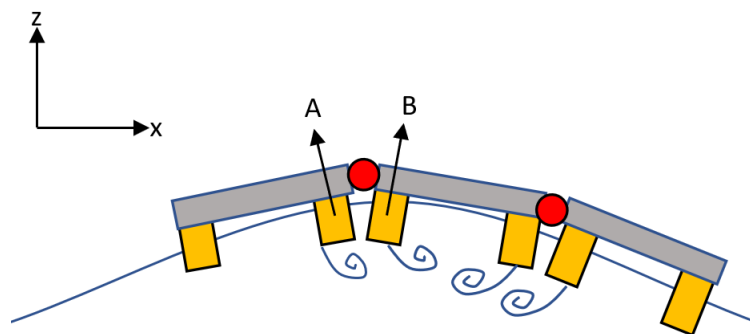


Figure 1.1: A sketch of three solar island modules connected by hinges. Wake shedding happens between two pontoons.

When placing two or more pontoons closely together, a set of problems related to the distance-to-width ratio appears. The first problem is that the wake generated between two bodies is different than for infinite fluid. The second problem is that the wake hit and affects nearby bodies, affecting the load. It is essential to investigate wake interaction, three-dimensional effects on the pontoons, and scaling factors for

---

structure-dominated viscous effects due to flow separation. With limited airgap, there may be fatiguing forces, also caused by slamming.

The concept of floating solar islands is still under development, and limited research is done on this topic, making for a broad hypothesis. The hypothesis made for this study is that there are non-negligible forces on the pontoons of the solar island modules.

## 1.2 Literature review

The hydrodynamic forces on circular cylinder bodies have been well studied and documented. Circulate cylinders have been important in the oil industry and have been studied thoroughly, but square-shaped cylinders and catamaran-shaped models have not been studied as extensively. This has left an interest regarding the interaction between square-shaped cylinders, and catamaran-shaped models, in oscillatory flow.

In 1977, Zdravkovich wrote a review on the flow interference between two circular cylinders in various arrangements [5]. In this review, Zdravkovich explains that in a steady current, the behavior of two cylinders in close proximity to each other is more complex than that of two cylinders far apart. His review can be divided into three possibilities of arrangements of the two cylinders; Tandem arrangement, side-by-side arrangement, and staggered arrangement.

Pannell, Griffiths, and Coals conducted tests force measurements on two "*circulate wires*" [6] in 1925. The distance between the centre of the wires varied from 1D (diameter of separation), where the wires were in contact, to 6D. The combined drag force was measured, and the experimental results are visualized in appendix Section A.1. They found that the minimum drag on two wires when in contact, was only 40% of the drag on one wire alone. The reasoning for this was assumed to be due to an improved streamlining of the flow pattern. Another finding from this experiment was that the combined drag force increased with increased distance between the centre of the wires.

Biermann and Herrnstein conducted in 1934, further studies on forces on two cylinders from a wind tunnel, with varying the spacing between the cylinders. In this experiment, it was possible to measure the drag force on each cylinder separately. This separate measuring system made it possible to introduce an "*interference drag coefficient*" that was defined as "[...] *the between the drag coefficient measured on one of the cylinders in tandem and the drag coefficient of the single cylinder at the same Reynolds number.*" [7]. By adding this interference drag of both cylinders, they obtained the combined interference drag as shown in Section A.2. This experiment found that the interference drag coefficient for upstream cylinders decreased with the spacing ratio, until  $L/D$  was smaller than 3  $D$ , where  $L$  is the length of the cylinder, and  $D$  is the diameter. When  $L/D$  became larger than 3, the coefficient increased. For the downstream cylinder, the coefficient increased until  $L/D = 2.5$  and decreased slightly after.

---

In 1959, Hori used only three spacings for his experiments; 1.2D, 2.0D, and 3.0D, where D is the diameter [8]. He measured the pressure disturbance around two cylinders in a tandem arrangement. His findings from this pressure disturbance are found in Section A.3. Hori found that for upstream cylinder affected the pressure distribution at the rear part only. With the increased spacing of the downstream cylinders, the base pressure was increased, and the upstream cylinder drag was reduced.

In 1958, Garbis H. Keulegan and Lloyd H. Carpenter published a research paper regarding the forces on a cylinder and plates in an oscillating fluid [9]. They investigated the inertia and drag coefficients of the plates and cylinders. They started with Stokes' studies and suggested that there is a physical relation between the flow patterns around the cylinders and plates, and the parameter  $U_m T/D$ . This relation was later known as the Keulegan-Carpenter number. The KC number is explained in greater detail in Section 2.3. They found that the drag coefficient  $C_d$  started with an unusually large value for low KC numbers up to 10, then decreased rapidly, and then decreased gradually for increased KC numbers. This plot is shown in the appendix, Figure A.4.

The forces that occur for sharp-edged cylinders in oscillatory flow at low KC numbers are discussed in a research article written by Graham in 1980[10]. The conclusion of that paper was presented at the International Symposium on Wave Induced Forces on Structures at Bristol in 1978. Bearman also did a similar experiment to Graham when he studied how the low KC numbers affected the forces on cylinders in viscous oscillatory flow [11]. Bearman found that the resulting force had "*[...] components both in phase with the fluid acceleration (inertia) and in phase with the velocity (drag)*".

In 2001, B. Havel, H. Hangan, and R. Martinuzzi conducted a two- and three-dimensional study regarding sharp-edged bluff bodies [12]. They investigated the changes in aerodynamic loading and wake dynamics when altering the distance gap. They found key differences in the wake dynamics due to the separated shear layer from the first body to the latter body. Amongst their findings, was that (1) for very small gaps, the shear layer separated at the first body, and '*overshoot*' the downstream body. The second body is subjected to the low-pressure area behind that forms downstream for the first body [13]. (2) For a slight increase in the gap, the *overshoot* reaches the side of the second body and reattaches. (3) For further increased gap, the second body is affected by the fully developed vortices. (4) When increasing the gap sufficiently, the bodies no longer affect one another.

The hydrodynamic behavior of perforated plates was experimentally and numerically investigated by Fredrik Mentzoni in 2019 [14]. He found that the damping force dominated over the added mass force for higher KC numbers. The damping force dominance increased with increasing perforation ratio as well.

In 2019, Magnus Onsrud wrote his master's thesis at NTNU, where he conducted an experimental study on the wave-induced vertical response of a floating solar island [2]. He studied a simplified model of the Moss Maritime concept, where his model was a 1X9 module train of hinged solar panels. The model was scaled 1:20, and was tested for wave periods varying from 2-13 seconds. Onsrud found that this model



---

was sufficient for low-frequent sea states, but should be investigated further for other sea states. A picture of his model can be found in Section A.5.

Henrik Reiten wrote his master's thesis in 2022, investigating the 2-dimensional hydrodynamic forces and wake interaction between two or more square-shaped cylinders KC numbers ranging from 1-32 [15]. Reiten found that there was an increased difference force as the KC number increased. The difference force showed to be dominated by the second harmonics component. The difference force was found to be sensitive to the distance between the cylinders in tandem and the inflow angle.

## 1.3 Previous Work - Project Thesis

This master thesis is a continuation of the research conducted during the fall semester of 2022, as documented in the project thesis. Consequently, certain sections of the project thesis are reused in this master thesis. The main objective of the project thesis was to create a solid theoretical background and an introduction to the analysis of forces on square-shaped cylinders in oscillatory flow.

When writing the project thesis, the original plan was to conduct two experiments for the master thesis. The first experiment planned was regarding the investigation of catamarans in forced oscillatory flow, which was conducted. The second experiment intended to investigate the hydrodynamic loads of a train of floating solar panels in waves. However, due to constraints of laboratory resources, it became necessary to discard the second experiment.

## 1.4 Scope of Work and Objectives

The primary objective of this thesis is to study the hydrodynamic interactions that occur between two catamaran-shaped pontoons in harmonically oscillatory flow in varying conditions. This is compared with the interaction between two and four square-shaped cylinders operating under the same conditions. To define the scope of work for this thesis, the following objectives have been outlined:

- Develop an understanding of the theory regarding catamarans and square-shaped cylinders in harmonic oscillatory flow in different conditions and arrangements.
- Conduct a numerical investigation focusing on the hydrodynamic forces obtained for different configurations of catamaran-shaped pontoons in oscillating flow. The numerical investigation contains a sensitivity analysis and convergence study for both mesh refinement and wave refinement.
- Conduct an experimental study of the hydrodynamic forces on catamaran-shaped pontoons in oscillatory flow. Various configurations are tested.

- 
- Compare the experimental and numerical results to validate the results. These are compared to the numerical and experimental results for two and four square-shaped cylinders obtained in previous work.
  - Establish a strong basis for further studies on this topic.

# Chapter 2

## Theory

The focus of this section is to present the terminology used in this thesis, already existing theory, governing equations, and dimensionless quantities. These are relevant for the discussion of the experimental and numerical results.

### 2.1 Terminology

In this section, the terminology used throughout this master's thesis is introduced. A group of floating solar panels that are connected, is referred to as a solar island. There are currently two main categories of solar islands: membrane and multi-modular. It should be noted that only multi-modular solar islands are the focus of this thesis. Additionally, a group of islands is called a solar island farm. One singular module of this solar island is called a solar panel or unit, while the floating elements are referred to as pontoons. A visualization of this is found in Figure 2.1.

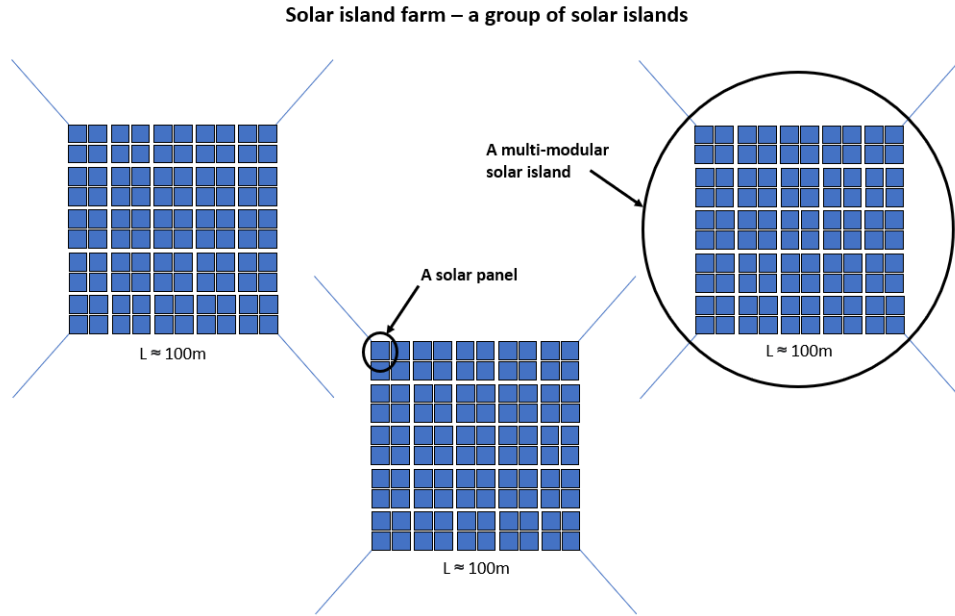


Figure 2.1: A visualization of the segments of a solar island farm.

### 2.1.1 The multi-modular concept

Each unit of the solar island has the full-scale size of 2 meters and is arranged in 10x10 units. The solar island itself is approximately 100x100 meters. Each unit can carry several solar panels and its floater ranges from a shallow barge to somewhat less shallow catamaran-shaped floater to either square- or round-shaped cylinders. In this thesis, the main focus is directed to the catamaran-shaped floaters, which contain a simple comparison to square-shaped cylinders. A visualization of the square-shaped cylinder, catamaran, and barge-shaped floaters can be found in Figure 2.2.

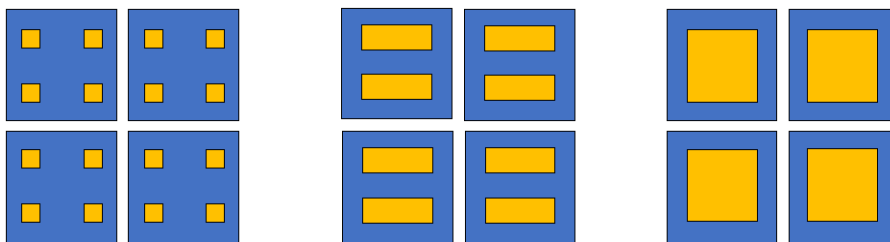


Figure 2.2: Floating solar units seen from beneath. From left to right: square-shaped cylinders, catamaran, and barge type of floaters.

The solar panels are attached to the unit so that the panel lies flat and the wind loads are minimized, yet still matter. The hydrodynamic loads on the unit only, are investigated in this thesis. The effect of wind should be investigated in another study. The distance between the floaters affects the hydrodynamic loads acting on the solar island due to the wake effect.

---

## 2.2 Governing equations

### 2.2.1 Navier-Stokes equation

Around 1850, Navier and Stokes formulated the Navier-Stokes equations. This equation is also known as *governing equations of fluid motions* and *momentum equations*. The equation describes the motion of a fluid's behavior. The Navier-Stokes equation is derived from Newton's second law for a fluid element. In Cartesian coordinates, the equation is as follows:

$$\frac{\partial \mathbf{u}}{\partial t} + \nabla \mathbf{u} \cdot \mathbf{u} = -\frac{1}{\rho} \nabla p + \mathbf{g} + \nu \nabla^2 \mathbf{u} \quad (2.1)$$

Here,  $\nu = \mu/\rho$ . As this equation is a vector equation and  $\nabla = [\partial/\partial x, \partial/\partial y, \partial/\partial z]$ , the Navier-Stokes equation is three equations.  $\mathbf{u}$  is the fluid velocity vector,  $\rho$  is the fluid density,  $\nabla p$  is the pressure gradient and  $\mu \nabla^2 \mathbf{u}$  is the shear term [13].

As the fluid velocity vector  $\mathbf{u}$  and the pressure is unknown, there are four unknown and three equations, introducing the continuity equation for an incompressible fluid

$$\nabla \cdot \mathbf{u} = 0 \quad (2.2)$$

To efficiently solve these arguments, the problem must be simplified. This leads to potential theory.

### 2.2.2 Bernoulli and Laplace

Bernoulli's equation is derived from the Navier-Stokes equation by assuming conservative forces, inviscid flow, no turbulence, incompressible fluid, and steady flow.

$$\frac{\partial \varphi}{\partial t} + \frac{1}{2} \nabla \varphi \cdot \nabla \varphi + gz + \frac{1}{\rho} p = C \quad (2.3)$$

$$\nabla^2 \varphi = 0 \quad (2.4)$$

## 2.3 Parameters and coefficients

In 1903 Arnold Sommerfeld named the Reynolds number after Osborne Reynolds, since Osborne Reynolds used this in many of his experiments. The Reynolds number is a dimensionless number describing the ratio of inertia forces to viscous forces [16]. By examining the Reynolds number one can say something about the separation point of the flow, and the degree of turbulence. The Reynolds number is given as

$$\text{Re} = \frac{U_m D}{\nu} \quad (2.5)$$

---

where  $U$  is the velocity,  $D$  is the characteristic length and  $\nu$  is the kinematic viscosity of the fluid.

The Kaulegan-Carpenter number compares the inertia and drag term in oscillatory flow [9]. It is named after Garbis H. Keulegan and Lloyd H. Carpenter. The Kaulegan-Carpenter number is defined as

$$\text{KC} = \frac{U_m T}{D} \quad (2.6)$$

where  $U_m$  is the amplitude velocity,  $T$  is the period, and  $D$  is the characteristic length. This expression can be rewritten in regard to a harmonically oscillating body

$$\text{KC} = \frac{2\pi \eta_a}{D} \quad (2.7)$$

where  $\eta_a$  is the amplitude of the oscillation. If the body is subjected to waves, the velocity can be considered as the amplitude of the water particle velocity. The expression can be rewritten as

$$\text{KC} = \frac{2\pi \zeta_a}{D} \quad (2.8)$$

where  $\zeta_a$  is the wave amplitude.

The ratio  $\beta$  of the Reynolds number and KC number can be found as [17]

$$\beta = \frac{\text{Re}}{\text{KC}} = \frac{D^2}{\nu T} \quad (2.9)$$

The angular natural frequency of a system with stiffness  $k$  and mass  $m$  can be expressed as the following

$$\omega = \sqrt{\frac{k}{m}} \quad (2.10)$$

## 2.4 Hydrodynamic force

Hydrodynamic responses in regular waves can be divided into two sub-problems: diffraction problem and radiation problem. For these two conditions, steady-state condition is assumed. The diffraction problem is when there are incident regular waves, and the structure is restrained from oscillating. The hydrodynamic loads in this sub-problem are called wave excitation loads which are composed of Froude-Kriloff and diffraction forces and moments. The second sub-problem is the radiation problem, where the structure is forced to oscillate, generating excitation waves. There are no incident waves, and the hydrodynamic loads are the added mass, damping, and restoring terms. In harmonic motion, the hydrodynamic added mass and damping loads can be written from Newton's 2<sup>nd</sup> law as

$$F = -A_{kj}\ddot{\eta}_j - B_{kj}\dot{\eta}_j \quad (2.11)$$

where  $\ddot{\eta}_j$  and  $\dot{\eta}_j$  is acceleration and velocity in mode  $j = 1, 2, \dots, 6$ .

---

One can define the oscillation of the body as

$$\eta = \eta_a \cos(\omega t) \quad (2.12)$$

which yields

$$\dot{\eta} = -\omega \eta_a \sin(\omega t) \quad (2.13)$$

$$\ddot{\eta} = -\omega^2 \eta_a \cos(\omega t) \quad (2.14)$$

One can separate the added mass and damping from the total measured hydrodynamic forces by Fourier averaging [17]. This is done by multiplying Equation 2.11 with the acceleration term and integrating over n periods

$$\int_{nT} F \ddot{\eta} dt = - \int_{nT} A \ddot{\eta} \ddot{\eta} dt - \underbrace{\int_{nT} B \dot{\eta} \ddot{\eta} dt}_{=0} \quad (2.15)$$

where T is the period and n is a selected oscillation period. The damping term consists of both sine and cosine, yielding zero when integrated over the entire period. It is now possible to solve for mass. The damping term can be found similarly, but multiplying with velocity instead of acceleration. The added mass term yields zero, and one can solve for added mass.

$$\int_{nT} F \dot{\eta} dt = - \underbrace{\int_{nT} A \dot{\eta} \ddot{\eta} dt}_{=0} - \int_{nT} B \dot{\eta} \dot{\eta} dt \quad (2.16)$$

### 2.4.1 Exciting forces of a submerged body

The excited forces of a submerged body are made up of the forces from Froude Krylov and the diffraction forces and are given as

$$F_{exc} = F_{FK} + F_{Diff} \quad (2.17)$$

Froude Krylov forces on a submerged body are found by integrating the hydrodynamic pressure over the significant surface of the body.

$$F_{FK} = \int_S p \vec{n}, \quad (2.18)$$

$$F_{FK} = \int_S \rho g \zeta_a e^{kz} \sin(\omega t - kx) \vec{n},$$

where S is the area that normal vector  $\vec{n}$  is oriented towards.  $\rho$  is the water density, g is gravity,  $\zeta_a$  is wave amplitude, k is the wave number, and z is the characteristic height of the body. The sine part of the equation is the phase, where  $\omega$  is the phase, t a given time, and x is a given placement along the x-axis.

## 2.4.2 Exciting forces of a submerged catamaran-shaped body

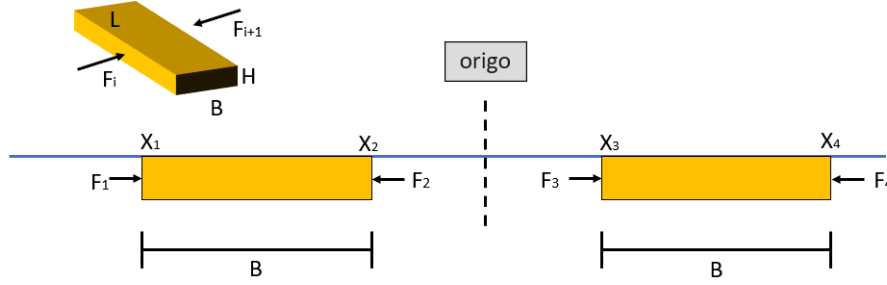


Figure 2.3: Forces integrated over the sides of the catamaran.

The forces integrated over the sides of the catamaran are illustrated in Figure 2.3. The Froude-Krylov force of a catamaran-shaped submerged body with significant width  $B$  and height  $H$ , as shown in Figure 2.3, is calculated in Appendix B to be

$$F_{FK} = \frac{L\rho g\zeta_A}{k}(1 - e^{kH}) 2 \sin(\omega t) \left[ \sin(kx_3) - \sin(kx_3 + kB) \right]. \quad (2.19)$$

The diffraction force on complex form of the same submerged body as Equation 2.19 is calculated in Appendix B to be

$$F_{Diff} = \sqrt{(\Re)^2 + (\Im)^2}$$

$$F_{Diff} = \sqrt{\left( r \cos(\phi_{exc}) - F_{FK} \cos(\phi_{FK}) \right)^2 + \left( r \sin(\phi_{exc}) - F_{FK} \sin(\phi_{FK}) \right)^2} \quad (2.20)$$

and

$$\phi = \arctan\left(\sqrt{\frac{\Re}{\Im}}\right) \quad (2.21)$$

$$\phi = \arctan\left(\sqrt{\frac{r \cos(\phi_{exc}) - F_{FK} \cos(\phi_{FK})}{r \cdot \sin(\phi_{exc}) - F_{FK} \cdot \sin(\phi_{FK})}}\right)$$

where

$$\Im\left(ir \sin(\phi_e) - iF_{FK} \sin(\phi_{FK})\right) = r \sin(\phi_e) - F_{FK} \sin(\phi_{FK}) \quad (2.22)$$

## 2.4.3 Damping

Damping in a harmonically oscillating system contained linear and quadratic damping. The linear and quadratic term are referred to as  $B_{33}^{(1)}$  and  $B_{33}^{(2)}$ , respectively. The damping term can be rewritten as

$$B_{33}\dot{\eta}_3 = B_{33}^{(1)}\dot{\eta}_3 + B_{33}^{(2)}\dot{\eta}_3|\dot{\eta}_3| \quad (2.23)$$



---

## 2.4.4 The Morison equation

In potential flow theory, the viscous effect is neglected. One way to incorporate the viscous effect and calculate the forces on a moving body, is by the Morison equation [18]. Morison's equation per unit length for a circulate bodies is given as

$$F_m(t) = \rho \frac{D^2 \pi}{4} C_A a_w(t) + \frac{1}{2} \rho D C_D u_w(t) |u_w(t)| \quad (2.24)$$

where  $\rho$  is the density,  $D$  is the characteristic length,  $C_A$  is the added mass coefficient,  $C_D$  is the drag coefficient and  $a_w(t)$  and  $u_w(t)$  is acceleration and velocity.

For a catamaran-shaped body, the Morison equation can be expressed as

$$F_m(t) = \rho H L B C_A a_w(t) + \frac{1}{2} \rho B C_D u_w(t) |u_w(t)| \quad (2.25)$$

The acceleration can be expressed as

$$\begin{aligned} \text{KC} &= \frac{U_m T}{B} = \frac{\omega \eta_A T}{B} = \frac{\frac{2\pi}{T} \eta_A T}{B} = 2\pi \frac{\eta_A}{B} \\ &\Rightarrow \eta_A = \frac{\text{KC}}{2\pi} B \end{aligned} \quad (2.26)$$

$$a_w = \omega^2 \eta_A = \frac{(2\pi)^2 \text{KC}}{T^2} \frac{\text{KC}}{2\pi} B = \frac{2\pi}{T^2} \text{KC} B. \quad (2.27)$$

## 2.4.5 Sloshing modes

Sloshing is a hydrodynamic phenomenon that occurs when a structure entraps liquid with the free surface. The liquid moves back and forth between the walls with the natural modes of the barge. This results in resonant excitation of the liquid with natural frequencies. The sloshing can have a large influence on the dynamic stability. In many cases, the excitation of the lowest natural frequency is expected to be most significant [19]. When studying catamaran-shaped floaters placed relatively close together, sloshing occurs between them.

In 2002, Molin formulated a simplified mathematical expression determining the sloshing modes for gap resonance between two barges in three dimensions[20]. The problem Molin describes assumes linearized potential flow theory, infinite water depth, and length, and that the beam of the barges contains moonpools. It should be noted that for the simplified formula to be reasonable, the barge breadth  $B$  divided by the gap width  $b$ ,  $B/b$ , should be larger than 2-3. The sloshing modes are expected to be somewhat over-predict. This formula is expressed as

$$\omega_{n0}^2 \simeq g \lambda_n \frac{1 + J_{Dn0} \tanh(\lambda_n h)}{J_{Dn0} + \tanh(\lambda_n h)} \quad (2.28)$$

where  $n$  is the mode and

$$J_{Dn0} = \frac{n}{b l^2} \int_0^b dy \int_0^b dy' \int_0^l dx \int_0^l dx' \frac{\cos(\lambda_n x) \cos(\lambda_n x')}{(x - x')^2 + (y - y')^2} = \frac{n}{b l^2} I_{nn00} \quad (2.29)$$

---

$J_{Dn0}$  can be reduced to

$$J_{Dn0} = \frac{2}{n\pi^2 r} \left[ \int_0^1 \frac{r^2}{u^2 \sqrt{u^2 + r^2}} \left[ 1 + 2u + (u - 1) \cos(n\pi u) - \frac{3}{n\pi} \sin(n\pi u) \right] du + \frac{1}{\sin(\theta_0)} + 1 + 2r \ln \frac{1 + \cos \theta_0}{1 - \cos \theta_0} \right] \quad (2.30)$$

where  $r = b/l$  and  $\tan \theta_0 = r^{-1}$  [21]

## 2.5 Nondimensionalization

For this thesis, some nondimensionalizations are used consistently. The added mass coefficient  $C_{Aij}$ , damping coefficient  $C_{Bij}$  and force coefficient  $X_i$  is made nondimensional as the following

$$C_{Aij} = \frac{A_{ij}}{\rho \nabla} \quad C_{Bij} = \frac{B_{ij}}{\rho \nabla \omega} \quad X_i = \frac{F_i}{\rho g \nabla} \quad (2.31)$$

where  $A_{ij}$  is the added mass,  $B_{ij}$  is the damping,  $F$  is force,  $\rho$  is water density,  $\nabla$  is the submerged volume,  $\omega$  is frequency and  $g$  is the gravitational acceleration.

The first part of Morison equation, from Equation 2.24 can be re-written as

$$F = \rho HLB C_A a_w(t) = \rho HLB^2 C_A KC \frac{2\pi}{T^2}. \quad (2.32)$$

The first part of the Morison equation converted to the nondimensionalization used for force in Equation 2.31 can be expressed as

$$\frac{F}{\rho g HLB} = \frac{\rho HLB^2 C_A KC \frac{2\pi}{T^2}}{\rho g HLB} = \frac{B C_A KC 2\pi}{g T^2}. \quad (2.33)$$

# Chapter 3

## Experiment

The experimental setup and execution of the experiment conducted in this master's thesis are presented in this chapter. A summary of the experimental setup and execution of the experiment of 2022 regarding square-shaped cylinders, is also provided. The Ladertanken (*en*: Lader tank) is used for both the investigation of forced oscillation of square-shaped cylinders, as documented in the project thesis, and for forced oscillation of catamarans in this master's thesis. The scale used for these experiments is 1:10, where the full-scale length of one catamaran-shaped pontoon is 2 m, resulting in a model length of 0.2 m.

### 3.1 The Lader tank - Lab facilities

The Lader tank is placed at the Center of Marine Technology in Trondheim, and is used for the experiments of forced oscillation. The tank got its name from Pål Lader, who initiated the installation of the tank in 1996. Since then, the tank has been used for research purposes by SINTEF, as well as experiments conducted by MSc and Ph.D. students.

The tank is 13.5 m long, has a width of 0.6 m, and the water level is adjustable. The water level is set to 1.0m for the experiments conducted in the Lader tank regarding forced oscillations. Due to leakage, it is important to monitor the tank and refill it when necessary. The tank is filled with fresh water and the temperature is monitored throughout the experiment. A change of temperature of  $2^{\circ}C$  results in an uncertainty of  $0.36kg/m^3$  in water density, which makes the changes in water density negligible.

The tank walls are made from Plexiglass, an alternative to glass. This makes it possible to observe the model within the tank. A wave flap is installed at one end of the tank, making deep water waves accessible. The wave flaps are not for the experiments of forced oscillation in this master's thesis. A rig on top of the tank is attached to a rail system reaching the entire tank, making it possible to adjust the rig. The rig and an actuator make it possible to move the model up and down as well. Two plates are attached to the rig and are connected to two force-measuring

sensors. Models can be attached to the plates. The test rig is explained in greater detail in Section 3.3.1. A sketch of the Lader tank and the setup used, is presented in Figure 3.1.

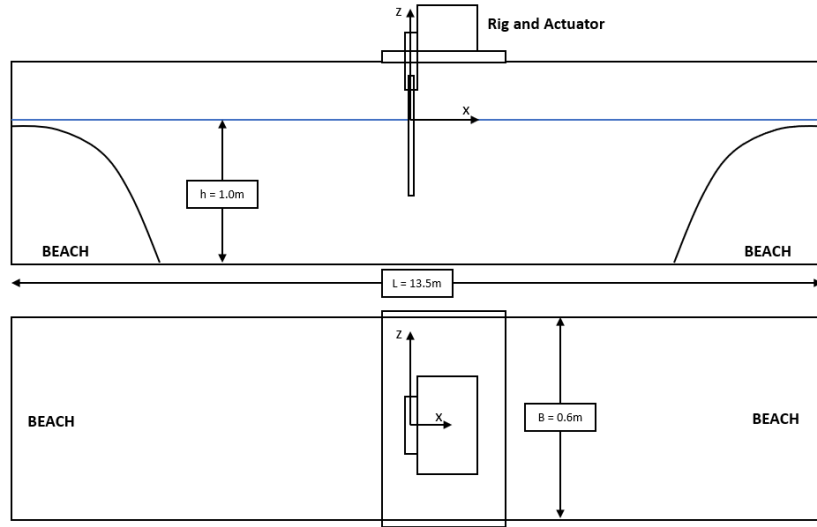


Figure 3.1: A sketch of the setup and tank characteristics of the Lader Tank shown from side-view and bird-view, respectively.

## 3.2 Previous work - square-shaped cylinders

In the fall of 2022, as documented in the project thesis, the experiment with square-shaped cylinders was conducted in the Lader tank. A summary of the experimental setup and testing procedure, as well as a summary of the findings, is presented in this section.

### 3.2.1 Model description

The experiment of square-shaped cylinders was held in the fall of 2022, in the Lader tank testing square-shaped cylinders. The cylinders represent the draft of a floating solar panel with four square-shaped cylindrical-shaped floaters. Three different heights, simulating three drafts of the cylinders, were tested with seven different placement configurations. This master's thesis only elaborates on the configurations regarding two and four cylinders, as shown in Figure 3.2. The length and width of the cylinders are the same for each case, but the height varies. The dimensions for the sets of cylinders are found in Table 3.1. The three different placement configurations simulate the distance between neighbor cylinders. The different case configurations can be found in Figure 3.2.

---

| Configuration no. | Referred to as      | Length [cm] | Width [cm] | Height [cm] |
|-------------------|---------------------|-------------|------------|-------------|
| Case 1            | small, $L/H = 1$    | 5           | 5          | 5           |
| Case 2            | medium, $L/H = 1/2$ | 5           | 5          | 10          |
| Case 3            | large, $L/H = 1/3$  | 5           | 5          | 15          |

Table 3.1: Dimensions of the square-shaped cylinders investigated in the project thesis.

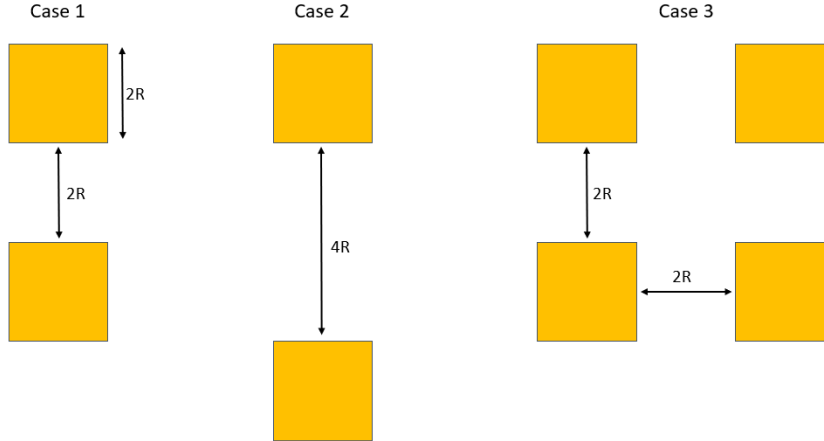


Figure 3.2: The different cases investigated for all three sized square-shaped cylinders.

### 3.2.2 Test program - Cylinders

The test program is based on testing the different cases of spacing for all three sizes. All cases are tested for increasing  $KC$  number, increasing by  $0.5 KC$ . The periods of the tests are  $1s$  and  $1.5s$ , and  $KC$  numbers  $7$ ,  $14$ , and  $21$  are repeated  $4-5$  times.

The rig runs without models attached first, to account for the effect of the rig alone. By doing this, the forces measured on the rig alone can be subtracted from forces measured when the models are attached, isolating the model forces. The frequency of measurements is  $200Hz$ . The different  $KC$  numbers tested are listed in Table 3.2.

| <b>KC</b>   | $\eta_{a,square-shaped}$ [cm] | $\eta_{a,diamond}$ [cm] | <b>KC</b>   | $\eta_{a,square-shaped}$ [cm] | $\eta_{a,diamond}$ [cm] |
|-------------|-------------------------------|-------------------------|-------------|-------------------------------|-------------------------|
| <b>1</b>    | 0.8                           | 1.1                     | <b>10.5</b> | 8.4                           | 11.8                    |
| <b>1.5</b>  | 1.2                           | 1.7                     | <b>12.5</b> | 9.9                           | 14.1                    |
| <b>2</b>    | 1.6                           | 2.3                     | <b>13</b>   | 10.3                          | 14.6                    |
| <b>2.5</b>  | 2.0                           | 2.8                     | <b>13.5</b> | 10.7                          | 15.2                    |
| <b>3</b>    | 2.4                           | 3.4                     | <b>14</b>   | 11.1                          | 15.8                    |
| <b>3.5</b>  | 2.8                           | 3.9                     | <b>14.5</b> | 11.5                          | 16.3                    |
| <b>4</b>    | 3.2                           | 4.5                     | <b>15</b>   | 11.9                          | 16.9                    |
| <b>4.5</b>  | 3.6                           | 5.1                     | <b>15.5</b> | 12.3                          | 17.4                    |
| <b>5</b>    | 4.0                           | 5.6                     | <b>16</b>   | 12.7                          | 18.0                    |
| <b>5.5</b>  | 4.4                           | 6.2                     | <b>16.5</b> | 13.1                          | 18.6                    |
| <b>6</b>    | 4.8                           | 6.8                     | <b>17</b>   | 13.5                          | 19.1                    |
| <b>6.5</b>  | 5.2                           | 7.3                     | <b>17.5</b> | 13.9                          | 19.7                    |
| <b>7</b>    | 5.6                           | 7.9                     | <b>18</b>   | 14.3                          | 20.3                    |
| <b>7.5</b>  | 6.0                           | 8.4                     | <b>18.5</b> | 14.7                          | 20.8                    |
| <b>8</b>    | 6.4                           | 9.0                     | <b>19</b>   | 15.1                          | 21.4                    |
| <b>8.5</b>  | 6.8                           | 9.6                     | <b>19.5</b> | 15.5                          | 21.9                    |
| <b>9</b>    | 7.2                           | 10.1                    | <b>20</b>   | 15.9                          | 22.5                    |
| <b>9.5</b>  | 7.6                           | 10.7                    | <b>20.5</b> | 16.3                          | 23.1                    |
| <b>10</b>   | 8.0                           | 11.3                    | <b>21</b>   | 16.7                          | 23.6                    |
| <b>11</b>   | 8.8                           | 12.4                    | <b>21.5</b> | 17.1                          | 24.2                    |
| <b>11.5</b> | 9.2                           | 12.9                    | <b>22</b>   | 17.5                          | 24.8                    |
| <b>12</b>   | 9.5                           | 13.5                    |             |                               |                         |

Table 3.2: KC numbers tested for square-shaped cylinders in forced oscillations.

### 3.2.3 Summary of the findings

The experiment with the square-shaped cylinders was successful. Co-student Kristian Mikkelsen focused his master's thesis on the wake interaction of these cases, focusing on staggered arrangement [22]. As the presented master's thesis focus on tandem arrangement, the main findings for tandem arrangement are summarized in the outline below:

- There was generally smaller hydrodynamic interaction between the square-shaped cylinders when increasing the distance. It was found that the hydrodynamic interaction decreased when the hydrodynamic forces increased. The hydrodynamic forces increased with increased KC number.
- The draft height of the cylinders had no large effect on the results. There was some scattering of the small drafted cylinders for small KC numbers.
- The large drafted models had to discard  $F^{4\omega}$  and  $F^{5\omega}$ , due to the eigenfrequency of the rig with the models attached.
- The results of case 3 could be used with the small drafted cylinders only. This was due to the weight that the four models added. The eigenfrequency

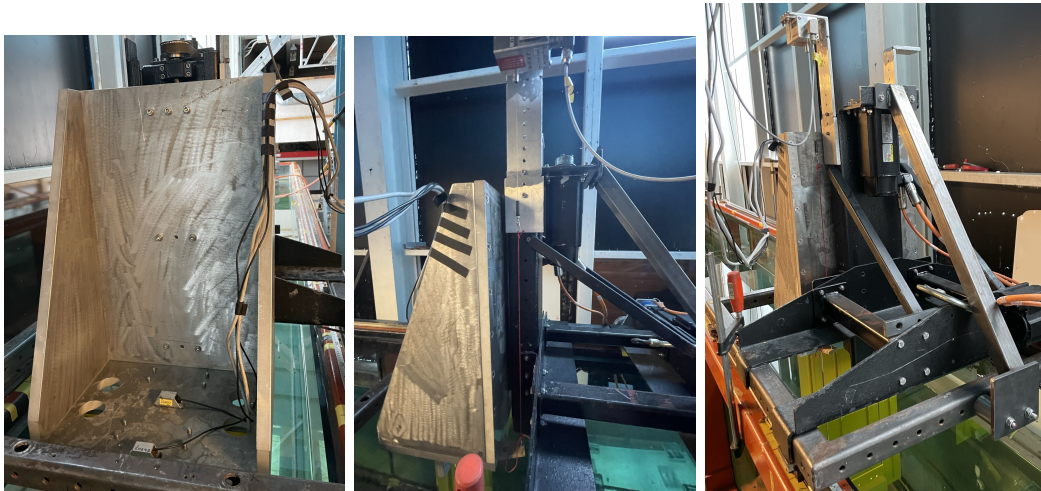
---

dominated the measurements for the medium and large drafted model for case 3, resulting in discarded them.

### 3.3 Experimental setup

#### 3.3.1 The test rig

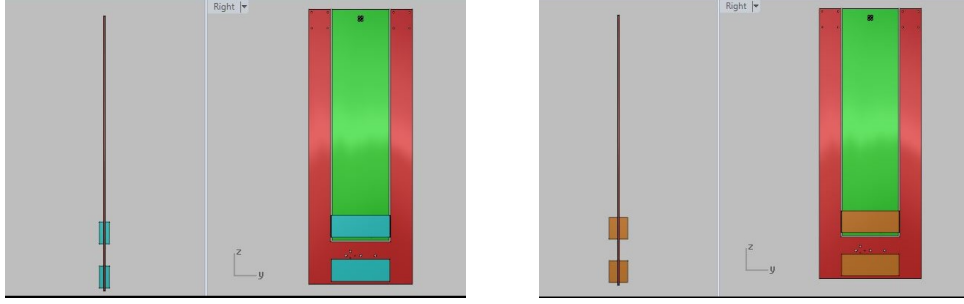
The actuator is placed in the middle of the tank, and the rig is wedged to avoid unnecessary motions that may affect the results. The custom-built rig is attached to the actuator, making it possible to move in the vertical direction. The actuator is programmed to oscillate with different amplitudes and velocities, making it possible to test for several KC numbers during the experiment. The rig and actuator are shown from front-view, side-view, and back-view in Figure 3.3.



(a) Front-view of the rig and actuator. (b) Side-view of the rig and actuator. (c) Back-view of the rig and actuator.

Figure 3.3: Front-view, side-view, and back-view of the rig and actuator, respectively.

The rig is attached to two plates with two force transducers that measure the separate forces of their respective plates. The outer plate has a width of 40 cm, providing a 10 cm space on each side towards the glass wall of the tank. High pressure occurs due to the oscillations occurs between the glass wall and plates of the rig, preventing the plates and glass wall from colliding. The plates have a variety of holes, making it possible to vary the placement of the models. After attaching the model, every excess hole is filled with yellow putty to obtain a smooth surface, avoiding hydrodynamic disturbance. One model is attached to both sides of the plate to maintain symmetry, as shown in Figure 3.4.



(a) Test rig for case 1 with the small-draft catamaran model with  $H/b = 1.5/7.5$ . (b) Test rig for case 1 with the large-draft catamaran model with  $H/b = 3/7.5$ .

Figure 3.4: The test rig with the small- and large-draft catamarans attached with gap distance as of case 1. The small- and large-draft catamarans is specified as  $H/b = 1.5/7.5$  and  $H/b = 3/7.5$  respectively.

### 3.3.2 Model description - Catamarans

The experiment investigating the catamarans is conducted by attaching two sets of catamarans to the rig, one set at the fixed position at the bottom of the outer plate, and one set at the placement of the case to be investigated. Three cases are tested for two height variations, so the total of runs becomes six. The catamaran model has a length  $L$  of 20 cm and a width  $B$  of 7.5 cm. The two catamaran heights that are tested, are 1.5 cm and 3 cm. The catamaran with a height of 1.5 cm is named a small-draft catamaran with  $H/L = 1.5/20$ . The tallest catamaran is named large-draft catamaran and has  $H/L = 3/20$ .

The catamaran models are attached so that the long side is parallel to the  $Y$ -direction of the tank. The two sets of catamarans have the same length and width, but different heights simulating two different drafts. The spacing between the catamaran sets simulates the distance between neighboring pontoons, either attached to the same solar panel or neighboring solar panels. A visualization of the catamaran model with dimensions is be found in Figure 3.5. The plate with the placement of the three cases is found in Figure 3.6. In Figure 3.7, one can see a picture of the large-drafted models attached with gap distance according to case 3,  $H/b = 3/11.25$ .



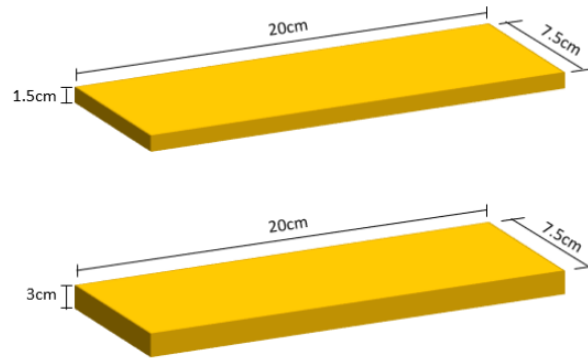


Figure 3.5: Dimensions of the small- and large-draft catamaran model.

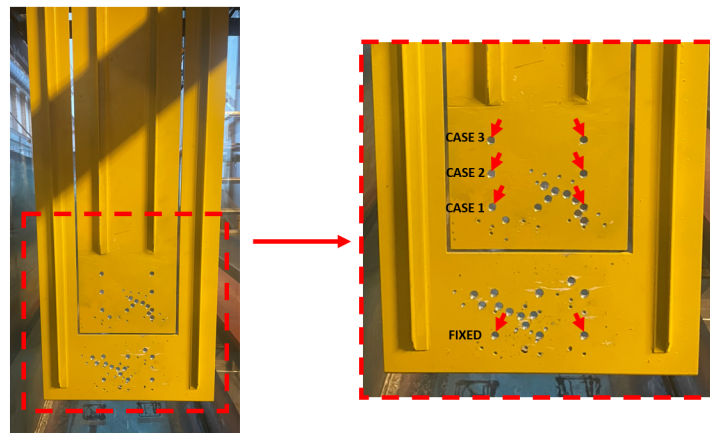


Figure 3.6: The holes that is used for the attachment of catamarans in case 1, case 2 and case 3.



Figure 3.7: Large-drafted models attached with gap distance according to case 3,  $H/b = 3/11.25$ .

---

### 3.3.3 Test program - Catamarans

This experiment follows mostly the same procedure as the experiment performed in the project thesis with square-shaped cylinders. After analyzing the data in the project thesis, it was concluded that there was no significant difference between the results of half period and half KC numbers when compared to whole. So for this experiment, only whole periods and KC numbers are tested. The rig can move up to 20cm from its center, which allows testing of KC numbers from 1 to 16. The tested KC numbers and the respective amplitude are shown in Table 3.4.

The actuator ramps up with four oscillations, oscillate 30 times at the given KC number, then ramps down with four oscillations. The small- and large-draft catamaran models are tested for three cases of placement. The distance between the models in each case is specified in Table 3.3 and visualized in Figure 3.6.

The rig runs without models attached first, as for the square-shaped cylinders. This makes it possible to isolate the forces of the models. The frequency of measurements is 200Hz as well.

| Case:                          | Case 1 | Case 2  | Case 3 |
|--------------------------------|--------|---------|--------|
| Distance b between the models: | 7.5cm  | 11.25cm | 15cm   |

Table 3.3: Case 1, case 2, and case 3 and their respective gap distance between the models.

| KC       | $\eta_a$ [cm] | KC        | $\eta_a$ [cm] |
|----------|---------------|-----------|---------------|
| <b>1</b> | 1.2           | <b>9</b>  | 10.7          |
| <b>2</b> | 2.4           | <b>10</b> | 11.9          |
| <b>3</b> | 3.6           | <b>11</b> | 13.1          |
| <b>4</b> | 4.8           | <b>12</b> | 14.3          |
| <b>5</b> | 6.0           | <b>13</b> | 15.5          |
| <b>6</b> | 7.2           | <b>14</b> | 16.7          |
| <b>7</b> | 8.4           | <b>15</b> | 17.9          |
| <b>8</b> | 9.5           | <b>16</b> | 19.1          |

Table 3.4: KC numbers, and the associated vertical amplitude, tested for the catamaran-shaped models in forced oscillations.

## 3.4 Instrumentation and Calibration

The instrumentation is a key part of conducting a successful experiment and obtaining reliable results. The instrumentation must be calibrated and tested to ensure correct measurements. An explanation of the instrument used in this experiment, and the procedure for using them is presented in this chapter.

---

### 3.4.1 Calibration of sensors

The sensors used for this experiment were calibrated by Robert and Terje, who are responsible for the lab equipment. The force sensors and position was zeroed between each run, and are checked to be zero at the start of each run. A manual test was executed to ensure that the access system is functioning correctly. This was done by applying some force by hand to the outer and inner plate in X-, Y- and Z-directions, and checking that the logging system corresponds.

### 3.4.2 Hammer test

When examining the data from the experiments, it is expected to dominate responses at certain frequencies, such as at the natural frequencies of the rig. By performing a Hammer test, it is possible to establish an overview of which frequencies the eigenfrequencies are expected to dominate. A hammer test is conducted by striking the model and its surroundings with a hammer in X-, Y-, and Z-direction. At the inner and outer plate it is not possible to strike the model in the Z-direction due to the water blocking the movement.

After the hammer has struck, the object vibrates at different frequencies. It is essential to note that electrical noise usually dominates at around 50Hz [23]. In this thesis, everything higher than 40Hz is filtered and discarded. The hammer test in this thesis is performed by striking the tank, stronghold, rig, and inner and outer plate.

Two pairs of sensors measure the forces on the setup, one on the outer plate and one on the inner plate. These are expected to respond differently to the hammer striking, due to the different sizes of the plates, and consequently weight. Since the outer plate is larger, it is expected to have an eigenfrequency at a lower frequency than the inner plate. The hammer test results are presented in Section 5.1.

## 3.5 Sources of Error

There are several sources of error when performing an experiment. These may originate from human errors or instrumentation. In this chapter, some possible sources of error are presented and discussed.

The instrumentation used in the lab varies in age and degree of wear. Some of the sensors may drift during the experiment, leaving it to post-processing to correct. The lab personnel ensured that the sensors used in this experiment should be sufficient, but some offset may be present.

When installing the rig, the plate is fastened with screws on the top of the rig. There is no support to this plate other than the screws and two supporter beams along the plate. This allows the plate to move the plate in Y-direction. The outer plate is quite easy to displace in the Y-direction, so the inner and outer plates are touching.

---

This creates physical noise when tracking, but is easily identified as spiking curves when tracking. This is a source of inconsistency during the experiment, though the worst effect of this error is avoided by careful monitoring.

One error that may be significant, is that the hammer test was performed after the experiments were conducted, and the rig was disassembled. Consequently, the rig had to be reassembled after the experiments in order to perform the hammer test. It could be argued that there is therefore some inconsistency in the experiment and hammer test.

The Lader tank is situated one level under a large cavitation tunnel. When this cavitation tunnel operates, vibration and noise travel through the building. When the tunnel is at its maximum speed, there are strong vibrations in the Lader tank. Experiments in the Lader tank were on hold when the tunnel ran at max speed, avoiding the largest impact. It should be noted that there may be some inconsistent vibrations due to this, though these are hard to identify.

# Chapter 4

## Numerical analysis

The numerical analysis of this thesis is done with WAMIT as the numerical solver [24]. The low-drafted catamarans are simulated with three gap distance configurations and two draft configurations. A description of the numerical software WAMIT and the approach of how to use the numerical solver is discussed in this section.

### 4.1 WAMIT

WAMIT is a numerical solver that solves the boundary value problem for the interaction of structures and surface waves in finite- and infinite-water depth [24]. WAMIT provides a variety of different output files. An overview of these is found in Figure 4.1.

| Option | Description                                      | Filename                 |
|--------|--|--------------------------|
| 1      | Added-mass and damping coefficients              | <i>frc.1</i>             |
| 2      | Exciting forces from Haskind relations           | <i>frc.2</i>             |
| 3      | Exciting forces from diffraction potential       | <i>frc.3</i>             |
| 4      | Motions of body (response amplitude operator)    | <i>frc.4</i>             |
| 5p     | Hydrodynamic pressure on body surface            | <i>frc.5p</i>            |
| 5v     | Fluid velocity vector on body surface            | <i>frc.(5vx,5vy,5vz)</i> |
| 6      | Pressure/ free-surface elevation at field points | <i>frc.6</i>             |
| 7      | Fluid velocity vector at field points            | <i>frc.(7x,7y,7z)</i>    |
| 8      | Mean drift force and moment from momentum        | <i>frc.8</i>             |
| 9      | Mean drift force and moment from pressure        | <i>frc.9</i>             |

Figure 4.1: The output options provided by WAMIT [25].

WAMIT is based upon some assumptions that should be noted. The software assumes potential flow theory, consequently, viscous effects of fluids are not considered. WAMIT assumes that the wave amplitude is small compared to the

wave length. The flow is assumed ideal and time-harmonic, and the free-surface conditions are linearized.

WAMIT consists of two sub-programs; '*POTEN*', which calculates velocity potentials, and '*FORCE*', which calculates the desired hydrodynamic parameters. WAMIT uses the input files listed in Table 4.1 and produces the output files specified in Figure 4.1 on the format specified in Figure 4.3. Whether the bodies are located at the free surface, submerged or mounted on the sea bottom, must be specified. One must also specify if the bodies are freely floating, restrained or in a fixed position. To calculate the radiation and diffraction velocity potentials on the wetted surface are obtained by using Green's theorem with the free-surface source-potential as the Green function [24]. A flowchart of WAMIT and its sub-programs with their associated input and output files is visualized in Figure 4.2.

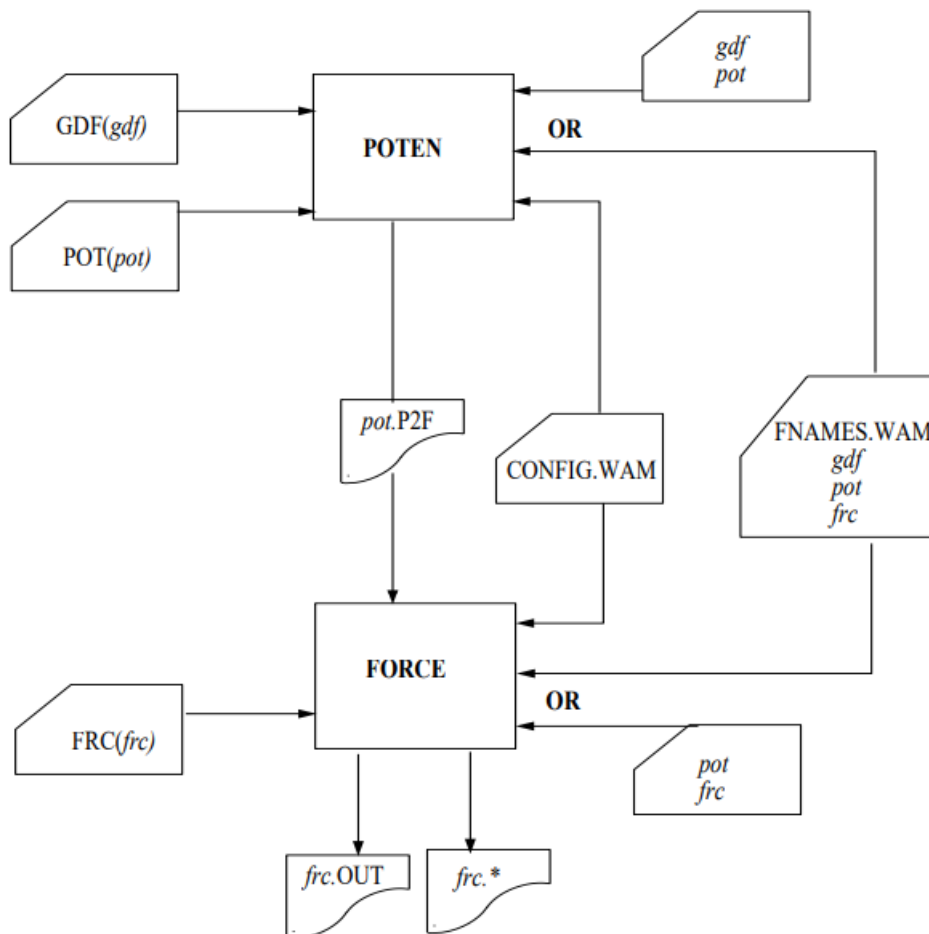


Figure 4.2: Flowchart of WAMIT showing the subprograms POTEN and FORCE with their associated input and output files [25].

---

## 4.2 Theory

### 4.2.1 The boundary-value problem in WAMIT

WAMIT assumes potential flow, so the flow velocity can be defined by the gradient of the velocity potential  $\Phi$  satisfying the Laplace equation in the fluid domain

$$\nabla^2 \Phi = 0.$$

Due to harmonic time dependence, it is allowed to define the complex velocity potential  $\varphi$  as

$$\Phi = \text{Re}(\varphi e^{i\omega t}),$$

where  $\text{Re}$  is the real part,  $\omega$  is the frequency of the incident wave and  $t$  is time. The linearized free-surface condition is

$$\varphi_z - K\varphi = 0 \quad \text{on} \quad z = 0,$$

where  $K = \omega^2 / g$  is the infinite-depth wave number and  $g$  is the gravitational acceleration. The velocity potential of the incident wave in WAMIT, is defined as

$$\varphi_0 = \frac{igA}{\omega} \frac{\cosh[k(z+H)]}{\cosh kH} e^{-ikx \cos \beta - iky \sin \beta},$$

where  $\beta$  is the angle between the direction of the propagating incident wave and the positive X-axis and  $k$  is the real root of the dispersion relation

$$\frac{\omega^2}{g} = k \tanh kH.$$

The linearization of the boundary-value problem makes it possible to divide the velocity potential  $\varphi$  into radiation and diffraction as

$$\varphi = \varphi_R + \varphi_D,$$

$$\varphi_R = i\omega \sum_{j=1}^6 \xi_j \varphi_j,$$

$$\varphi_D = \varphi_0 + \varphi_S.$$

Here,  $\xi_j$  is the complex amplitude of the body motions in the six degree of freedom,  $\varphi_j$  is the corresponding unit-amplitude radiation potentials.  $\varphi_s$  is the velocity potential of the scattered disturbance of the incident wave [25].

### 4.2.2 Added mass and damping coefficients

The non-dimensional added mass and damping coefficients provided by WAMIT are found in Equation 4.1.

---


$$\begin{aligned}
A_{ij} - \frac{i}{\omega} B_{ij} &= \rho \iint_{S_B} n_i \varphi_j dS \\
\bar{A}_{ij} &= \frac{A_{ij}}{\rho L^k} & \bar{B}_{ij} &= \frac{B_{ij}}{\rho L^k \omega}
\end{aligned} \tag{4.1}$$

where  $S_b$  is the mean wetted surface area and  $L^k$  is the *ULEN*-parameter, which is set to 1 meter in this thesis, and

$$\begin{aligned}
k = 3 & \text{ for } i, j = 1, 2, 3 \\
k = 4 & \text{ for } i = 1, 2, 3, j = 4, 5, 6 \quad \text{or} \quad i = 4, 5, 6, j = 1, 2, 3 \\
k = 5 & \text{ for } i, j = 4, 5, 6.
\end{aligned}$$

### 4.2.3 Exciting forces

The exciting forces from the Haskind relations is given as

$$X_i = -i\omega\rho \iint_{S_b} \left( n_i \varphi_0 - \varphi_i \frac{\partial \varphi_0}{\partial n} \right) dS. \tag{4.2}$$

Exciting forces from direct integration of hydrodynamic pressure is given as

$$\begin{aligned}
X_i &= -i\omega\rho \iint_{S_b} n_i \varphi_D dS \\
\tilde{X}_i &= \frac{X_i}{\rho g A L^m}
\end{aligned} \tag{4.3}$$

where  $m = 2$  for  $i = 1, 2, 3$  and  $m = 4, 5, 6$ . It is possible to calculate the Froude-Krylov and scattering components of the exciting forces in WAMIT directly by using IOPTN(2)=2 and IOPTN(3) = 2 in the *.frc*-file.

### 4.2.4 Body motion and free surface elevation

The non-dimensional body motions and free surface elevation are given by

$$\bar{\xi}_i = \frac{\xi_i}{A/L^n} \quad \bar{\eta} = \frac{\eta}{\xi_j L^n} = KL\bar{\varphi}_j \tag{4.4}$$

where  $K = \omega^2/g$ ,  $\varphi$  is the total velocity potential,  $n = 0$  for  $i, j = 1, 2, 3$  and  $n = 1$  for  $i, j = 4, 5, 6$ .

## 4.3 Input and output files

A description of the different input files follows.



---

|                     |   |
|---------------------|---|
| <b>'fnames.wam'</b> | The file specifying the input filenames that WAMIT reads (POTEN reads).                                       |
| <b>.pot</b>         | The Potential Control File.   |
| <b>'frc'</b>        | The Force Control File. This specifies the non-geometric inputs for WAMIT.                                    |
| <b>'CONFIG.WAM-</b> | This file is necessary for finding the path and reading files WAMIT uses. This is only needed for WAMIT 7.    |
| <b>'gdf'</b>        | The Geometric Data File that defines the coordinates of the panel vertices, so the mesh of the configuration. |
| <b>'userid.wam'</b> | The license file.   |

Table 4.1: Input files for WAMIT [25].

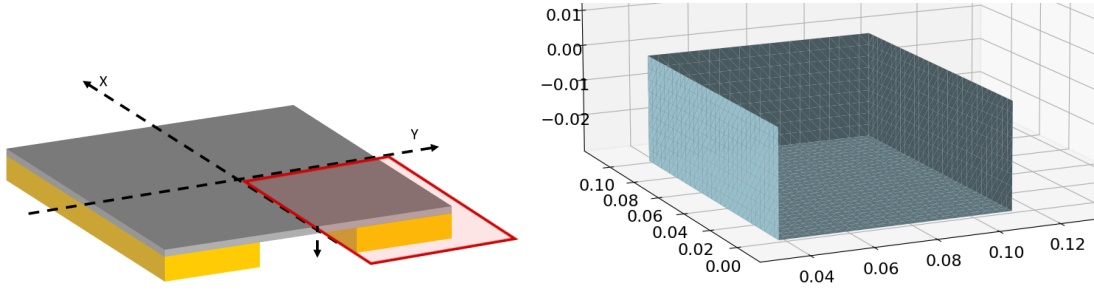
|           |      |                   |                   |                           |                            |                            |                           |                           |  |
|-----------|------|-------------------|-------------------|---------------------------|----------------------------|----------------------------|---------------------------|---------------------------|--|
| OPTN.1:   | PER  | I                 | J                 | $\bar{A}_{ij}$            | $\bar{B}_{ij}$             |                            |                           |                           |  |
| OPTN.2:   | PER  | BETA              | I                 | $\text{Mod}(\bar{X}_i)$   | $\text{Pha}(\bar{X}_i)$    | $\text{Re}(\bar{X}_i)$     | $\text{Im}(\bar{X}_i)$    |                           |  |
| OPTN.3:   | PER  | BETA              | I                 | $\text{Mod}(\bar{X}_i)$   | $\text{Pha}(\bar{X}_i)$    | $\text{Re}(\bar{X}_i)$     | $\text{Im}(\bar{X}_i)$    |                           |  |
| OPTN.4:   | PER  | BETA              | I                 | $\text{Mod}(\bar{\xi}_i)$ | $\text{Pha}(\bar{\xi}_i)$  | $\text{Re}(\bar{\xi}_i)$   | $\text{Im}(\bar{\xi}_i)$  |                           |  |
| OPTN.5P:  | PER  | BETA              | M K               | $\text{Mod}(\bar{p})$     | $\text{Pha}(\bar{p})$      | $\text{Re}(\bar{p})$       | $\text{Im}(\bar{p})$      |                           |  |
| OPTN.5VX: | PER  | BETA              | M K               | $\text{Mod}(\bar{V}_x)$   | $\text{Pha}(\bar{V}_x)$    | $\text{Re}(\bar{V}_x)$     | $\text{Im}(\bar{V}_x)$    |                           |  |
| OPTN.5VY: | PER  | BETA              | M K               | $\text{Mod}(\bar{V}_y)$   | $\text{Pha}(\bar{V}_y)$    | $\text{Re}(\bar{V}_y)$     | $\text{Im}(\bar{V}_y)$    |                           |  |
| OPTN.5VZ: | PER  | BETA              | M K               | $\text{Mod}(\bar{V}_z)$   | $\text{Pha}(\bar{V}_z)$    | $\text{Re}(\bar{V}_z)$     | $\text{Im}(\bar{V}_z)$    |                           |  |
| OPTN.6P:  | PER  | BETA              | L                 | $\text{Mod}(\bar{p})$     | $\text{Pha}(\bar{p})$      | $\text{Re}(\bar{p})$       | $\text{Im}(\bar{p})$      |                           |  |
| OPTN.6VX: | PER  | BETA              | L                 | $\text{Mod}(\bar{V}_x)$   | $\text{Pha}(\bar{V}_x)$    | $\text{Re}(\bar{V}_x)$     | $\text{Im}(\bar{V}_x)$    |                           |  |
| OPTN.6VY: | PER  | BETA              | L                 | $\text{Mod}(\bar{V}_y)$   | $\text{Pha}(\bar{V}_y)$    | $\text{Re}(\bar{V}_y)$     | $\text{Im}(\bar{V}_y)$    |                           |  |
| OPTN.6VZ: | PER  | BETA              | L                 | $\text{Mod}(\bar{V}_z)$   | $\text{Pha}(\bar{V}_z)$    | $\text{Re}(\bar{V}_z)$     | $\text{Im}(\bar{V}_z)$    |                           |  |
| OPTN.7:   | PER  | BETA <sub>1</sub> | BETA <sub>2</sub> | I                         | $\text{Mod}(\bar{F}_i)$    | $\text{Pha}(\bar{F}_i)$    | $\text{Re}(\bar{F}_i)$    | $\text{Im}(\bar{F}_i)$    |  |
|           | [PER | BETA <sub>1</sub> | BETA <sub>2</sub> | -I                        | $\text{Mod}(\bar{F}_{io})$ | $\text{Pha}(\bar{F}_{io})$ | $\text{Re}(\bar{F}_{io})$ | $\text{Im}(\bar{F}_{io})$ |  |
| OPTN.8:   | PER  | BETA <sub>1</sub> | BETA <sub>2</sub> | I                         | $\text{Mod}(\bar{F}_i)$    | $\text{Pha}(\bar{F}_i)$    | $\text{Re}(\bar{F}_i)$    | $\text{Im}(\bar{F}_i)$    |  |
| OPTN.9:   | PER  | BETA <sub>1</sub> | BETA <sub>2</sub> | I                         | $\text{Mod}(\bar{F}_i)$    | $\text{Pha}(\bar{F}_i)$    | $\text{Re}(\bar{F}_i)$    | $\text{Im}(\bar{F}_i)$    |  |
|           | [PER | BETA <sub>1</sub> | BETA <sub>2</sub> | -I                        | $\text{Mod}(\bar{F}_{io})$ | $\text{Pha}(\bar{F}_{io})$ | $\text{Re}(\bar{F}_{io})$ | $\text{Im}(\bar{F}_{io})$ |  |

Figure 4.3: Format of the output '.frc' files [25].

The output files are '.frc'-files with the form shown in Figure 4.3. All outputs from WAMIT are dimensionless, and are given in Crestian coordinates.

### 4.3.1 Mesh and the '.gdf' input file

The Geometric Data File describes the geometry of the structure that is analyzed. The dimensions are in meters and the centre is at the free surface with the negative Z-axis oriented down. Due to symmetry, one can mirror the structure in terms of the X- and Y-axis. This means that if there is symmetry about the X- and Y-axis, one needs to generate a mesh for one quarter of the cube only. Consequently, one quarter of the total mesh is sufficient for the geometries in this thesis. To obtain a sufficient WAMIT analysis, the input structure in the '.gdf'-file should have a refinement of a minimum of 10 sub-panels per main panel. A mesh refinement study presenting a sufficient mesh refinement is conducted in Section 4.4. The section that is mirrored in WAMIT is illustrated in Figure 4.4.



(a) The model mirrored about the X- and Y-axis. (b) Visualisation of one quarter of the structure before mirroring.

Figure 4.4: A visualization of the model with case 1 gap distance 7.5 cm between the floaters. The section marked red, is the quarter that is mirrored about the X- and Y-axis. The right figure is a visualization of the finest `.gdf`-file used, which is refinement `'G22'`, consequently 9 panels per cm.

### 4.3.2 Mass matrix and the `.frc` input file

The Force Control File specifies the options one would like to simulate, and are shown in (Figure 4.1). The `.frc`-file specifies the value of density  $\rho$ , vertical centre of gravity, the mass-, hydrostatic damping- and hydrostatic stiffness matrix, and lastly the coordinates one would like to estimate either velocity flow or hydrodynamic pressure. In the damping- and stiffness matrix, additional damping and stiffness from mooring can be added. If the body is freely floating, instead of moored, these should be set to zero. The inertia matrix is defined as

$$M = \begin{pmatrix} m & 0 & 0 & 0 & mz_g & -my_g \\ 0 & m & 0 & -mz_g & 0 & mx_g \\ 0 & 0 & m & my_g & -mx_g & 0 \\ 0 & -mz_g & my_g & I_{11} & I_{12} & I_{13} \\ mz_g & 0 & -mx_g & I_{21} & I_{22} & I_{23} \\ -my_g & mx_g & 0 & I_{31} & I_{32} & I_{33} \end{pmatrix}. \quad (4.5)$$

where the moment of inertia  $I_{ij}$  are defined in terms of the radii of gyration  $r_{ij}$ ,

$$I_{ij} = \rho \nabla r_{ij} |r_{ij}|. \quad (4.6)$$

The radii of gyration are calculated from  $r_{ij} = \sqrt{\frac{I_{ij}}{A_{ij}}}$ , where I is the moment of area, and A is the cross-section area. The second moment of area for the small cylinder and the correlated radii can be calculated as

$$\begin{aligned}
I_{xx} &= \int_{-y/2}^{y/2} \int_0^z y^2 + z^2 dz dy = \frac{1}{12}y^3z + \frac{1}{3}yz^3 \\
I_{yy} &= \int_{-x/2}^{x/2} \int_0^z x^2 + z^2 dz dx = \frac{1}{12}x^3z + \frac{1}{3}xz^3 \\
I_{zz} &= \int_{-y/2}^{y/2} \int_{-x/2}^{x/2} x^2 + y^2 dx dy = \frac{1}{12}(x^3y + xy^3)
\end{aligned} \tag{4.7}$$

$$\begin{aligned}
r_{xx} &= \sqrt{\frac{I_{xx}}{A_{xx}}} = \sqrt{\frac{1}{12}y^2 + \frac{1}{3}z^2} \\
r_{yy} &= \sqrt{\frac{I_{yy}}{A_{yy}}} = \sqrt{\frac{1}{12}x^2 + \frac{1}{3}z^2} \\
r_{zz} &= \sqrt{\frac{I_{zz}}{A_{zz}}} = \sqrt{\frac{1}{12}(y^2 + x^2)}
\end{aligned} \tag{4.8}$$

The inertia matrix changes with different configurations.

Consider the large catamaran-shaped floater with a body mass equal to the submerged mass  $m = \rho\nabla$ . The length, width, and height equals 0.2m, 0.075m, and 0.03m, and origo in the middle of the square at the free surface,  $(x, y, z = 0) = (0.10, 0.0375, 0)$ . The centre of gravity for this simple floater with  $H/L = 0.15$ , is at  $(x_g, y_g, z_g) = (0, 0, -H/2)$ . As the inertia matrix is defined by the coordinates to the centre of gravity,  $x_g$  and  $y_g$  can be set to zero. Due to summitry  $I_{12}, I_{13}, I_{21}, I_{23}, I_{31}, I_{32}$  becomes zero. The mass matrix is now much simpler.

$$M = \begin{pmatrix} m & 0 & 0 & 0 & mz_g & 0 \\ 0 & m & 0 & -mz_g & 0 & 0 \\ 0 & 0 & m & 0 & 0 & 0 \\ 0 & -mz_g & 0 & I_{11} & 0 & 0 \\ mz_g & 0 & 0 & 0 & I_{22} & 0 \\ 0 & 0 & 0 & 0 & 0 & I_{33} \end{pmatrix}. \tag{4.9}$$

When implementing the values for body mass, coordinates, and radii of gyration, the inertia matrix for the large-draft model with  $H/L = 0.15$ , becomes

$$M = \begin{pmatrix} 0.45 & 0 & 0 & 0 & -0.00675 & 0 \\ 0 & 0.45 & 0 & 0.00675 & 0 & 0 \\ 0 & 0 & 0.45 & 0 & 0 & 0 \\ 0 & 0.00675 & 0 & 3.5e-4 & 0 & 0 \\ -0.00675 & 0 & 0 & 0 & 16.4e-4 & 0 \\ 0 & 0 & 0 & 0 & 0 & 43.1e-4 \end{pmatrix}. \tag{4.10}$$

## 4.4 Refinement study

A grid and wave refinement study of the largest module is conducted. The purpose of these tests are to ensure that the input values are sufficient to produce converged

---

output values. The methodology, along with the final refinement values, is presented in the following section.

#### 4.4.1 Mesh refinement

Here, the refinement of the grid is defined by the number of panels per cm. The roughest grid is 1 panel per cm and the finest is 9 grids per cm. Table 4.2 specifies the grid refinements that are tested and their refinement along their respective axis. A visual representation of the mesh with the coarsest and finest grid can be found in Figure 4.5. An overview of the visualization of all resolutions for the large-draft model before mirroring can be found in Appendix C. The added mass coefficient in surge  $C_{A11}$  of the large-draft model with the coarse grid is plotted for wave period 0-3 seconds, and is found in Figure 4.6.

| Name | Refinement  |             |             |
|------|-------------|-------------|-------------|
|      | x-direction | y-direction | z-direction |
| G2   | 2           | 3           | 1           |
| G4   | 4           | 5           | 2           |
| G8   | 8           | 10          | 3           |
| G15  | 15          | 20          | 6           |
| G22  | 22          | 30          | 9           |

Table 4.2: Grid refinements in X-, Y- and Z-direction before mirroring that was tested for convergence study.

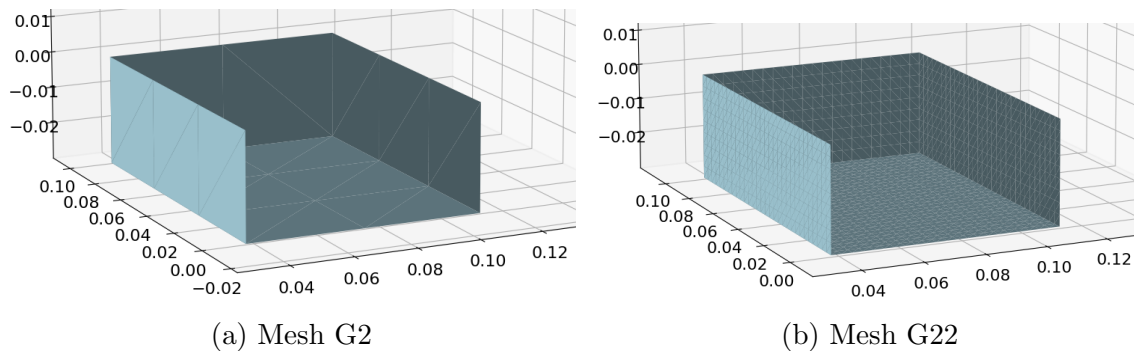
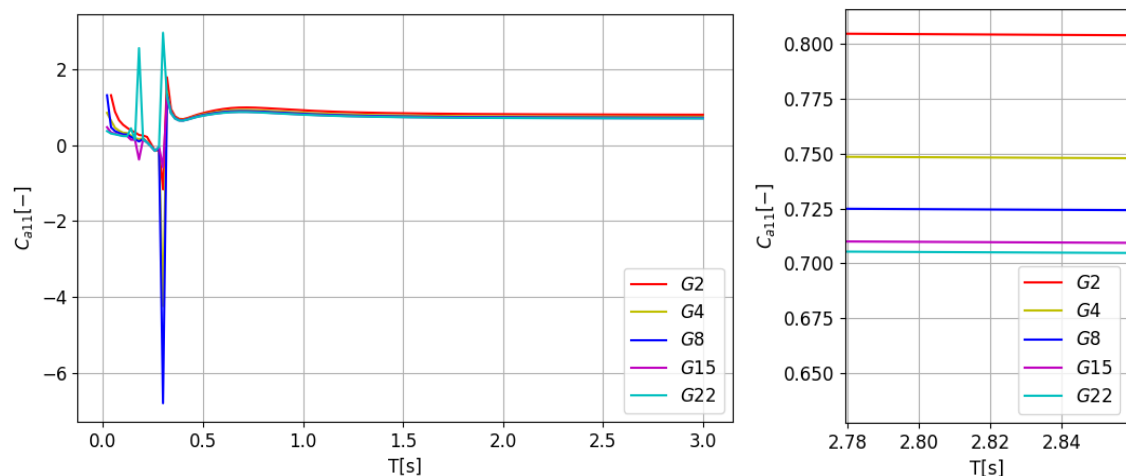


Figure 4.5: A visual representation of the most coarse and refined mesh tested for the convergence study. These are visualized before mirroring.



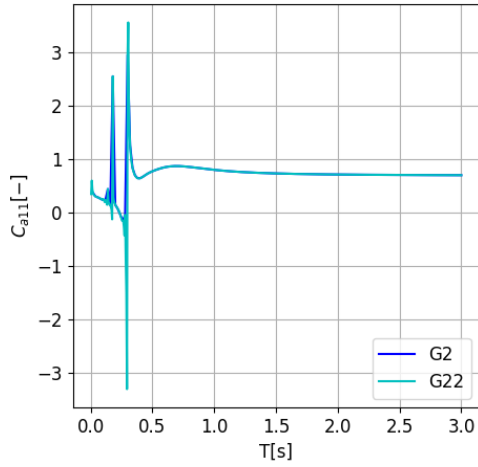
(a) The added mass coefficient  $C_{A11}$  plotted for period  $T \leq 3$  seconds. (b)  $C_{A11}$  plotted for long-crested waves and close to convergence.

Figure 4.6: The added mass coefficient for surge motion  $C_{A11}$  plotted for period  $T$  for the large-draft model with gap distance as case 1,  $H/b = 3/7.5$ . The sensitivity study is conducted using the coarse grid refinement of 1 panel per cm. The added mass coefficient in surge,  $C_{A11}$ , is plotted period  $T \leq 3$  seconds and close to convergence.

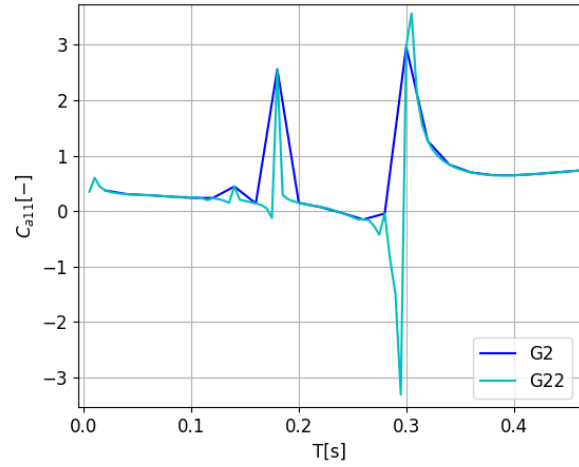
From Figure 4.6, it is seen that the added mass coefficient in surge starts to converge with the finest grid. The difference is small when increasing grids per cm before mirroring from 6 to 9. It is also shown that using nine grids per cm is sufficient for the smallest gap distance between the floaters. This means that it is sufficient to use nine grids per cm before mirroring, and grid size  $G22$  is used for further analysis.

#### 4.4.2 Wave refinement

The wave period increment used to this point, is 1/10 second. This period increment results in some harsh measurements for wave period less than 1 second. This thesis focuses on long waves, so wave periods above 2 seconds in model scale, are of focus. Although periods above 2 seconds is of main focus, wave periods under 1 second are key to identify sloshing modes that are studied in Section 4.5.1. This means that it is important to have good resolution when validating the numerical results with sloshing modes. The wave period increment is increased from 1/10 second to 1/40 second for period less than 1 second, while the period step for periods of 1-3 seconds remains 1/10 second. The added mass coefficient  $C_{A11}$  is plotted for periods 0-3 seconds, comparing the coarse and fine period increment, which is shown in Figure 4.7.



(a) The added mass coefficient  $C_{A11}$  plotted for period  $T \leq 3$  seconds



(b) The added mass coefficient  $C_{A11}$  plotted for period  $T \leq 0.4$  seconds

Figure 4.7: Sensitivity study of wave period refinement of the large-draft models. Added mass coefficient in surge  $C_{A11}$  plotted  $C_{A11}$  plotted for period  $T \leq 3$  seconds, and period  $T \leq 0.4$  seconds. The gap distance  $b$  between the floaters is 7.5cm,  $H/b = 3/7.5$ .

## 4.5 Verification of numerical results

To verify the accuracy and reliability of the numerical and experimental results, a comparison with relevant theory are presented. The numerical findings are compared to expected results based on theoretical sloshing modes. The numerical finds are compared to the added mass in surge for long-crested waves according to DNV recommended practice, DNV-RP-C205.

### 4.5.1 Sloshing modes

The hydrodynamic data obtained from analysis in WAMIT is expected to show resonance peaks at the sloshing modes. It is complicated to calculate the exact sloshing modes for the case of a three-dimensional catamaran model with a relatively small gap distance between the two bodies.

Bernard Molin provided the sloshing modes for two three-dimensional barges with a certain gap distance. The sloshing modes for these barges are calculated from the simplified equation explained in Section 2.4.5. According to Molin, should the reasonable characteristic length  $B$  to gap distance  $b$  ratio be within  $B/b = [2 - 3]$ . The catamaran width  $B$  is 0.075 cm and the gap distance  $b$  varies between 0.075cm and 0.15 cm. The width-to-gap distance ratio for the catamarans becomes  $B/b = [1 - 0.5]$ . The width-to-gap distance ratio is outside the range of what Molin's simplified equation qualifies as reasonable. This contributes to the offset in the correlation of the sloshing modes and their respective resonance peaks.

To visualize the sloshing periods, dimensionless added mass in surge is presented for large catamarans with the three gap distance configurations. Additionally, a comparison is made with the added mass in surge for two catamaran-shaped bodies that are sufficiently distant from each other, not affecting one another.

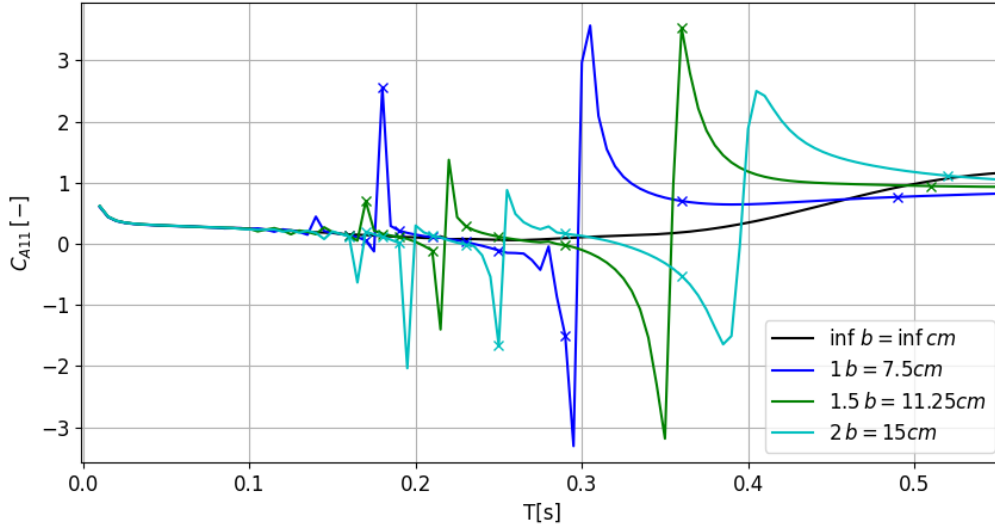


Figure 4.8: Added mass coefficient  $C_{A11}$  is plotted for  $T < 0.5$  seconds. The catamaran-shaped models are investigated with four gap distance configurations. The crosses mark is the sloshing periods calculated from Molin [21].

Figure 4.8 shows the added mass coefficient  $C_{A11}$  for the large-draft models, and are plotted for period  $T < 0.5$  seconds. Molin's estimation of the sloshing modes are also plotted.  $C_{A11}$  are plotted for three gap distance configurations, in addition to the infinite gap distance that is denoted 'inf  $b$ '.

It is shown in Figure 4.8 that Molin's simplifies equation for sloshing modes indicates where the peaks should be, and seems to correlate with some resonance peaks as it over-predict. As discussed in Section 2.4.5, the lowest frequency is predicted to be at the largest resonance peak. As the lowest sloshing frequency is the largest sloshing period, it is expected to find the largest excitation peak at the crosses around  $T = 0.5s$ . It is evident that there is some offset to this method for the case in this thesis, but it is sufficient to validate that the expected sloshing occurs for periods lower than 0.5s in model scale.

## 4.5.2 Added mass DNV

DET NORSKE VERITAS (DNV) is an independent foundation that undertakes classification, certification and other verification of offshore and onshore industries worldwide [26]. DNV has published their nondimensional added mass coefficients for different bodies in Appendix D of the paper "DNV-RP-C205: Environmental Conditions and Environmental Loads" [26]. This compares the nondimensional

---

added mass coefficients for long-crested waves obtained from analysis in WAMIT. The three-dimensional added mass coefficient from DNV is expected to be a slightly higher estimate compared to the result from WAMIT, as it is somewhat more accurate in its estimation.

In Appendix D, the analytical added mass coefficient is calculated. In this elaboration, the analytical added mass coefficient for two-dimensional is calculated. When converting to a three-dimensional added mass coefficient, a reduction is expected. It is expected that the correction would result in an over-predicted estimate.

A comparison of the analytical added mass of two-dimensional and the converged result from the WAMIT analysis is found in Table 4.3.

|                   | $C_{A11}$ [H/b = 1.5/7.5] | $C_{A11}$ [H/b = 3/7.5] |
|-------------------|---------------------------|-------------------------|
| Two-dimensional   | 0.717 [-]                 | 1.269 [-]               |
| Three-dimensional | 0.559                     | 0.793                   |
| WAMIT             | 0.49                      | 0.8                     |

Table 4.3: Comparison of numerical added mass coefficient from WAMIT and analytical added mass coefficient calculated estimated from appendix D in *DNV-RP-C205* [26].



# Chapter 5

## Post-Processing

The focus of this chapter is to present the choices made when post-processing data obtained from both the numerical and experimental analysis. The hammer test aims to establish the eigenfrequencies of the rig. A selection of the hammer strikes is presented in this section, while all can be found in Appendix J.

### 5.1 Hammer test

The data from an experiment may be overshadowed at frequencies that are dominated by vibrations. These vibrations may be due to eigenfrequencies or oscillations due to the strike of the hammer, the last one is especially noticeable for the stuck in X-direction on the plate. It is important to obtain an understanding of the frequencies that are expected to experience these vibrations that may overshadow data from the experiment.

The natural frequency of the oscillation experienced after striking the experimental setup with the hammer, is propositional with mass Equation 2.10. This leads to the assumption that the distance between the models does not significantly affect the results, consequently, distance configurations was not tested when performing the hammer test. The distance between the models was set to one floater width distance,  $1b = 0.075\text{m}$  for the hammer test. Furthermore, it is interesting to establish how increasing the thickness of the models, and the weight of the models, affect the response of the hammer test. The spectral density is expected to move towards lower frequencies with increasing mass.

The results of the hammer test are presented as a spectrum analysis. As explained in Section 3.4.2, everything above 40Hz is filtered, consequently, the dominating electrical noise expected at 50Hz is filtered. This thesis presents experimental results for forces in the Z-direction and frequencies 1-5Hz. Consequently, it is interesting to establish the eigenfrequencies of the experimental setup and note peaks of interest within 1-40Hz with a focus on the Z-direction.

The outer plate is expected to oscillate with a lower frequency than the inner plate

due to its larger mass, as explained in Section 3.4.2. Since the outer plate oscillated at lower frequencies, it is used for the primary analysis of the hammer test. One exception to analyzing only the outer plate, is when striking the outer plate with the hammer. The outer plate oscillates due to the hammer striking, and the inner plate is analyzed to avoid the oscillations due to the strike. It should be noted that the magnitude of the peaks varies with the force applied to the hammer struck.

### 5.1.1 Comparing outer and inner plate

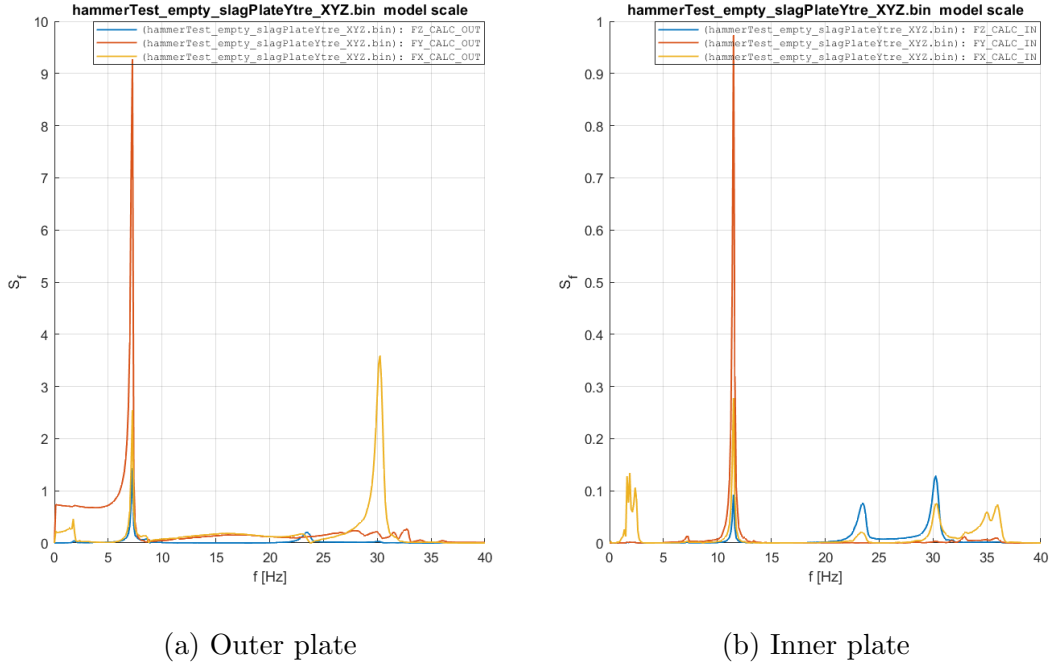


Figure 5.1: The spectra analysis of the force measured on outer and inner plate without models, when striking the outer plate in Y-direction.

Figure 5.1 shows the spectra analysis of the force measured on outer and inner plates when striking the outer plate in the Y-direction. By comparing these two figures, one can establish the eigenfrequencies of the two plates. The comparison is without the models.

In Figure 5.1, dominant peaks at 6Hz and 11Hz can be seen. The larger mass of the outer plate causes the eigenfrequency of the plate to occur at a lower frequency than for the inner plate. From this point, only the Z-forces are presented.

### 5.1.2 Empty plate

To establish how the rig behaves by itself, a hammer test is performed on a rig with the plate attached without the models, focusing on the outer plate. Some trends can be noticed throughout the hammer test for the empty plate. Significant

peaks in  $F_Z$  at 7Hz and 24Hz are found to be common throughout the test. A peak was sometimes visible at 2-3Hz when striking the hammer in X-and Y-direction. When striking the plates, a peak at 11-12Hz was visible as well. Figure 5.2 shows the spectral analysis of the hammer test of the empty rig, when striking the rig in Y- and Z-direction, and the outer and inner plate when striking the outer plate in Y-direction.

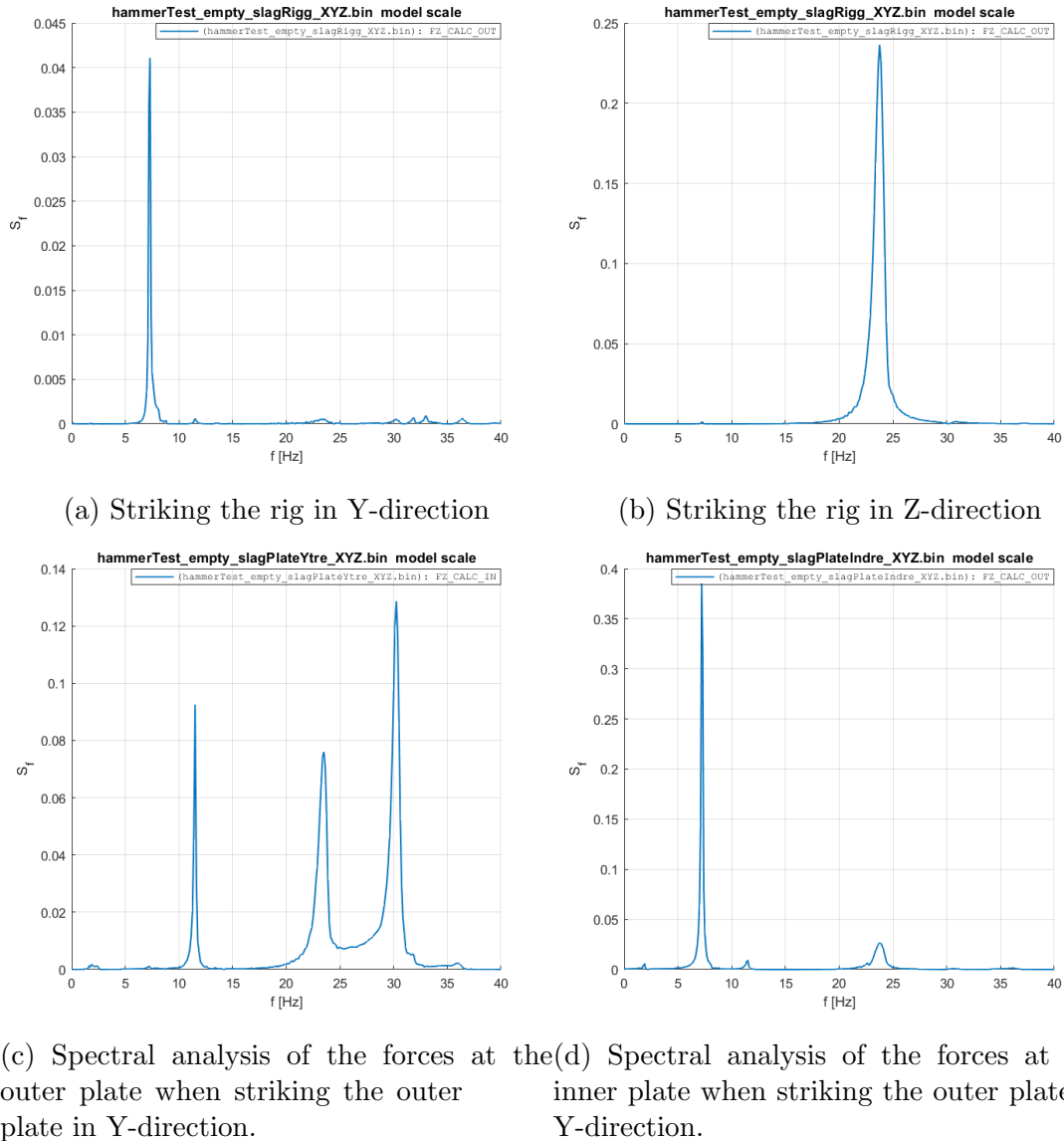
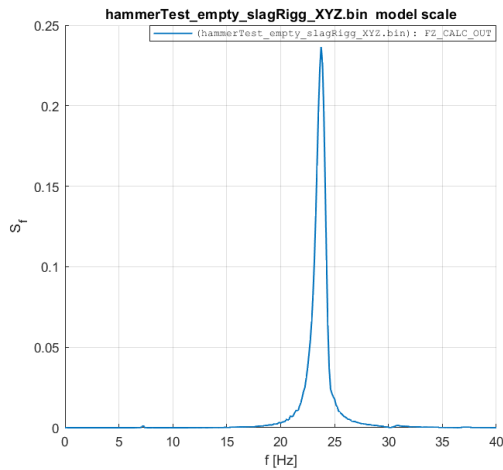


Figure 5.2: Spectral analysis of the forces in Z-direction when striking the experimental setup without models in Y- and Z-direction.

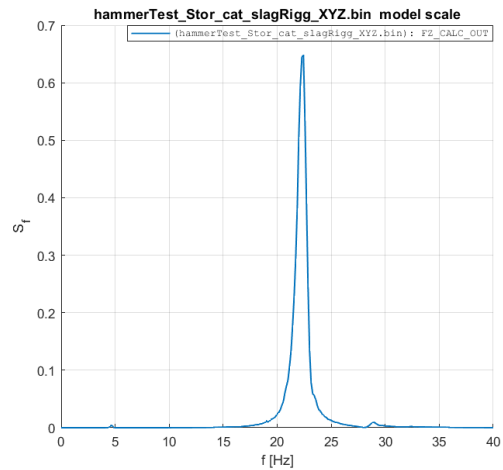
### 5.1.3 Small- and large-draft models

When analyzing the responses of the hammer test with the small- and large-draft models attached, one can see from Figure 5.3 that the response tendencies are similar to the empty plate. The main difference is that the responses shift towards lower frequencies when increasing the weight. This is identified by noticing that

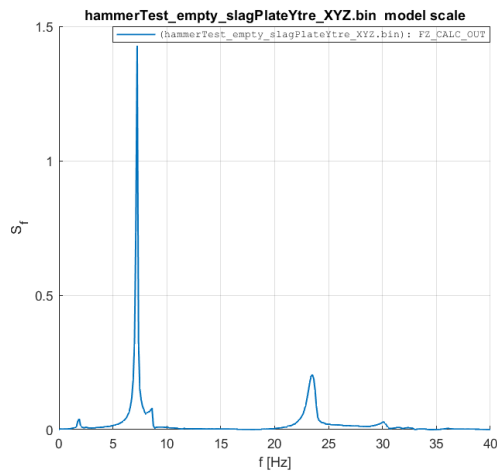
the significant peaks are at 7Hz and 24Hz for the empty plate, then at about 5.5Hz and 23Hz for the small-draft models, and then finally at 4.7Hz and 22Hz for the large-draft models. Figure 5.3 shows the spectral analysis of the hammer test of the rig with small- and large-draft models attached. The hammer struck the rig in the Z-direction, and the outer plate when striking the outer plate in the Y-direction.



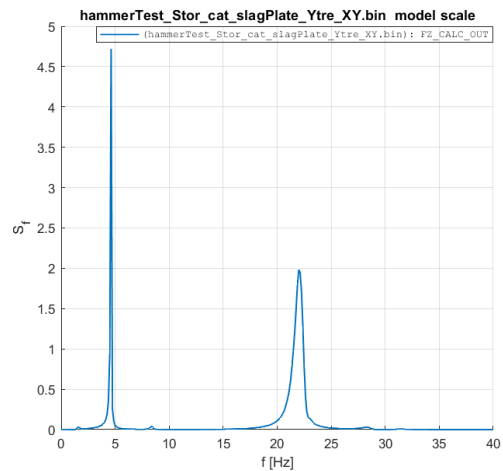
(a) Spectral analysis of the forces when striking the rig with small-draft models in Z-direction



(b) Spectral analysis of the forces when striking the rig with large-draft models in Z-direction



(c) Spectral analysis of the forces measured at the outer plate, when striking the outer plate in Y-direction. With small-draft models



(d) Spectral analysis of the forces measured at the outer plate, when striking the outer plate in Y-direction. With large-draft models

Figure 5.3: Spectral analysis of the forces in Z-direction when striking the experimental setup with small- and large-draft models in Y- and Z-direction.

# Chapter 6

## Result and discussion

In this section, the results from the numerical analysis and the experiment are presented, along with a comparison. These are presented case by case to identify changes experienced when increasing the distance between the floaters and the change with increased draft.

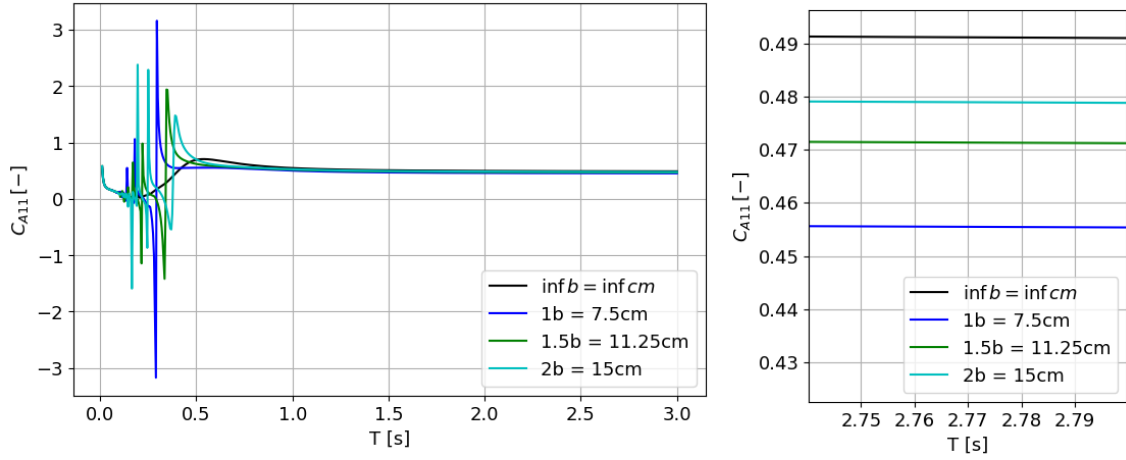
As specified earlier, gap distance  $b$  has the value of one width  $B = 0.075$  m. This means that  $1b = 0.075$  m,  $1.5b = 11.25$  m and  $2b = 0.15$  m.

### 6.1 Numerical analysis - WAMIT

The main focus of the numerical analysis is to study the added mass coefficient  $C_A$ , and the exciting forces, in addition to the damping coefficient  $C_B$ , for short-crested waves. The exciting forces are presented as the total excitation, Froude-Krylov forces, and scattering forces. All analysis is run with the finest grid, "G22", which has nine panels per centimeter. The period increment of the analysis is 1/40 second for period 0-1 second, and 1/10 second for period 1-3 seconds.

## 6.1.1 Added mass coefficient

### 6.1.1.1 Small-draft models



(a) The added mass coefficient  $C_{A11}$  plotted for period  $T \leq 3$  seconds.

(b) The added mass coefficient  $C_{A11}$  plotted for long crested waves and close to convergence.

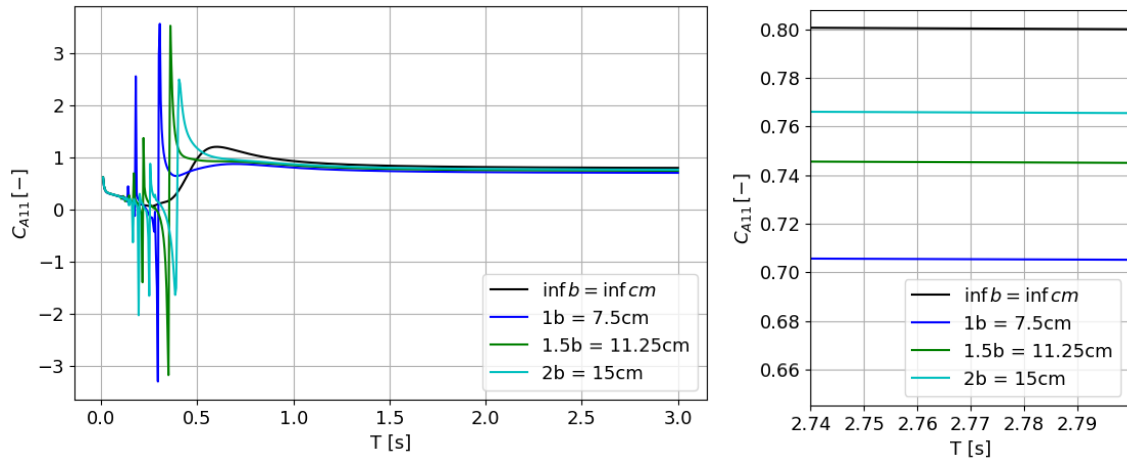
Figure 6.1: The added mass coefficient in surge  $C_{A11}$  for the small-draft models analysed in WAMIT.  $C_{A11}$  is plotted with three gap distance configurations, in addition to the infinite gap distance that is denoted '*inf b*'.

Figure 6.1 shows the added mass coefficient  $C_{A11}$  for the small-draft models, and are plotted for period  $T < 3$  seconds.  $C_{A11}$  are plotted for three gap distance configurations, in addition to the infinite gap distance that is denoted '*inf b*'.

The small-draft models in surge motion experience sloshing for period  $T < 0.5$  seconds.  $C_{A11}$  converges at period of 3 seconds. The distance  $1b$  results in the smallest value, while infinite distance results in the largest. With the increasing distance,  $C_{A11}$  goes towards infinite distance. There is about 5% increase from distance  $1b$  to distance  $2b$ , and 2% increase from  $1.5b$  to  $2b$ . This bears a resemblance to the findings of B. Havel, H. Hangang, and R. Martinuzzi [12].

The sloshing peaks at period  $T < 0.5$  seconds, decreases with increasing distance. The floaters that are infinitely far away from each other are a reference. It can be observed that the infinite distance only has one peak in the  $C_{A11}$  at around 0.55 second period.

### 6.1.1.2 Large-draft models



(a) The added mass coefficient  $C_{A11}$  plotted for period  $T \leq 3$  seconds.

(b) The added mass coefficient  $C_{A11}$  plotted for long crested waves and close to convergence.

Figure 6.2: The added mass coefficient in surge  $C_{A11}$  for the large-draft models analysed in WAMIT.  $C_{A11}$  is plotted with three gap distance configurations, in addition to the infinite distance that is denoted '*inf b*'.

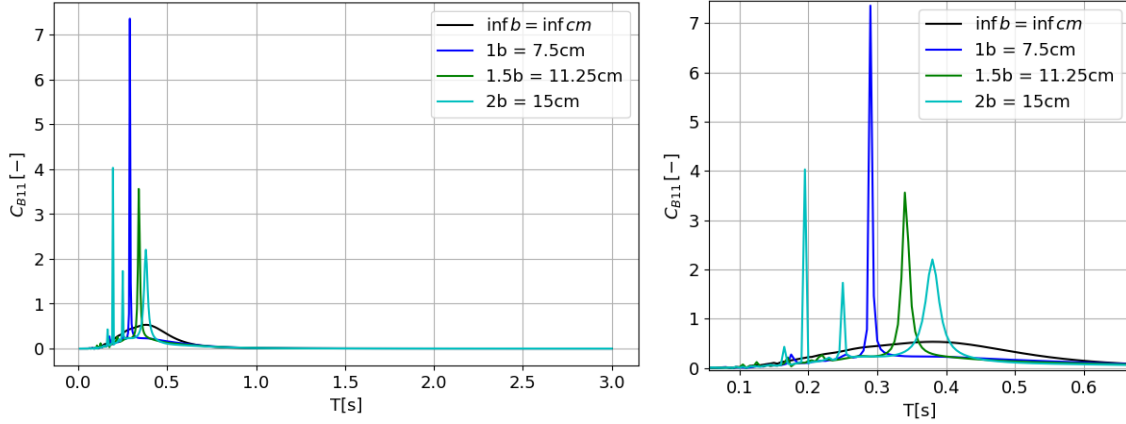
Figure 6.2 shows the  $C_{A11}$  for the large-draft models with four distance configurations, including infinite distance. The same tendencies are shown in this plot as for Figure 6.1, though the values are higher.

The sloshing peaks experienced below 0.5 second, and decreases with increasing distance. The largest decrease is between  $1.5b$  and  $2b$ . The increase in  $C_{A11}$  is around 10% when comparing  $1b$  to  $2b$ , and 3% when comparing  $1.5b$  to  $2b$ .

---

## 6.1.2 Damping coefficients

### 6.1.2.1 small-draft models



(a) The damping coefficient  $C_{B11}$  plotted for period  $T \leq 3$  seconds.

(b) The damping coefficient  $C_{B11}$  plotted for period  $T \leq 0.6$  seconds.

Figure 6.3: The damping coefficient in surge  $C_{B11}$  for the small-draft models analysed in WAMIT.  $C_{B11}$  is plotted with three gap distance configurations, in addition to the infinite gap distance that is denoted '*inf b*'.

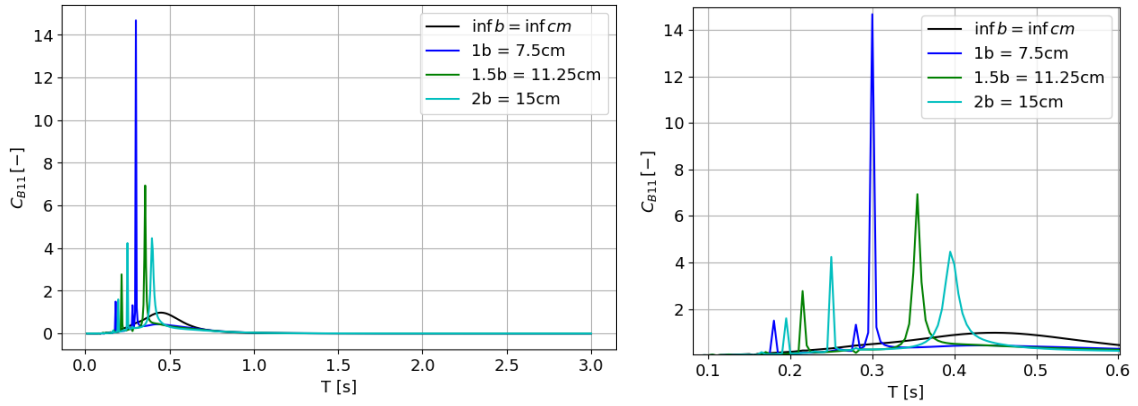
Figure 6.3 shows the damping coefficient  $C_{B11}$  for the small-draft models, and are plotted for period  $T < 3$  seconds.  $C_{B11}$  are plotted for three gap distance configurations, in addition to the infinite gap distance that is denoted "*inf b*".

The damping for the small-draft models, as shown in Figure 6.3, converges quickly. The system damping coefficient is fully damped at 0.7 second period. The sloshing modes are evident for periods up to 0.4 second. The sloshing peaks decrease for increasing distance after 0.3 second periods. The sloshing peaks for distance  $2b$  spikes for periods under 0.3 second. The maximum damping peak is found to be for distance  $1b$  for period 2.9 seconds, and has the value of  $C_{B11} = 7.1$ .



---

### 6.1.2.2 Large-draft models



(a) The damping coefficient  $C_{B11}$  plotted for period  $T \leq 3$  seconds.

(b) The damping coefficient  $C_{B11}$  plotted for period  $T \leq 0.6$  seconds.

Figure 6.4: The damping coefficient in surge  $C_{B11}$  for the large-draft models analysed in WAMIT.  $C_{B11}$  is plotted with three gap distance configurations, in addition to the infinite gap distance that is denoted 'inf b'.

Figure 6.4 shows the damping coefficient  $C_{B11}$  for the large-draft models, and are plotted for period  $T < 3$  seconds.  $C_{B11}$  are plotted for three gap distance configurations, in addition to the infinite gap distance that is denoted "inf b".

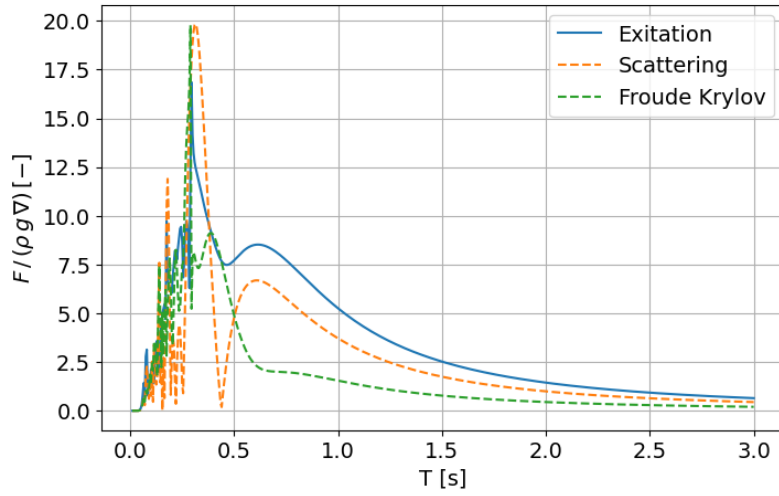
The sloshing modes are evident for periods up to 0.5 seconds. These sloshing peaks increase slightly for the increasing distance between the floater up to 0.30 seconds periods. After 0.3 second periods, the sloshing peaks decrease for increasing distance. The maximum damping coefficient is for distance 1D and period 0.3 second, and is found to be  $C_{B11} = 14.1$ .

### 6.1.3 Exciting forces

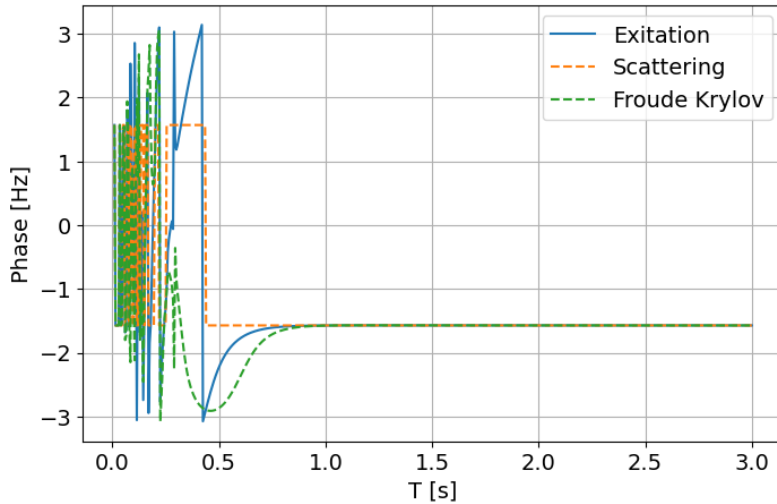
Total excitation forces can be divided into Froude-Krylov forces and the scattering, as explained in Section 2.4. In this section, surge motion for case 1 with small- and large-draft models are presented and analyzed presented. Case 2 and case 3 can be found in Appendix G.

---

### 6.1.3.1 Case 1 - small-draft models

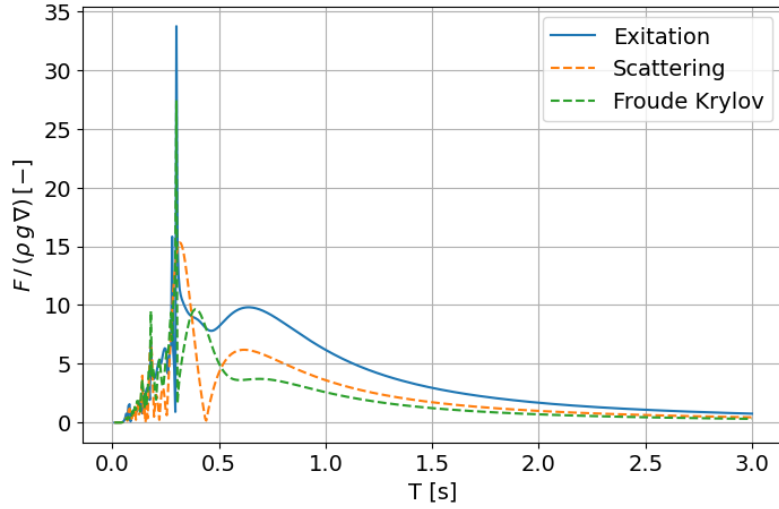


(a) Total excitation force coefficient, Froude-Krylov force coefficient and the scattering force coefficient plotted.

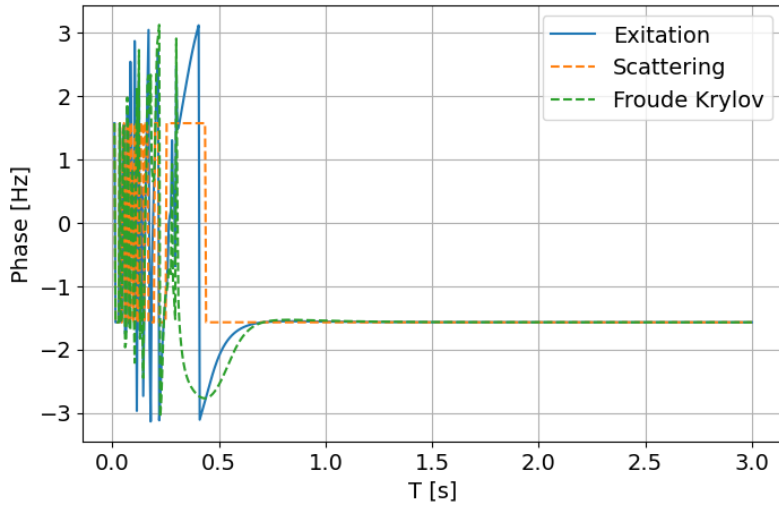


(b) The corresponding phase.

Figure 6.5: Total excitation force coefficient, Froude-Krylov force coefficient, and the scattering force coefficient plotted with the corresponding phase for period  $T \leq 3$  seconds. The case presented is for case 1 gap distance with small-draft models,  $H/b = 1.5/7.5$ .



(a) Total excitation force coefficient, Froude-Krylov force coefficient, and the scattering force coefficient plotted.



(b) The corresponding phase.

Figure 6.6: Total excitation force coefficient, Froude-Krylov force coefficient, and the scattering force coefficient plotted with the corresponding phase for period  $T \leq 3$  seconds. The case presented is case 1 with large-draft models,  $H/b = 3/7.5$ .

Figure 6.5 and Figure 6.6 shows the total excitation force coefficient, Froude-Krylov force coefficient, and the scattering force coefficients, with the corresponding phase, for the small- and large-draft models respectively. These are plotted for period  $T < 3$  seconds.

The same trends are seen for both the small- and large-draft models in Figure 6.5 and Figure 6.6. The main difference is found in the magnitude. The peak at the period of 0.4 second increases from 20 to 34, which is a 70% increase. Note that this peak may be due to sloshing modes. The peak at the period of 0.6 seconds increases from 8.5 to 10, a 17.6% increase. As there are no spikes at this peak, it seems to be more reliable. The phase seems to mostly oscillate within the interval  $[-\frac{\pi}{2}, \frac{\pi}{2}]$ , but still spikes at times. These spikes may be due to some convergence error when

---

conducting the numerical analysis in WAMIT.

## 6.2 Experimental results

This section presents and compares the experimental results to the numerical results. The results are limited to presenting surge for increasing KC numbers, as the experiment only tested hydrodynamic loads in surge. For small KC numbers, such as  $KC \leq 4$ , the added mass is expected to be relatively unaffected by the vortex shedding. While the KC numbers increase, it is likely that added mass, damping, and force component  $F^\omega$  increases as well. As the KC number increases, the experimental values of the hydrodynamic forces are expected to increase faster than the numerical estimation. This may be due to the difference in real and perfect fluid used for experimental and numerical investigation, respectfully. This is investigated in the following section.

The forces are measured at the outer and inner plate and made nondimensional, as explained in Section 2.5. The added mass and drag coefficients,  $C_A$  and  $C_B$ , are presented for the outer and inner plates and the sum of the outer and inner plates. When analysing the force,  $F_I^\omega$  and  $F_O^\omega$ , along with the sum  $F_S^\omega$ , are the primary focus. The sum  $F_S^\omega$  of the outer and inner plate, is accurate to compare with the numerical analysis.

Figure 6.7 shows the force components  $F^\omega$  for cases 1 and 3 for the small- and large-draft models, and are plotted for  $KC \leq 16$ . To get an understanding of the magnitude of the forces that are to be analyzed in this section, cases 1 and 3 are presented for the small- and large-draft models in Figure 6.7. The largest force is measured at case 3 with the small- and large-draft models.

From Figure 6.7, one can see that the measurements are scattered at  $KC < 5$  for the small-draft models. An investigation studying whether or not the boundary layer causes the scatter follows. At page 236 of *Sea loads on ships and offshore structures* by O.M. Faltinsen, there is an expression to estimate the boundary layer thickness [18]. The point of consideration is  $U_0(x)e^{-(\omega/(2\nu))^{1/2}y} = 0.01U_0(x)$ . This corresponds to  $(\omega/(2\nu))^{1/2}y = 4.6$ . With  $\nu = 10^{-6} \text{ m}^2\text{s}^{-1}$  and  $T = 1$  second, the thickness becomes

$$y = \frac{4.6}{\sqrt{\frac{\omega}{2\nu}}} = \frac{4.6}{\sqrt{\frac{2\pi}{2 \cdot 10^{-6}}}} = 2.6 \text{ mm}. \quad (6.1)$$

The boundary layer thickness becomes 2.6 mm. The smallest models of 1.5 cm is well outside the boundary thickness. The scatter may be due to noise. Due to the sensitivity of the small-draft models, all measurements for  $KC < 5$  are discarded.

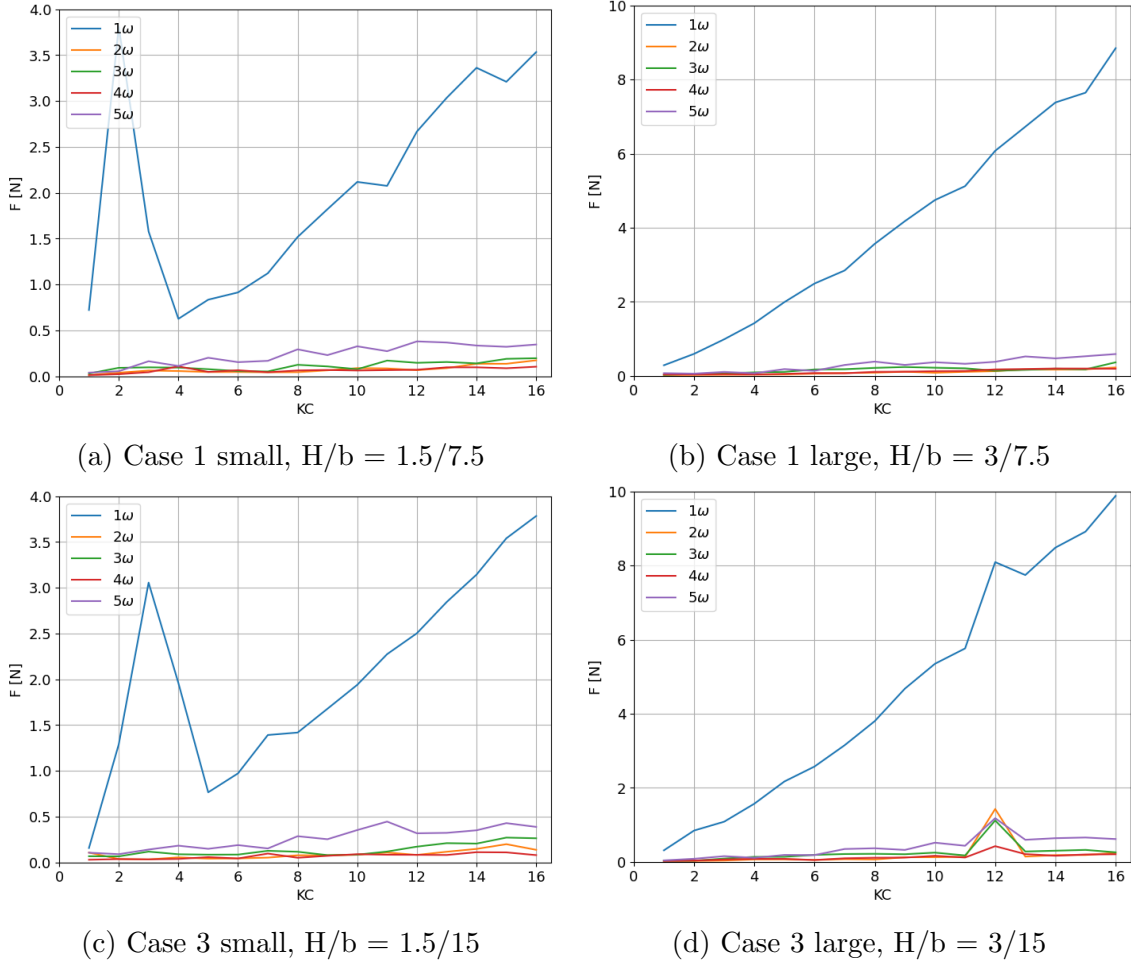
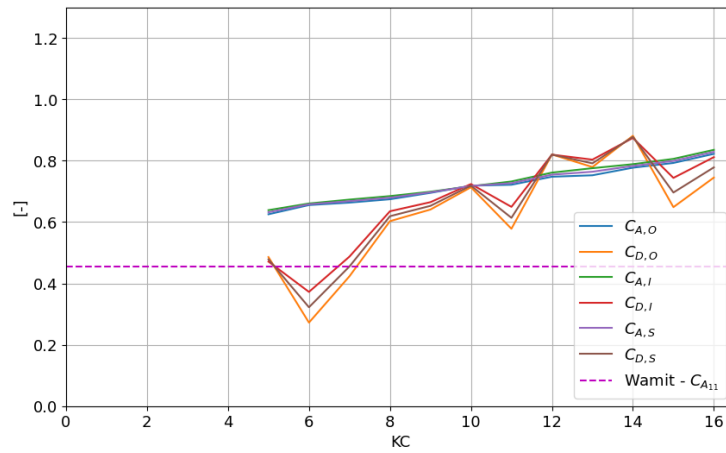


Figure 6.7: the force components  $F^\omega$  for cases 1 and 3 for the small- and large-draft models, and are plotted for  $KC \leq 16$ .

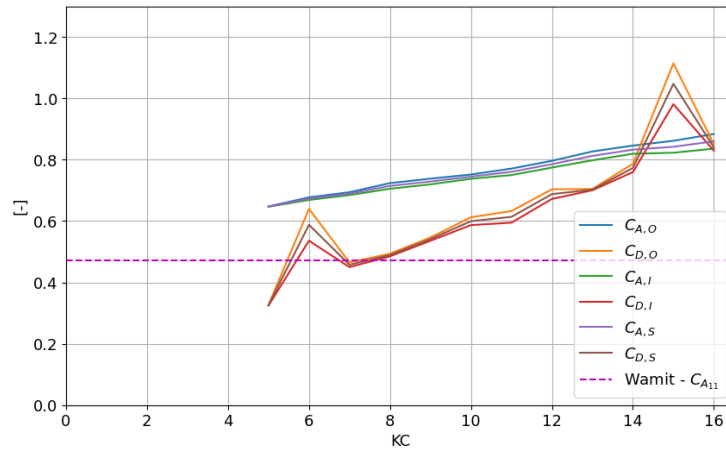
### 6.2.1 Added mass and drag coefficients

In this section, the added mass coefficients  $C_A$  and drag coefficients  $C_D$  from the experiment are discussed, and compared with the numerical added mass coefficient  $C_{A11}$ .  $C_{A11}$  for the small-draft are plotted for  $KC \geq 5$  in Figure 6.8, while plotted for  $KC \leq 16$  in Appendix I

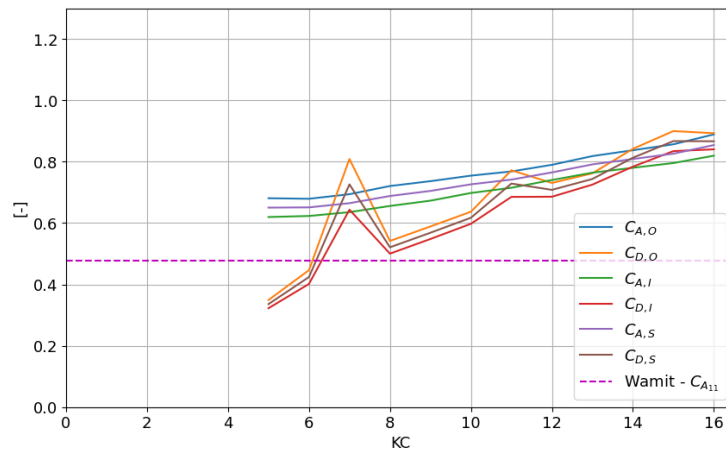
### 6.2.1.1 Small-draft models



(a) Case 1 with small-draft models,  $H/b = 1.5/7.5$



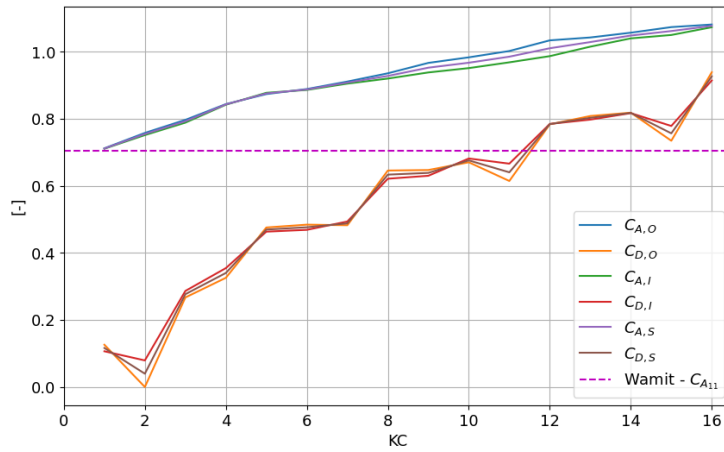
(b) Case 2 with small-draft models,  $H/b = 1.5/11.25$



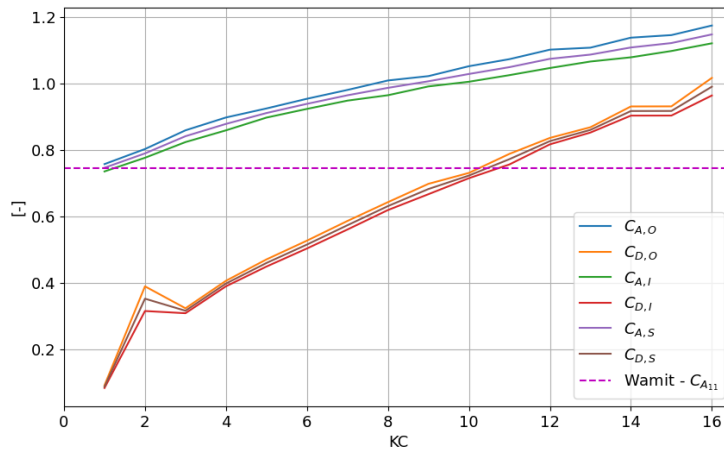
(c) Case 3 with small-draft models,  $H/b = 1.5/15$

Figure 6.8: The added mass  $C_A$  and drag coefficient  $C_D$  of the small-draft models attached to the outer and inner plate, measuring  $C_{A,O}$  and  $C_{A,I}$  plate. The sum  $C_{A,S}$  compared to  $C_{A11}$  from WAMIT.

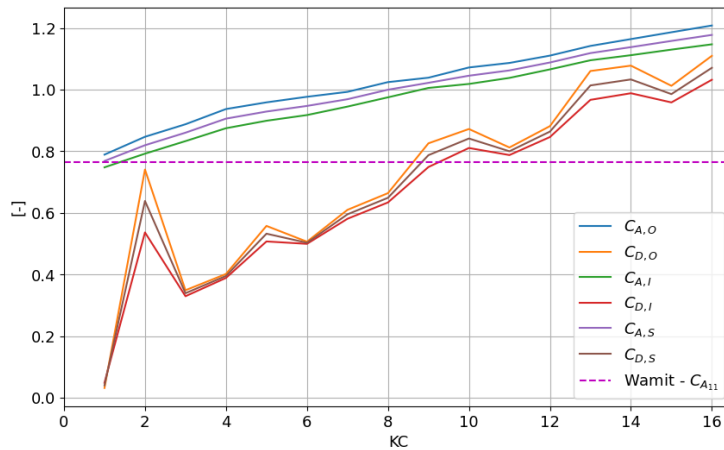
### 6.2.1.2 Large-draft models



(a) Case 1 with large-draft models,  $H/b = 3/7.5$



(b) Case 2 with large-draft models,  $H/b = 3/11.25$



(c) Case 3 with large-draft models,  $H/b = 3/15$

Figure 6.9: The added mass  $C_A$  and drag coefficient  $C_D$  of the small-draft models attached to the outer and inner plate, measuring  $C_{A,O}$  and  $C_{A,I}$ . The sum  $C_{A,S}$  is compared to  $C_{A11}$  from WAMIT.

---

Figure 6.8 and Figure 6.9 show the added mass  $C_A$  and drag coefficient  $C_D$  of the small- and large-draft models, respectively, and are plotted for  $KC \leq 16$ . The models are attached to the outer and inner plates measuring  $C_{A,O}$  and  $C_{A,I}$ . The sum  $C_{A,S}$  is compared to  $C_{A11}$  from WAMIT.

In Figure 6.8, all values for  $KC < 5$  are removed due to noise at low  $KC$  numbers for small-draft models. The added mass coefficient  $C_{A,S}$  should converge towards the numerical estimated value  $C_{A11}$  for  $KC = 0$ , which it seems to do. The measured drag coefficient should go to zero for  $KC = 0$ , as there is no drag when there is no velocity. From Figure 6.8, it can be observed that a fitted line of  $C_{D,S}$  seems to approach zero for  $KC = 0$ .

By comparing the hydrodynamic forces of the small-draft models on the outer and inner plate, one can notice that  $C_{A,O}$  and  $C_{A,I}$  differ more for case 3 than for cases 1 and 2.  $C_{A,O}$  and  $C_{A,I}$  is quite similar at  $KC = 16$  for case 1, while they differ in cases 2 and 3. This indicates that the difference of  $C_{A,O}$  and  $C_{A,I}$  increases with increased  $KC$  number. In Figure 6.8, it can be observed that for  $KC = 16$ ,  $C_{A,S}$  and  $C_{D,S}$  are about 0.8 and 0.78 respectively for case 1. Both  $C_{A,S}$  and  $C_{D,S}$  increases to about 0.82 for case 2 and 0.83 for case 3.

Figure 6.9 shows that the experimental added mass coefficient  $C_A$  converges slowly towards the numerical value for  $C_A$  at  $KC = 0$ . The draft coefficient  $C_D$  is consistently lower than  $C_A$  at a given  $KC$  number.  $C_D$  converges to 0 when  $KC = 0$ , which is to be expected as there is no drag when there is no velocity. All cases have a small spike in  $C_D$  at  $KC = 2$ , which seems to be caused by noise. The difference between  $C_{A,S}$  and  $C_{D,S}$  is more distinct for the large-draft models, than for the small. This may be because the small-draft models are more sensitive to noise than the large ones. The damping increases more for the large-draft models with increasing  $KC$  number than for the small-draft models.

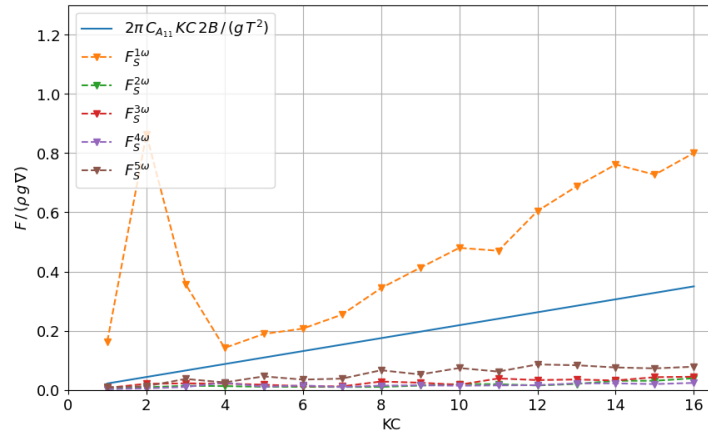
At  $KC = 16$ , it is shown that  $C_{A,S}$  and  $C_{D,S}$  are about 1.1 and 0.91, respectively, for case 1. Both  $C_{A,S}$  and  $C_{D,S}$  increase to about 1.14 and 0.99 for case 2, and to 1.18 and 1.15 for case 3, respectively. The increase in value when increasing distance is more noticeable for the large-draft models. The increase in hydrodynamic forces is to be expected, as discussed in Section 1.2.

If one were to conduct this experiment for  $KC$  numbers above 16, one could expect to see some different trends than for  $KC \leq 16$ . As discussed in Section 1.2, Garbis H. Keulegan and Lloyd H. Carpenter found that the drag coefficient  $C_d$  increased to an unusually high value at low  $KC$  numbers up to 10, and then rapidly decreased before gradually decreasing with increasing  $KC$  number. Considering this finding, it may also be so for the catamaran-shaped floaters. Based on Keulegan and Carpenter one should see that the trend was the same for catamarans, if higher  $KC$  numbers were tested. As this thesis was limited to a maximum  $KC$  of 16, one could suspect that the drag coefficient has not yet reached its peak. This would be interesting to investigate in a separate study.

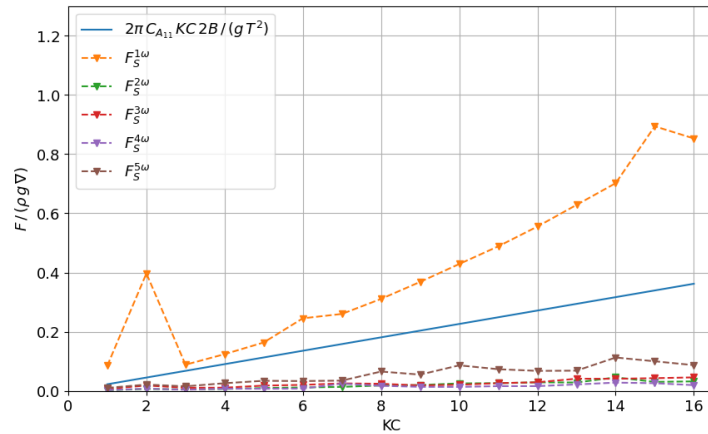


## 6.2.2 Higher $\omega$ -forces

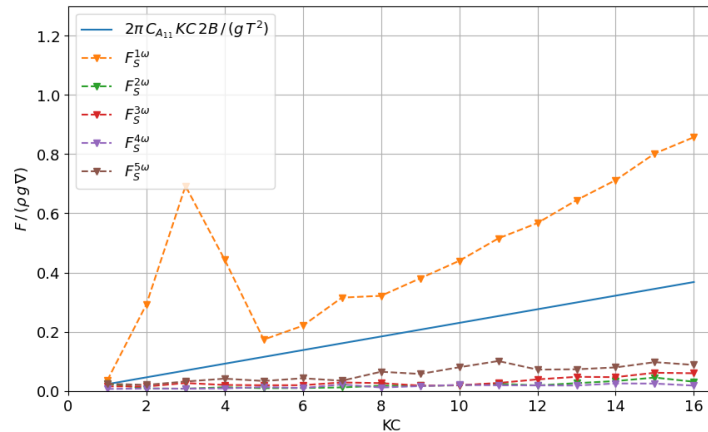
### 6.2.2.1 Small-draft models



(a) Case 1 with small-draft models,  $H/b = 1.5/7.5$



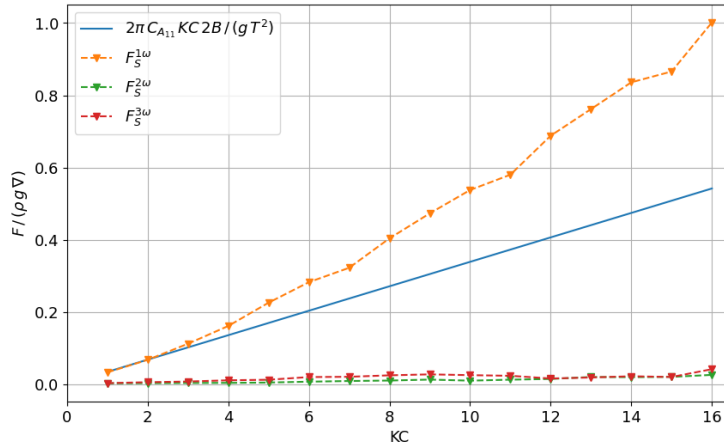
(b) Case 2 with small-draft models,  $H/b = 1.5/11.25$



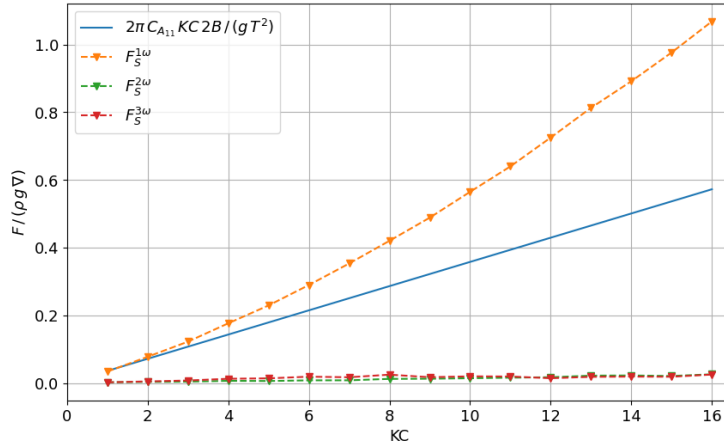
(c) Case 3 with small-draft models,  $H/b = 1.5/15$

Figure 6.10: The force components of the outer and inner module summed is presented. As a comparison, the numerical value from WAMIT is plotted, where  $C_A$  is converted to the linearization for KC numbers in this thesis. This is cases 1, 2, and 3 with the small-draft models.

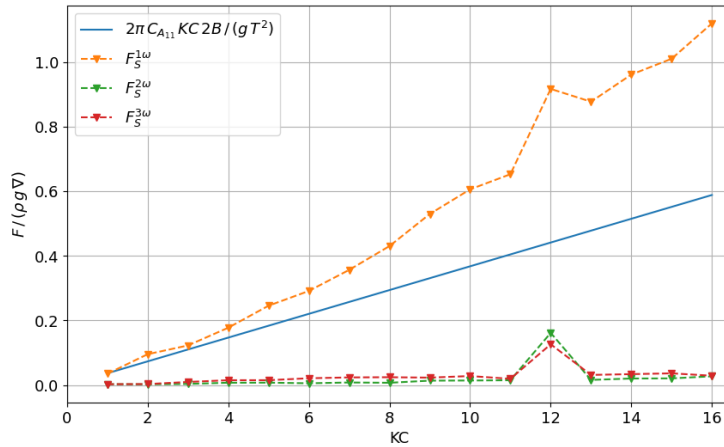
### 6.2.2.2 Large-draft models



(a) Case 1 with large-draft models,  $H/b = 3/7.5$



(b) Case 2 with large-draft models,  $H/b = 3/11.25$



(c) Case 3 with large-draft models,  $H/b = 3/15$

Figure 6.11: The force components of the outer and inner module summed is presented. As a comparison, the numerical value from WAMIT is plotted, where  $C_A$  is converted to the linearization for KC numbers in this thesis. This is cases 1, 2, and 3 with the large-draft models.

---

Figure 6.10 and Figure 6.11 shows the force components  $F_S^\omega$  of the small- and large-draft models, respectively. These are plotted for  $KC \leq 16$ . The added mass coefficient  $C_{A11}$  from numerical analysis in WAMIT is made dimensionless as described in Equation 2.31.

In Figure 6.10, one can see spikes for  $KC < 5$ . The same trend is observed in the analysis of the summed added mass coefficient from the experiment compared in Figure 6.8. These spikes may be due to noise, and should be ignored. When ignoring measurement for the  $F_S^{1\omega}$  for  $KC < 5$ , one can see that the force goes toward zero for  $KC = 0$ . This is to be expected, as there is no hydrodynamic force if there is no velocity.

From the Hammer test in Section 5.1, it was found that the eigenfrequency for the large-draft models included 4-5Hz. This results in the discard of the non-dimensional force of  $4\omega$  and  $5\omega$ , causing  $F_S^{4\omega}$  and  $F_S^{5\omega}$  to be discarded when analyzing the large-draft models. From Figure 6.11 one can see that the  $F_S^{1\omega}$  is dominant for the large-draft models, as for the small-draft models in Figure 6.10.

The maximum  $F_S^{1\omega}$  is at  $KC = 16$ . For the small-draft model, the maximum value is 0.8, 0.85 and 0.86 for cases 1, case 2, and case 3. This is an increase in  $F_S^{1\omega}$  with about 9% from case 1 to case 3. The maximum value of  $F_S^{1\omega}$  with large-draft models are 1.0, 1.07 and 1.13 for case 1, case 2, and case 3. This is an increase of 7% from case 1 to case 2, and 13% from case 1 to case 3.

Figure 6.10 and Figure 6.11 shows that  $F^{1\omega}$  correlates with the numerical value, and diverges at  $KC \geq 4$ . This is expected, as the model is more affected by the vortex shedding for higher  $KC$  numbers. Through the numerical and experimental investigation, there is a trend of the hydrodynamic forces increasing with the increased gap distance. This may be due to the change in wake dynamics when changing the gap distance, as discussed Section 1.2 [12].

P.G. Hals did his thesis on the square- and diamond-shaped cylinders in oscillatory fluid flow. In his thesis, he investigated, amongst other topics, how the hydrodynamic forces were affected by different gap distances between the models. He found that the hydrodynamic forces increased with increased gap distance, and that the damping dominated the added mass for higher  $KC$  values, supporting this finding [27]. As for the experiment studying the square-shaped cylinders, as summarized in Section 3.2.3, there are some correlations in the found trends. As for P. G. Hals [27] and K. Mikkelsen [22], it is found that the hydrodynamic forces increase with increased  $KC$  number, where the  $KC$  numbers range from 1-16 for the catamarans and 1-21 for the square-shaped cylinders. In all cases, the hydrodynamic forces were found to increase with increased gap distance. While the increased draft of the square-shaped cylinders was found to have little effect, the draft increase affected the magnitudes of the hydrodynamic forces for the catamaran shaped-models.

---

## 6.3 Additional notes

In this section, additional notes that highlight important considerations when up-scaling are presented.

### 6.3.1 Full scale

The model is not significantly affected by vortex shedding at small KC numbers, if affected at all. The vortex shedding dominates for large KC numbers, and the added mass and damping increase.

Whether or not the Reynolds number is within the turbulent flow regime can be used to check how accurate the experimental results are for the full-scale structure in turbulent flow. The flow is turbulent if the Reynolds number is within order  $O(10^4)$ . The crossover between laminar and turbulent flow exhibits a gradual transition between the phases, rather than strict demarcations. This leaves some Reynolds numbers to be in-between the phases. One should also note that the separation point of the vortices is fixed at the sharp edges of a box.

The Reynolds number of the models can be calculated by using the relation in Equation 2.5

$$\text{Re} = \frac{U_{max}B}{\nu} = \frac{\omega AB}{\nu} = \frac{KC \omega B B}{2\pi \nu} = \frac{KCB^2}{2\pi \nu T}. \quad (6.2)$$

Using  $\nu = 10^{-6}$ ,  $T = 1$  s,  $B = 0.075$  m and  $KC = 1, 4, 10$  and  $16$ , gives us model scale value

$$\begin{aligned} \text{Re} &= \frac{1 \cdot 0.075^2}{2\pi \cdot 10^{-6} \cdot 1} = 89.5, \\ \text{Re} &= \frac{4 \cdot 0.075^2}{2\pi \cdot 10^{-6} \cdot 1} = 358 \\ \text{Re} &= \frac{10 \cdot 0.075^2}{2\pi \cdot 10^{-6} \cdot 1} = 895, \\ \text{Re} &= \frac{16 \cdot 0.075^2}{2\pi \cdot 10^{-6} \cdot 1} = 1432. \end{aligned} \quad (6.3)$$

Scaling to the full-scale structure by using scaling factor  $\lambda = 10$ . The full-scale Reynolds numbers are found as

$$\begin{aligned} \text{Re} &= 89.5 \cdot 10^{1.5} = 0.28 \cdot 10^4, \\ \text{Re} &= 358 \cdot 10^{1.5} = 1.1 \cdot 10^4, \\ \text{Re} &= 895 \cdot 10^{1.5} = 2.8 \cdot 10^4, \\ \text{Re} &= 1432 \cdot 10^{1.5} = 4.5 \cdot 10^4. \end{aligned} \quad (6.4)$$

For KC numbers  $\leq 4$ , the Reynolds number is too low for the free shear layers due to separated flow, to be characterized as fully turbulent characteristics. However, the

---

viscous effects are negligible in this KC range, and hold limited practical interest. KC numbers  $< 10$  correspond to Reynolds numbers on the order of  $10^4$ , indicating well-developed turbulent free shear layers. Consequently, results obtained for these KC numbers are likely representative of full-scale conditions.

In the KC number range between 4 and 10, the Reynolds numbers do not reach sufficiently high values to make the same assertion, but these KC numbers may still be relevant for practical applications. It would be interesting to conduct a separate study to investigate larger models.

This analysis of the Reynolds number indicates that  $KC \geq 4$  is a good indication that the experimental results are somewhat accurate for the full-scale model. The full-scale structure  $KC \leq 3$  is within the border area between the laminar and turbulent flow. It seems that the experimental values for  $\leq 3$  are not as valid for the full-scale structure, and one could use the numerical estimated values instead.

# Chapter 7

## Conclusion and further work

The numerical and experimental studies presented focus on investigating hydrodynamic loads affecting catamaran-shaped floaters. In this section, key findings and conclusions are drawn from the study.

### 7.1 Conclusions

The comprehensive numerical and experimental conducted in this study provided strong results showing the hydrodynamic interaction between the catamaran-shaped floaters. Specifically, the investigation explored the effect of two factors: the increased gap distance between the catamaran models and the increased draft.

The numerical estimated added mass coefficients  $C_A$  for long-crested waves, analyzed in WAMIT, were found to be satisfying when compared to the standards of DNV-RP-C205. In the analysis of the hydrodynamic forces acting on the catamaran models, the short-crested waves showed indications of being affected by sloshing.

Furthermore, an interesting finding was that the added mass coefficients  $C_A$  converged towards the numerical estimated value in surge as the KC number approached  $KC = 0$ . At this point, when  $KC = 0$ , the drag coefficient  $C_D$  was found to approach zero. These findings supported the validity and accuracy of both the experiment and numerical investigation.

Another noteworthy discovery was that the hydrodynamic forces  $C_A$ ,  $C_B$ ,  $C_D$ ,  $F_{exc}$ , and  $F^\omega$  increased with increasing KC number within the range  $KC = [0, 16]$ . This was found to be due to models experiencing the effect of vortex shedding for increasing KC numbers. Additionally, it was observed that higher harmonic components were relatively small compared to  $F_S^{1\omega}$ . The hydrodynamic forces in surge increased with increasing gap distance in the range  $b = [7.5, 11.25, 15]$ , as investigated in case 1, case 2, and case 3. This was to be expected since the wake dynamics changed with varying gap distances between bodies.

For higher KC numbers, it was found that the experimental hydrodynamic forces

---

increased at a faster rate than the numerical values. This difference could be expected due to the physical differences in real fluid and perfect fluid used in the experimental and numerical investigation, respectively.

## 7.2 Further work

While working on the master's thesis, several intriguing subjects seem promising for further investigation. In this section, some interesting avenues are outlined. These can help expand the understanding of the hydrodynamic loads of catamarans:

- Redo this study with larger models. By increasing the model by a factor of two, the Reynolds number increases by a factor of 3. This would result in well-turbulent free shear layers for  $KC$  in the range of 1 to 16. While it would require a slightly larger rig and basin, it would provide an advantage by reducing experimental uncertainties. One problem with increasing the plates and models, is that the mass increases, and the eigenfrequency moves towards lower frequencies. One solution to this is to reduce the weight. This could be accomplished to some extent by crafting the models of a different material.
- It would be enlightening to conduct a numerical and experimental study regarding higher  $KC$  numbers, using CFD as well. Increasing the range of  $KC$  numbers, can be done by increasing the size of the rig and basin.
- To build upon the scope of this master, it would be interesting to conduct a CFD study of the cases studied in this thesis.
- Conduct a numerical and experimental investigation regarding catamaran-shaped floaters in a staggered arrangement. It would be interesting to compare the catamarans in a staggered arrangement to the findings of Zdravkovich [5] and co-student Kristian Mikkelsen [22].
- Conduct a model experiment investigating the motion of a floating solar island in waves for tandem flow and staggered arrangements. This could be done by investigating the solar panels connected as a train formation or a 2x4 formation. Studying the hydrodynamic forces, excitation forces, and phenomena such as sloshing would be interesting.

# Bibliography

- [1] GASSCO. The green shift.
- [2] Magnus Onsrud. An experimental study on the wave-induced vertical response of an articulated multi-module floating solar island. Master's thesis, NTNU, 2019.
- [3] Torunn Kjeldstad, Dag Lindholm, Erik Marstein, and Josefine Selj. Cooling of floating photovoltaics and the importance of water temperature. *Solar Energy*, 218:544–551, 2021.
- [4] Evgeny Solomin, Evgeny Sirotkin, Erdem Cuce, Shanmuga Priya Selvanathan, and Sudhakar Kumarasamy. Hybrid floating solar plant designs: a review. *Energies*, 14(10):2751, 2021.
- [5] MM Zdravkovich. Review of flow interference between two circular cylinders in various arrangements. 1977.
- [6] JR Pannell, EA Griffiths, and JD Coales. Experiments on the interference between pairs of aeroplane wires of circular and lenticular cross section. *Reports and Memoranda—Aeronautical Research Council (Great Britain), Report*, 208, 1915.
- [7] David Biermann and William H Herrnstein Jr. The interference between struts in various combinations. Technical report, 1934.
- [8] Ei-ichi Hori. Experiments on flow around a pair of parallel circular cylinders. In *Proc. 9th Japan National Congress for Applied Mech.*, pages 231–234, 1959.
- [9] Garbis H Keulegan, Lloyd H Carpenter, et al. Forces on cylinders and plates in an oscillating fluid. *Journal of research of the National Bureau of Standards*, 60(5):423–440, 1958.
- [10] JMR Graham. The forces on sharp-edged cylinders in oscillatory flow at low keulegan-carpenter numbers. *Journal of Fluid Mechanics*, 97(2):331–346, 1980.
- [11] PW Bearman, MJ Downie, JMR Graham, and ED Obasaju. Forces on cylinders in viscous oscillatory flow at low keulegan-carpenter numbers. *Journal of fluid mechanics*, 154:337–356, 1985.
- [12] B Havel, H Hangan, and R Martinuzzi. Buffeting for 2d and 3d sharp-edged bluff bodies. *Journal of Wind Engineering and Industrial Aerodynamics*, 89(14-15):1369–1381, 2001.



- 
- [13] E.E.Bachynski-Polic T.Kristiansen and D.Myrhaug. *Compendium TMR4182 - Marine Dynamics*. Department of Marine Technology, NTNU, 2022.
- [14] Fredrik Mentzoni and Trygve Kristiansen. Numerical modeling of perforated plates in oscillating flow. *Applied Ocean Research*, 84:1–11, 2019.
- [15] Henrik Reiten. Two-dimensional numerical and experimental investigation of hydrodynamic forces and wake interaction between two or more square cylinders in large-amplitude oscillatory flow. Master’s thesis, NTNU, 2022.
- [16] Nikolaus Rott. Note on the history of the reynolds number. *Annual review of fluid mechanics*, 22(1):1–12, 1990.
- [17] Fredrik Mentzoni, Mia Abrahamsen-Prsic, and Trygve Kristiansen. Hydrodynamic coefficients of simplified subsea structures. In *International Conference on Offshore Mechanics and Arctic Engineering*, volume 51203, page V001T01A034. American Society of Mechanical Engineers, 2018.
- [18] O.M. Faltinsen. *Seal loads on ship and offshore structures*. Cambridge, 1990.
- [19] Alexander N.Timokha Odd M.Faltinsen. *Sloshing*. 2009.
- [20] B Molin, F Remy, O Kimmoun, and Y Stassen. Experimental study of the wave propagation and decay in a channel through a rigid ice-sheet. *Applied ocean research*, 24(5):247–260, 2002.
- [21] Bernard Molin. On the piston and sloshing modes in moonpools. *Journal of Fluid Mechanics*, 430:27–50, 2001.
- [22] Kristian Mikkelsen. Three-dimensional experimental investigation of hydrodynamic forces and wake interaction between two or more cylinders in large-amplitude oscillatory flow. Master’s thesis, NTNU, 2023.
- [23] Jason Mais. Spectrum analysis - the key features of analyzing spectra. Accessed: 04-20-2023.
- [24] WAMIT. Wamit theory manual. Accessed: 05-02-2023.
- [25] WAMIT. Wamit user manual. Accessed: 05-02-2023.
- [26] Det Norske Veritas. Dnv-rp-c205 environmental conditions and environmental loads. *Det Norske Veritas: Oslo, Norway*, 2010.
- [27] Petter Grudt Hals. Numerical experimental studies on the hydrodynamic loads on square-shaped and diamond-shaped cylinders in close proximity exposed to a forced oscillatory fluid flow. Master’s thesis, NTNU, 2023.
- [28] U. Ghia, K. N. Ghia, and C. T. Shin. High-re solutions for incompressible flow using the navier-stokes equations and a multigrid method. *Journal of Computational Physics*, 48:387–411, 1982.
- [29] GlobleNewsWire. Global floating solar panel market report 2022: Investments in floating solar panels continue to grow.

- 
- [30] Liang Sun, R Eatock Taylor, and Yoo Sang Choo. Responses of interconnected floating bodies. *The IES Journal Part A: Civil & Structural Engineering*, 4(3):143–156, 2011.

# Appendix A

## Literature review

### A.1 Pannell, Griffiths and Coales circular wire experiment

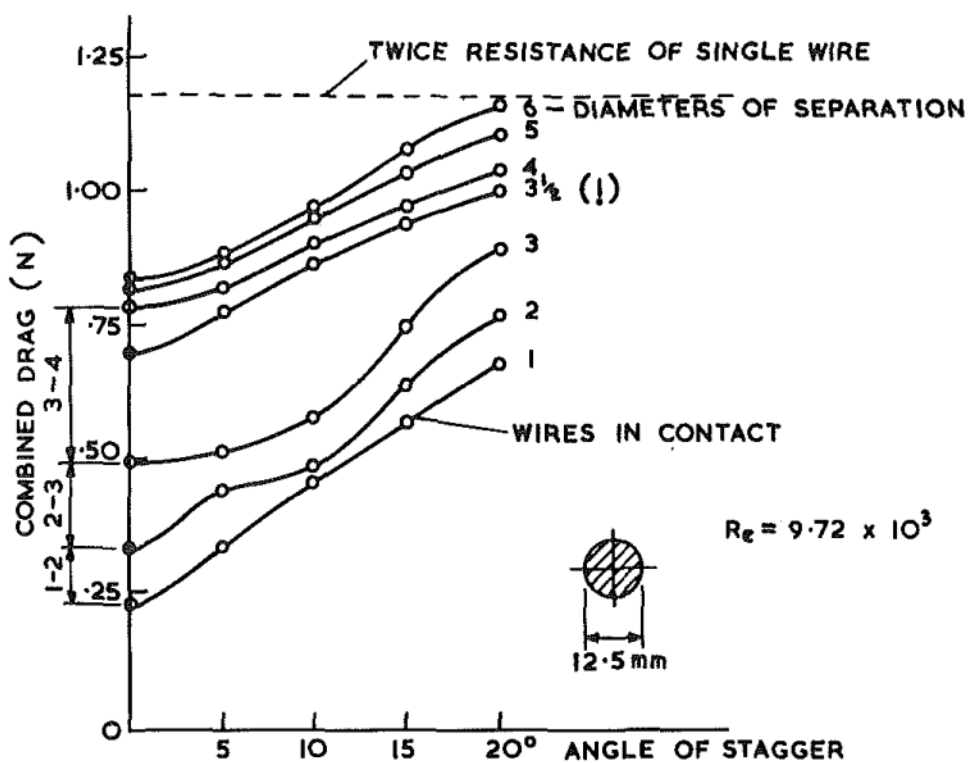


Fig. 1 Combined drag of two wires [1]

Figure A.1: The results from Pannell, Griffiths and Coales's experiment regarding combined drag for two wires. The distance between the wires increased from starting point where the wires was in contact. The starting Reynolds number was  $9.72 \cdot 10^3$  [6].

## A.2 Biermann and Herrnstein wind tunnel experiment

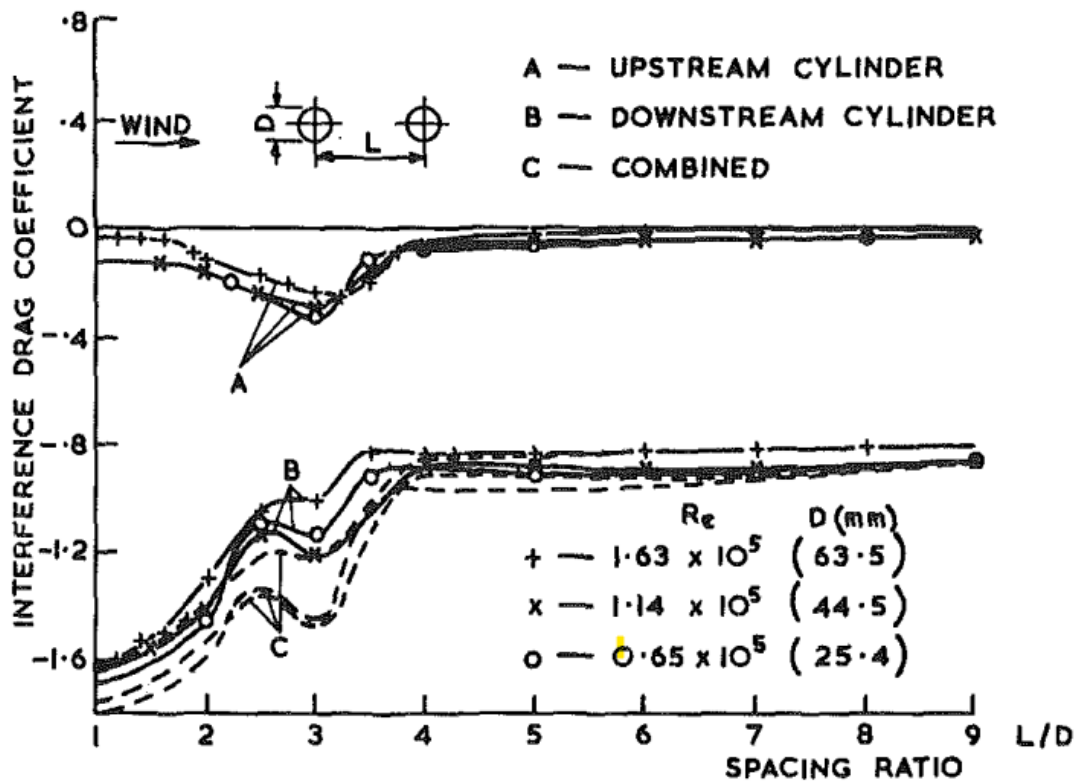


Figure A.2: The results from Biermann and Herrnstein's experiment regarding drag interference of two cylinders in an wind tunnel combined drag for two wires [7].

---

### A.3 Hori's experiment on the pressure disturbance around two cylinders

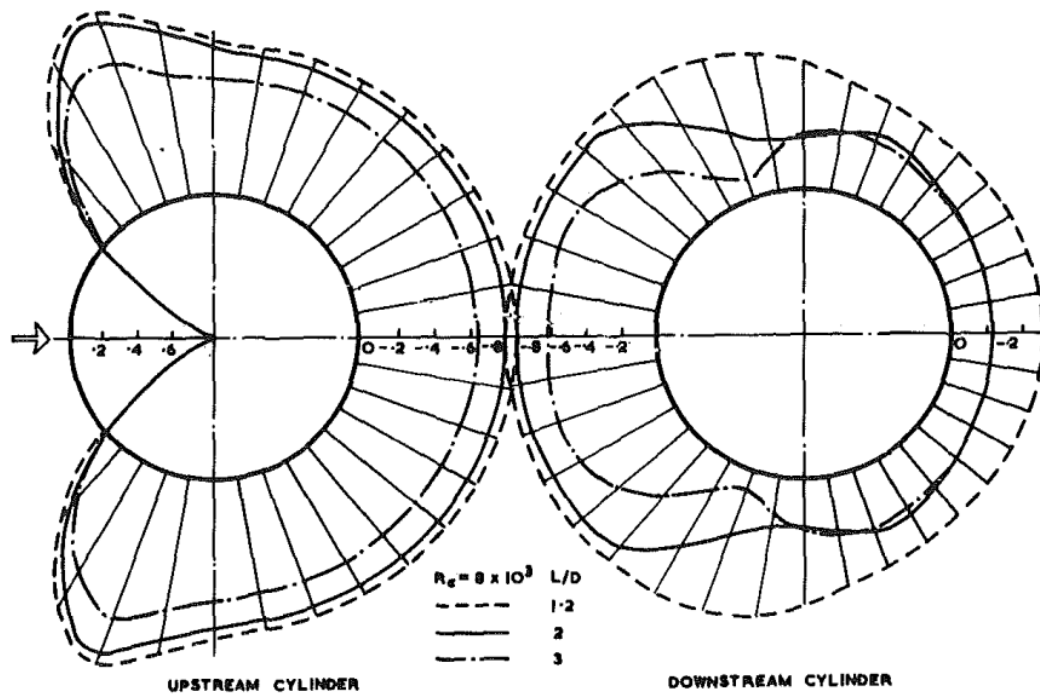


Figure A.3: The results from Hori's experiment result from drag interference of two cylinders in an wind tunnel in polar coordinates [8].

---

A.4 Garbis H. Keulegan and Lloyd H. Carpenter's figure for drag coefficient from their experimental and numerical study of *forces on cylinders and plated in an oscillating fluid*

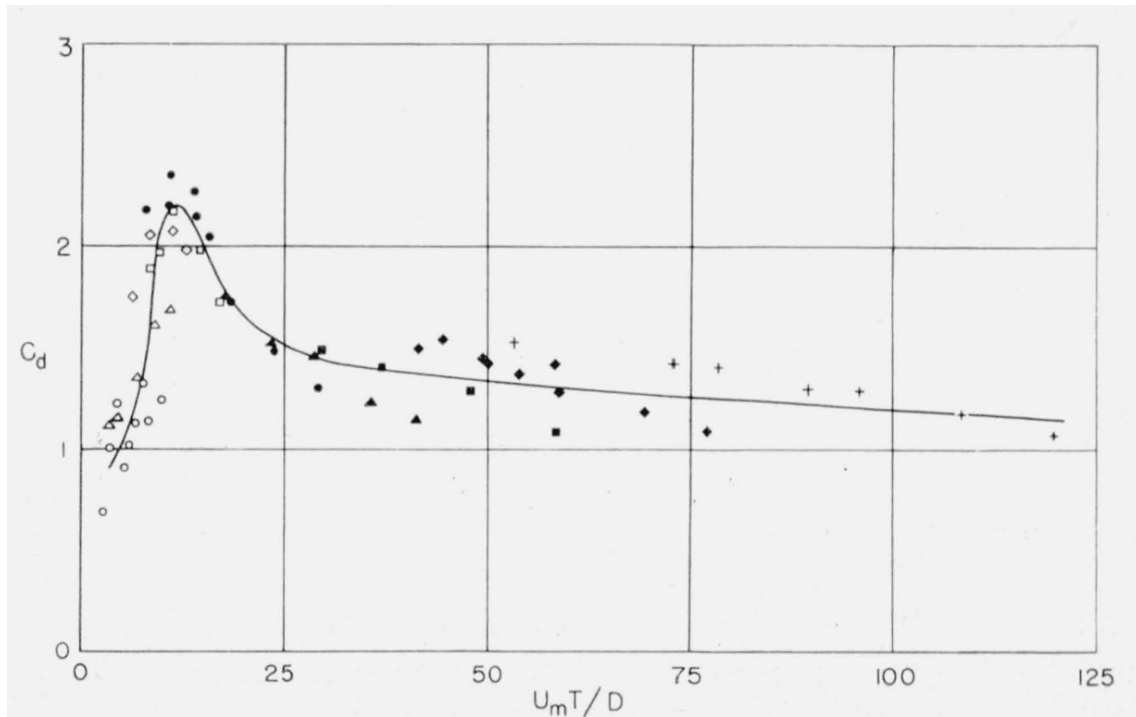


Figure A.4: The variation of drag coefficient of cylinders investigated by Garbis H. Keulegan and Lloyd H. Carpenter in 1958 [9].

---

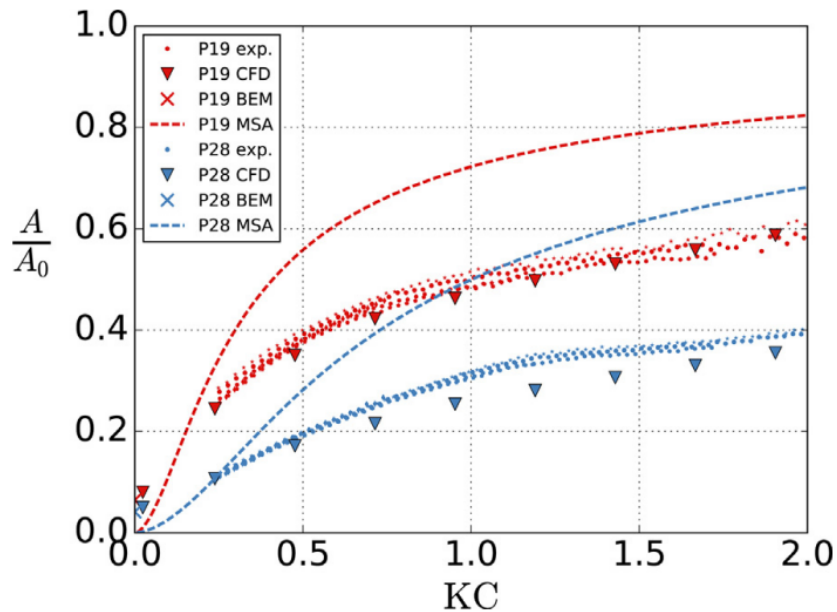
## A.5 Onsrud's Master thesis model



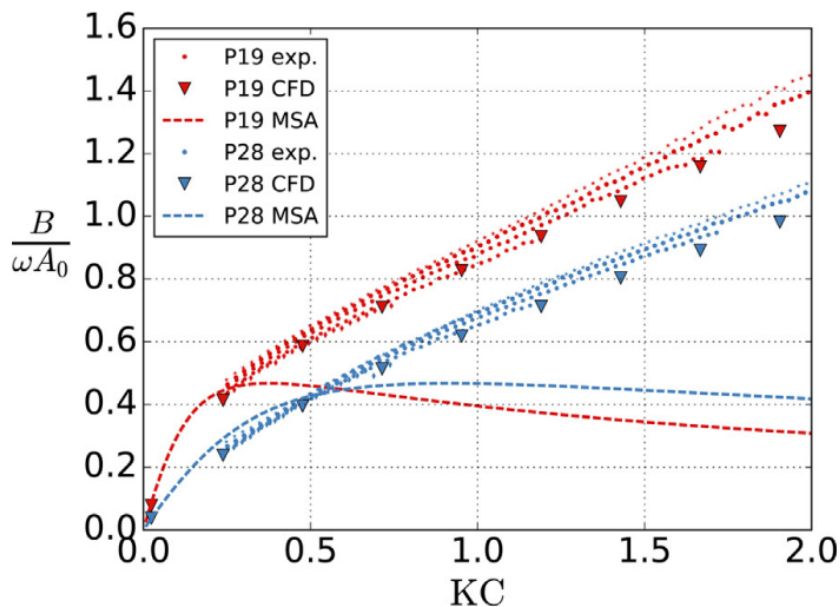
Figure A.5: The model used in Onsrud's Master Thesis. This was an simplified model of the Moss Maritime concept [2], and the scale was 1:20.

---

## A.6 Fredrik Mentzoni's added mass and damping coefficients from his paper: *numerical modeling of perforated plates in oscillating flow*



(a) The added mass coefficients from CFD simulations presented over five periods.



(b) The damping coefficients from CFD simulations presented over five periods.

Figure A.6: The added mass coefficient  $A/A_0$  and damping coefficient  $B/(\omega A_0)$  from CFD simulations for five periods [14].



# Appendix B

## The calculation of exciting forces of a submerged body

### B.1 Foude Krylov force

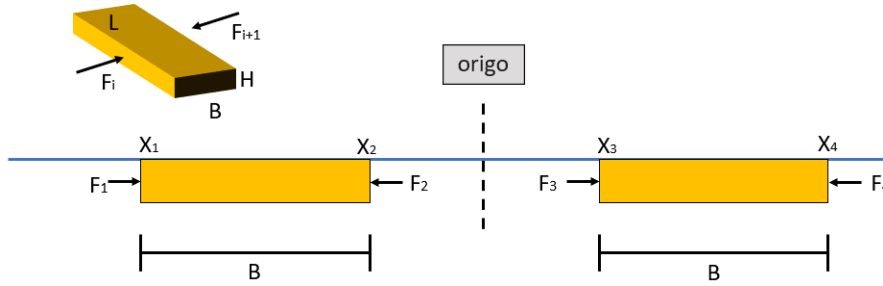


Figure B.1: Forces integrated over the sides of an catamaran pair.

We start by analysing a submerged catamaran floater pair, as shown in Figure B.1. The distance is equal from catamarans to origo, for both catamarans. The total distance between the floaters are  $\mathbf{B}$ .  $x_1 = -x_4$  and  $x_2 = -x_3$  The force acting on the side of the model can be calculated as

$$F = \int_S \rho A \vec{n} dS.$$

The sum of forces of one catamaran model is

$$F = \sum_{i=1}^4 F_i \vec{n} = F_1 - F_2 + F_3 - F_4$$

The dynamic pressure is specified in WAMIT [25] as

$$P_D = \rho g \zeta_a e^{kz} \cos(\omega t - kx).$$

---

Integrating over height, from waterline to submergence -H for  $F_i$

$$F_i = \int_{-H}^0 L\rho g\zeta_A e^{kz} \cos(\omega t - kx_i) dx dz = L\rho g\zeta_A \cos(\omega t - kx_i) \int_{-H}^0 e^{kz} dz$$

$$F_i = \frac{L\rho g\zeta_A}{k} (1 - e^{kH}) \cos(\omega t - kx_i)$$

$$F_i = F_0 \cos(\omega t - kx_i)$$

The sum of forces of one catamaran model can now be expressed as

$$F_{FK} = F_0 \cos(\omega t - kx_1) - F_0 \cos(\omega t - kx_2) + F_0 \cos(\omega t - kx_3) - F_0 \cos(\omega t - kx_4)$$

We move the  $F_0$  term to the left hand side, and set  $X_1 = -X_3$  and  $x_2 = -x_4$ . We now have

$$\frac{F_i}{F_{FK}} = \cos(\omega t + kx_4) - \cos(\omega t + kx_3) + \cos(\omega t - kx_3) - \cos(\omega t - kx_4)$$

$$\frac{F_i}{F_{FK}} = \cos(\omega t - kx_3) - \cos(\omega t + kx_3) + \cos(\omega t + kx_4) - \cos(\omega t - kx_4)$$

Using

$$2 \cos A \cos B = \cos(A + B) + \cos(A - B)$$

$$2 \sin A \sin B = \cos(A - B) - \cos(A + B)$$

We can now express  $F_{FK}/F_0$  as

$$\frac{F_i}{F_{FK}} = 2 \sin(\omega t) \sin(kx_3) - 2 \sin(\omega t) \sin(kx_3)$$

Using the relation  $x_4 = x_3 + B$ , and we get

$$\frac{F_i}{F_{FK}} = 2 \sin(\omega t) \left[ \sin(kx_3) - \sin(kx_3 + kB) \right]$$

## B.2 Diffraction force

The diffraction force can be found from the relation

$$F_{exc} = F_{FK} + F_{diff}$$

$$F_{diff} = F_{exc} - F_{FK}$$

The total excitation  $F_{exc}$  is on complex form, so we need to convert this to complex form. Using rule  $z = r \cos \Phi + ir \sin \Phi$

$$F_{diff} = r e^{i\varphi} - F_{FK} e^{i\varphi_{FK}}$$

$$F_{diff} = r \cos \varphi_{exc} + ir \sin \varphi_{exc} - F_{FK} \cos \varphi_{exc} - iF_{FK} \sin \varphi_{FK}$$

$$F_{diff} = \sqrt{(\Re)^2 + (\Im)^2}$$

$$F_{diff} = \sqrt{\left( r \cos(\varphi_{exc}) - F_{FK} \cos(\varphi_{FK}) \right)^2 + \left( r \sin(\varphi_{exc}) - F_{FK} \sin(\varphi_{FK}) \right)^2}$$

---

and

$$\phi = \arctan\left(\sqrt{\frac{\Re}{\Im}}\right)$$
$$\phi = \arctan\left(\sqrt{\frac{r \cos(\phi_{exc}) - F_{FK} \cos(\phi_{FK})}{r \cdot \sin(\phi_{exc}) - F_{FK} \cdot \sin(\phi_{FK})}}\right)$$

where

$$\Im(ir \sin(\phi_e) - iF_{FK} \sin(\phi_{FK})) = r \sin(\phi_e) - F_{FK} \sin(\phi_{FK})$$

# Appendix C

## A visualization of grids used in WAMIT

### C.1 Grid refinement G2, large-draft model

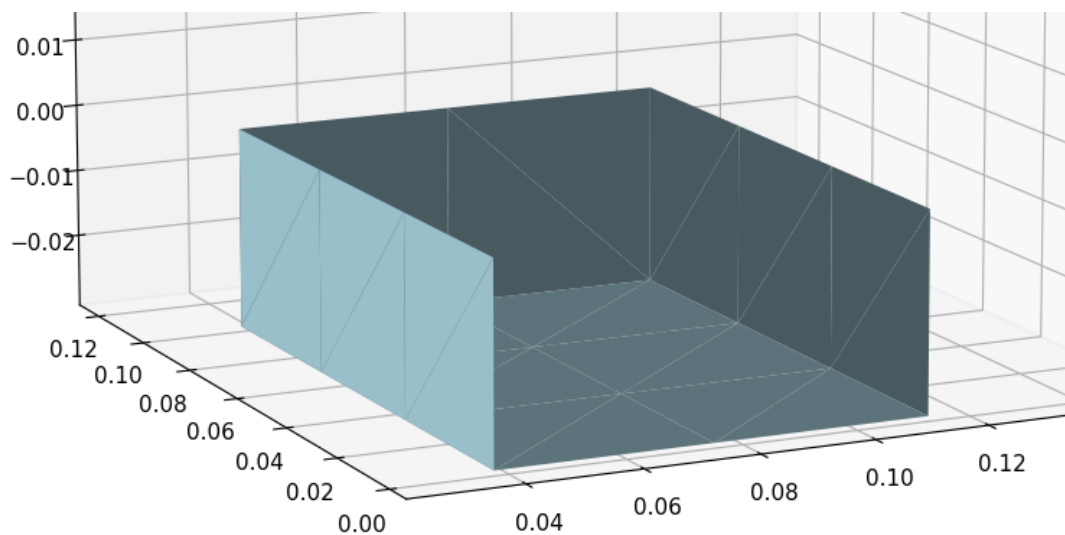


Figure C.1: A visualization of the WAMIT grid input before mirroring about the x- and y-axis. Course grid, 1 panel per cm. Large-draft model with length x breadth x height = 20cm x 7.5cm x 3cm after mirroring

---

## C.2 Grid refinement G4, large-draft model

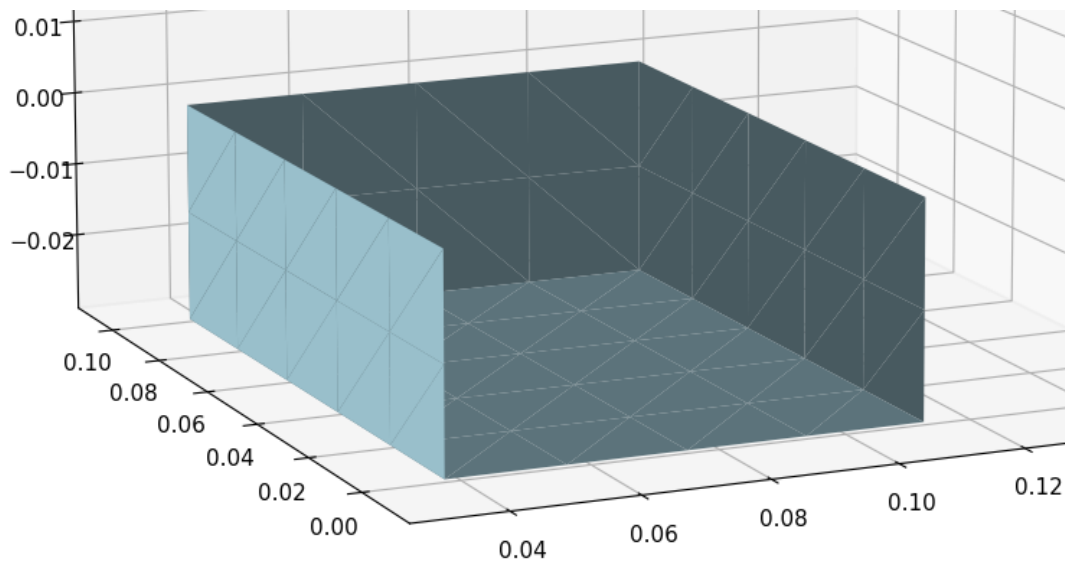


Figure C.2: A visualization of the WAMIT grid input before mirroring about the x- and y-axis. Course grid, 2 panel per cm. Large-draft model with length x breadth x height = 20cm x 7.5cm x 3cm after mirroring

## C.3 Grid refinement G8, large-draft model

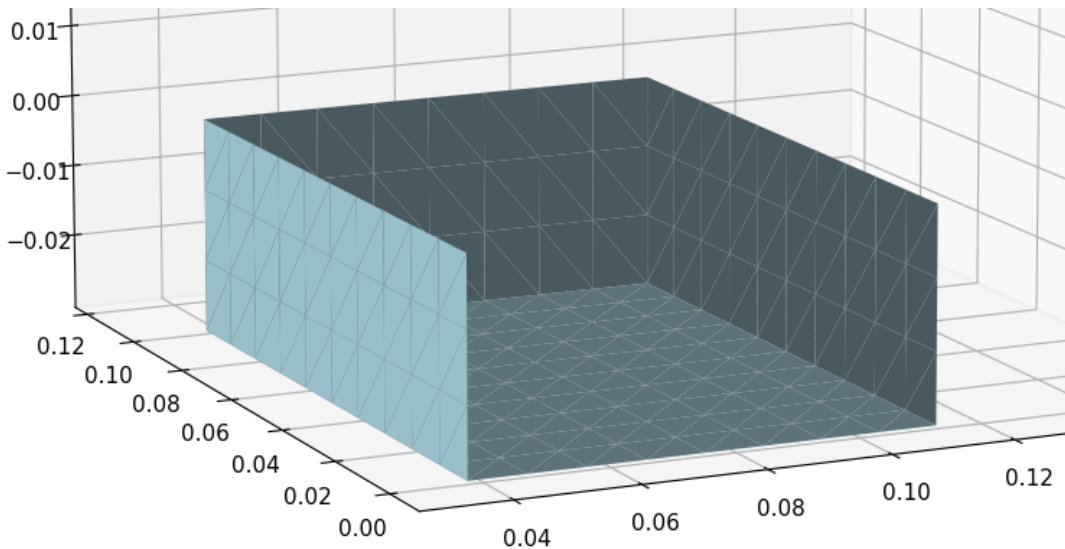


Figure C.3: A visualization of the WAMIT grid input before mirroring about the x- and y-axis. Course grid, 3 panel per cm. Large-draft model with length x breadth x height = 20cm x 7.5cm x 3cm after mirroring

---

## C.4 Grid refinement G15, large-draft model

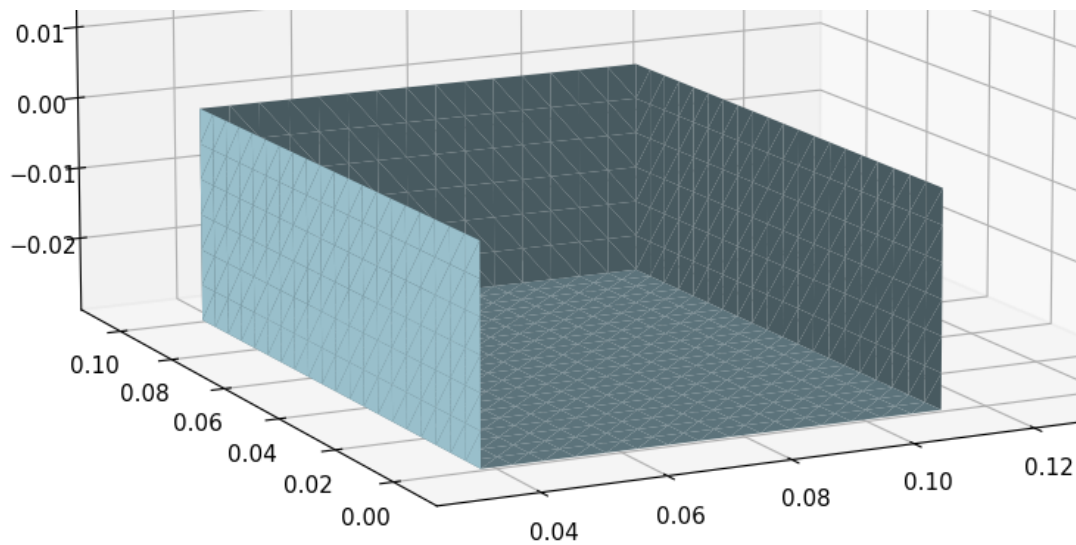


Figure C.4: A visualization of the WAMIT grid input before mirroring about the x- and y-axis. Course grid, 6 panel per cm. Large-draft model with length x breadth x height = 20cm x 7.5cm x 3cm after mirroring

## C.5 Grid refinement G22, large-draft model

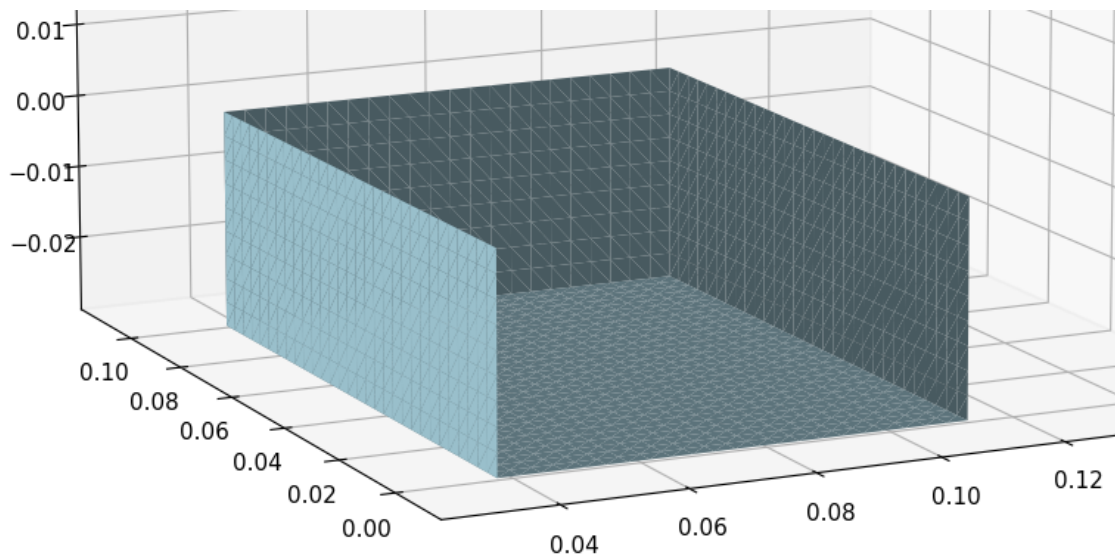
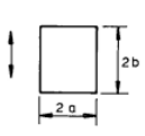


Figure C.5: A visualization of the WAMIT grid input before mirroring about the x- and y-axis. Course grid, 9 panel per cm. Large-draft model with length x breadth x height = 20cm x 7.5cm x 3cm after mirroring

# Appendix D

## Using DNV-RP-C205 to calculating added mass coefficient

Estimating the analytical added mass coefficient,  $C_{A,DNV}$ , for two-dimensional bodies by using DNV-RP-C205 appendix D for rectangle plates, which is shown in Figure D.1. Applying strip theory to one of the floaters makes it possible to use this approach. The strip of the floater that is used, is shown in Figure D.2. After estimating the  $C_{A,2D}$ , one can estimate the  $C_{A,3D}$  by correcting for the 3-dimensional effects. This correction can be done by using DNV-RP-C205 appendix D for right circular cylinder.

| <b>Table D-1 Analytical added mass coefficient for two-dimensional bodies, i.e. long cylinders in infinite fluid (far from boundaries).</b> |  |                     |   |           |   |           |           |
|---|--|---------------------|---|-----------|---|-----------|-----------|
| <b>Added mass (per unit length) is <math>m_A = \rho C_A A_R</math> [kg/m] where <math>A_R</math> [m<sup>2</sup>] is the reference area.</b> |  |                     |   |           |   |           |           |
| Section through body  |  | Direction of motion | $C_A$   | $A_R$     | Added mass moment of inertia [(kg/m) × m <sup>2</sup> ] |           |           |
|    |  | Vertical            | 1.0<br>1.14<br>1.21<br>1.36<br>1.51<br>1.70<br>1.98<br>2.23 | $\pi a^2$ | $\beta_1 \rho \pi a^4$ or $\beta_2 \rho \pi b^4$        |           |           |
|   |  |                     |   |           | $a/b$   | $\beta_1$ | $\beta_2$ |
|   |  |                     |   |           | 0.1   | -         | 0.147     |
|   |  |                     |   |           | 0.2   | -         | 0.15      |
|   |  |                     |   |           | 0.5   | -         | 0.15      |
|   |  |                     |   |           | 1.0   | 0.234     | 0.234     |
|   |  |                     |   |           | 2.0   | 0.15      | -         |
|   |  |                     |   |           | 5.0   | 0.15      | -         |
|   |  |                     |   |           | $\infty$  | 0.125     | -         |

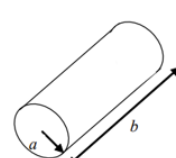
| <b>Table D-2 Analytical added mass coefficient for three-dimensional bodies in infinite fluid (far from boundaries).</b>          |          |                     |        |       |             |
|---|----------|---------------------|--------|-------|-------------|
| <b>Added mass is <math>m_A = \rho C_A V_R</math> [kg] where <math>V_R</math> [m<sup>3</sup>] is reference volume. (Continued)</b> |          |                     |        |       |             |
| Body shape  |          | Direction of motion | $C_A$  |       | $V_R$       |
|    |          | Vertical            | $b/2a$ | $C_A$ | $\pi a^2 b$ |
|   |          |                     |        | 1.2   |             |
|   | 2.5      | 0.78                |        |       |             |
|   | 5.0      | 0.90                |        |       |             |
|   | 9.0      | 0.96                |        |       |             |
|   | $\infty$ | 1.00                |        |       |             |

Figure D.1: Table of analytical added mass coefficient for two-dimensional plate found in DNV-RP-C205 appendix D [26]

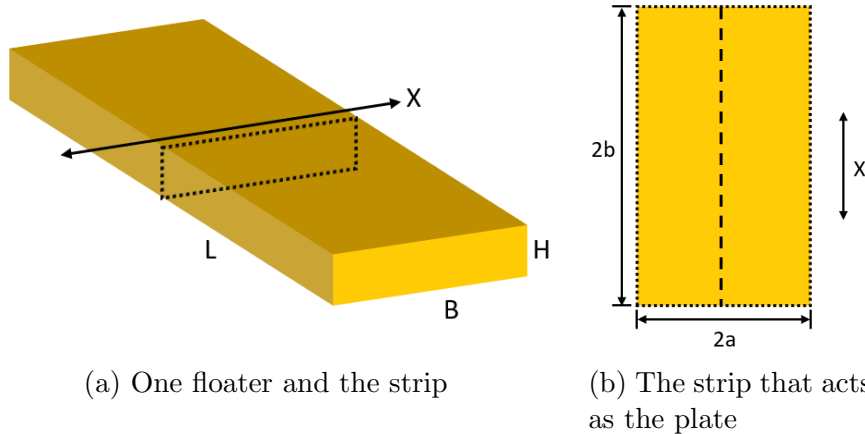


Figure D.2: One floater and the strip used for estimating DNV-RP-C205's analytical added mass coefficient

## D.1 Calculation procedure

The procedure for calculating the analytical added  $C_{A,DNV}$ , starts by mirroring the draft  $H$  about the free surface. The total mirrored draft is  $2H$ . The short, mirrored side of the plate is divided by the long side, resulting in the relation shown in Equation D.1. The relation produces a value that is interpolated and used to obtain  $C_{A,DNV}$ . Next is to correct for the normalization used by DNV, and apply a normalization that is consistent:  $\rho\pi ab$ .

### Small

$$\frac{2a}{2b} = \frac{2 \cdot 0.015}{0.075} = 0.4. \quad (D.1)$$

Interpolating

$$C_{A,DNV} = 1.98 + \frac{1.70 - 1.98}{0.5 - 0.2}(0.4 - 0.2) = 1.793. \quad (D.2)$$

Converting to our way of normalization

$$\begin{aligned} F_{DNV} &= C_{A,DNV} \cdot \rho\pi a^2 = C_{A,DNV} \cdot \rho\pi(a \cdot b) \frac{a}{b} = (C_{A,DNV} \frac{a}{b}) \cdot (\rho\pi a \cdot b) \\ C_{A,2D} &= C_{A,DNV} \cdot \frac{a}{b} = 1.793 \cdot 0.4 = 0.717 \end{aligned} \quad (D.3)$$

### Large

$$\frac{2a}{2b} = \frac{2 \cdot 0.03}{0.075} = 0.8. \quad (D.4)$$



---

Interpolating

$$C_{A,DNV} = 1.70 + \frac{1.51 - 1.70}{1 - 0.5}(0.8 - 0.5) = 1.586. \quad (\text{D.5})$$

Converting to our way of normalization

$$\begin{aligned} F_{DNV} &= C_{A,DNV} \cdot \rho \pi a^2 = C_{A,DNV} \cdot \rho \pi (a \cdot b) \frac{a}{b} = \left( C_{A,DNV} \frac{a}{b} \right) \cdot (\rho \pi a \cdot b) \\ C_{A,2D} &= C_{A,DNV} \cdot \frac{a}{b} = 1.586 \cdot 0.8 = 1.269 \end{aligned} \quad (\text{D.6})$$

## D.2 Correcting for 3-dimensional effects

**Small**

$$C_{A,DNV,3D} = \frac{b}{2a} = \frac{0.075}{2 \cdot 0.015} = 2.5 \Rightarrow Ca = 0.78 \quad (\text{D.7})$$

Correcting for 3D-effects

$$C_{A,3D} = C_{A,2D} \cdot C_{A,DNV,3D} = 0.717 \cdot 0.78 = 0.559 \quad (\text{D.8})$$

**Large**

$$C_{A,DNV,3D} = \frac{b}{2a} = \frac{0.075}{2 \cdot 0.03} = 1.25 \quad (\text{D.9})$$

Interpolating

$$C_{A,DNV} = 0.78 + \frac{0.62 - 0.78}{1.2 - 2.5}(1.25 - 2.5) = 0.626. \quad (\text{D.10})$$

Correcting for 3D-effects

$$C_{A,3D} = C_{A,2D} \cdot C_{A,DNV,3D} = 1.269 \cdot 0.626 = 0.794 \quad (\text{D.11})$$

## D.3 Summary

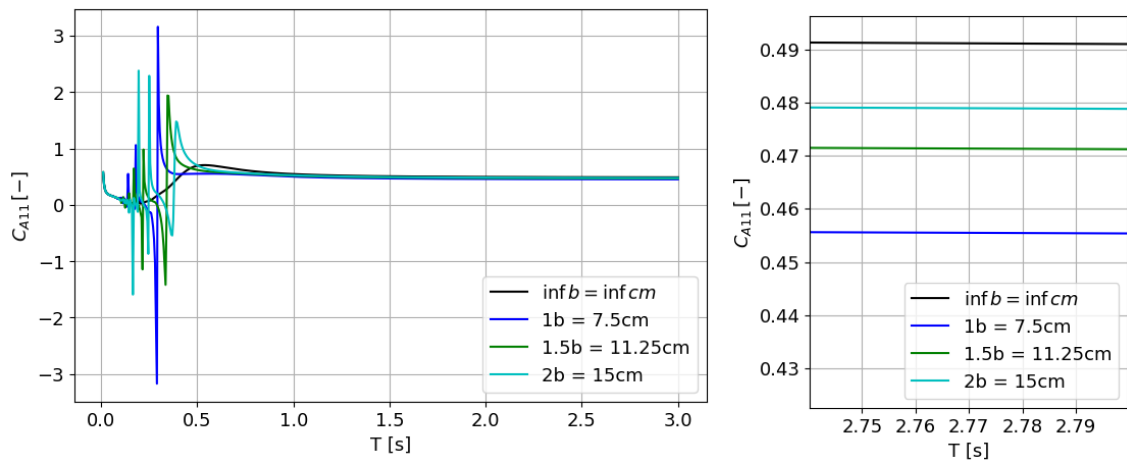
From the experiments it is expected that the estimation of the added mass coefficient should be somewhat larger than the values obtained from WAMIT. The added mass coefficients from WAMIT are found to be around 0.45-0.5 for the small-draft model and 0.7-0.8 for the large-draft model. The DNV estimation is somewhat over-predicting in general, so this verifies the numerical estimations to some extent.

# Appendix E

## Added mass coefficients in 6 Degrees Of Freedom (DOF)

### E.1 Small-draft models

#### E.1.1 The added mass coefficients in surge, $C_{A11}$

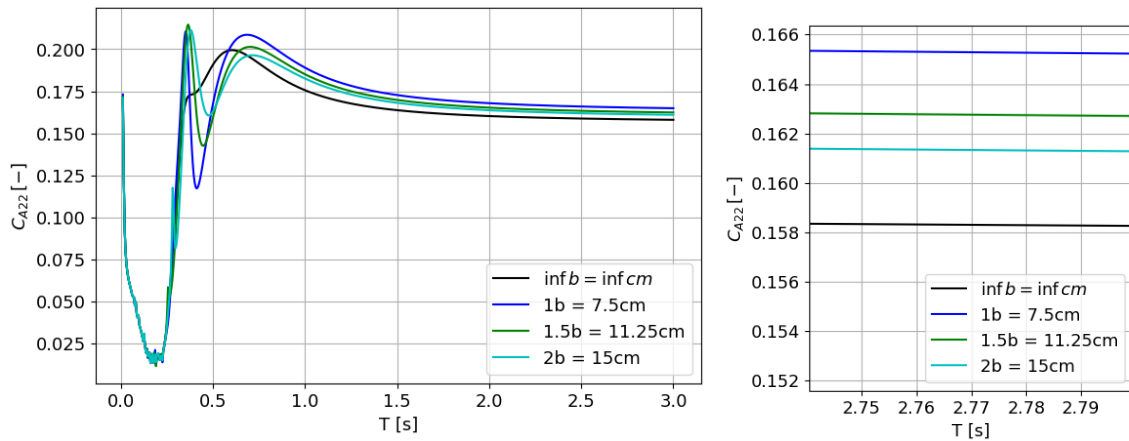


(a) The added mass coefficient  $C_{A11}$  plotted for period  $T \leq 3$  seconds.

(b) The added mass coefficient  $C_{A11}$  plotted for long crested waves and close to convergence.

Figure E.1: The added mass coefficient in surge  $C_{A11}$  for the small-draft models analysed in WAMIT.  $C_{A11}$  is plotted with three gap distance configurations, in addition to the infinite gap distance that is denoted 'inf b'.

### E.1.2 The added mass coefficient in sway, $C_{A22}$

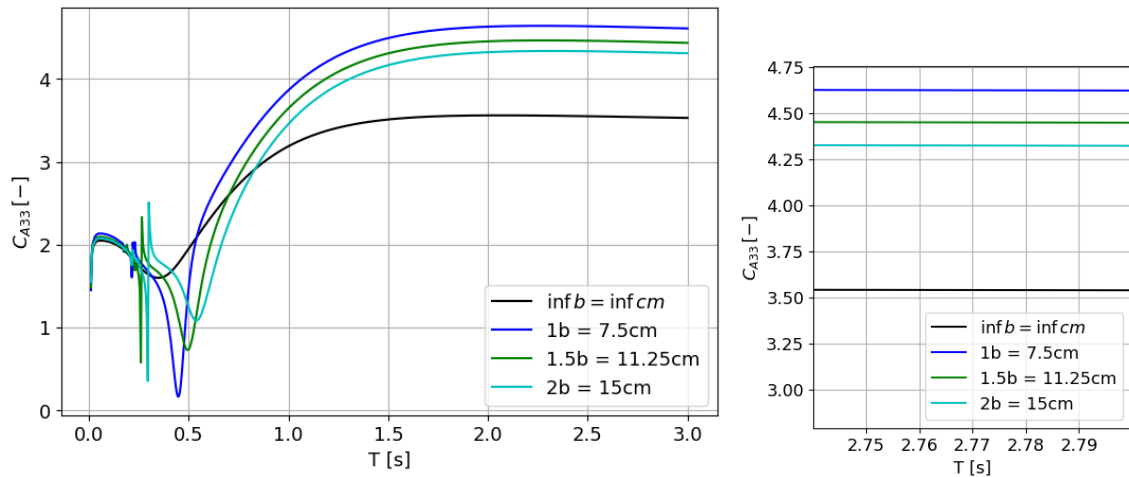


(a) The added mass coefficient  $C_{A22}$  plotted for period  $T \leq 3$  seconds.

(b) The added mass coefficient  $C_{A22}$  plotted for long crested waves and close to convergence.

Figure E.2: The added mass coefficient in sway  $C_{A22}$  for the small-draft models analysed in WAMIT.  $C_{A22}$  is plotted with three gap distance configurations, in addition to the infinite gap distance that is denoted ' $inf\ b$ '.

### E.1.3 The added mass coefficient in heave, $C_{A33}$

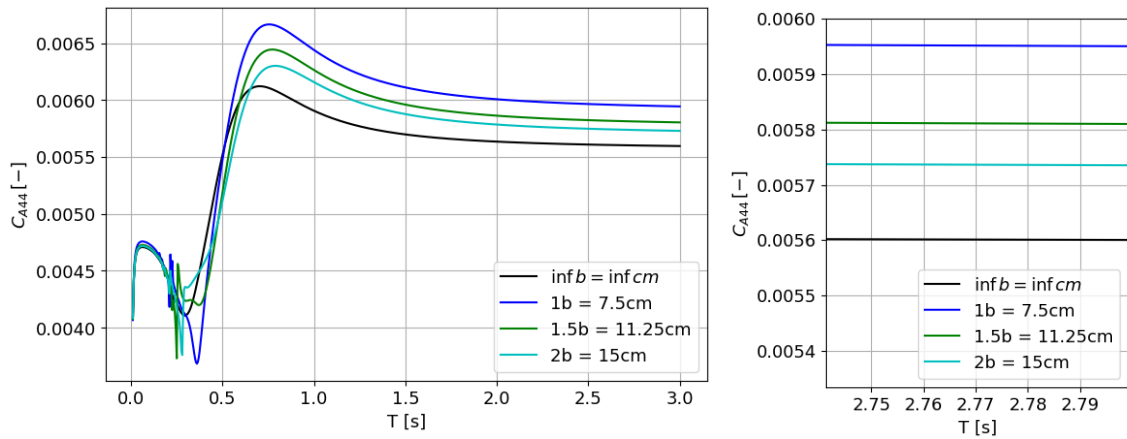


(a) The added mass coefficient  $C_{A33}$  plotted for period  $T \leq 3$  seconds.

(b) The added mass coefficient  $C_{A33}$  plotted for long crested waves and close to convergence.

Figure E.3: The added mass coefficient in heave  $C_{A33}$  for the small-draft models analysed in WAMIT.  $C_{A33}$  is plotted with three gap distance configurations, in addition to the infinite gap distance that is denoted ' $inf\ b$ '.

### E.1.4 The added mass coefficient in roll, $C_{A44}$

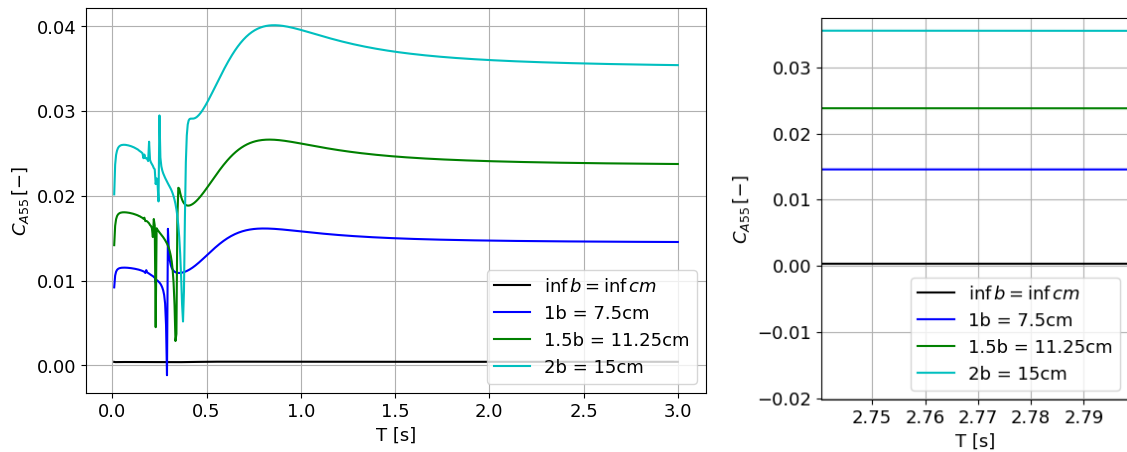


(a) The added mass coefficient  $C_{A44}$  plotted for period  $T \leq 3$  seconds.

(b) The added mass coefficient  $C_{A44}$  plotted for long crested waves and close to convergence.

Figure E.4: The added mass coefficient in roll  $C_{A44}$  for the small-draft models analysed in WAMIT.  $C_{A44}$  is plotted with three gap distance configurations, in addition to the infinite gap distance that is denoted 'inf  $b$ '.

### E.1.5 The added mass coefficient in pitch, $C_{A55}$

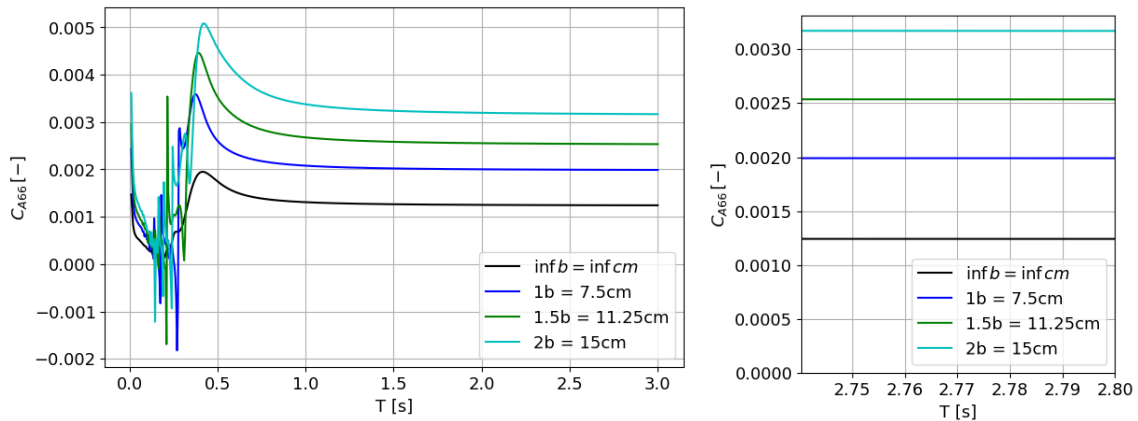


(a) The added mass coefficient  $C_{A55}$  plotted for period  $T \leq 3$  seconds.

(b) The added mass coefficient  $C_{A55}$  plotted for long crested waves and close to convergence.

Figure E.5: The added mass coefficient in pitch  $C_{A55}$  for the small-draft models analysed in WAMIT.  $C_{A55}$  is plotted with three gap distance configurations, in addition to the infinite gap distance that is denoted 'inf  $b$ '.

## E.1.6 The added mass coefficient in yaw, $C_{A66}$

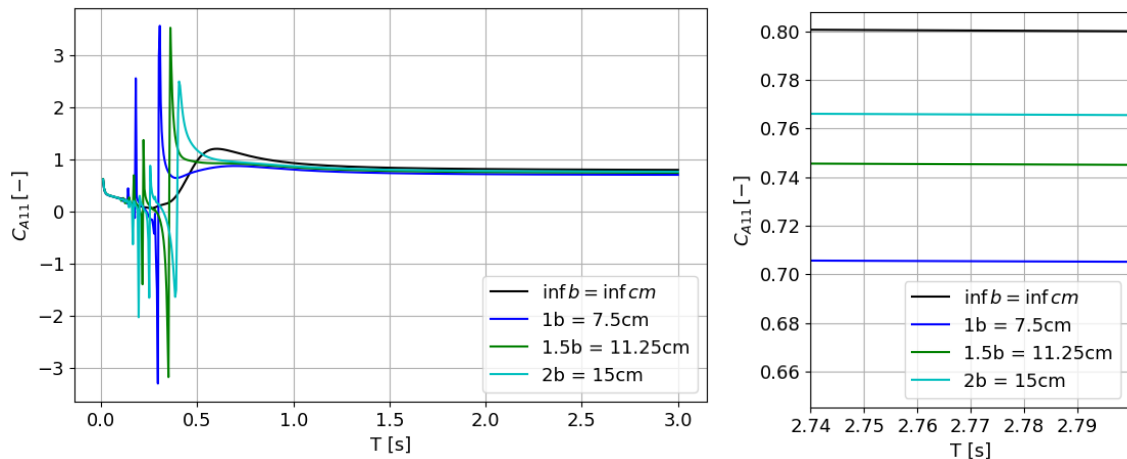


(a) The added mass coefficient  $C_{A66}$  plotted for period  $T \leq 3$  seconds. (b) The added mass coefficient  $C_{A66}$  plotted for long crested waves and close to convergence.

Figure E.6: The added mass coefficient in yaw  $C_{A66}$  for the small-draft models analysed in WAMIT.  $C_{A66}$  is plotted with three gap distance configurations, in addition to the infinite gap distance that is denoted ' $inf b$ '.

## E.2 Large-draft models

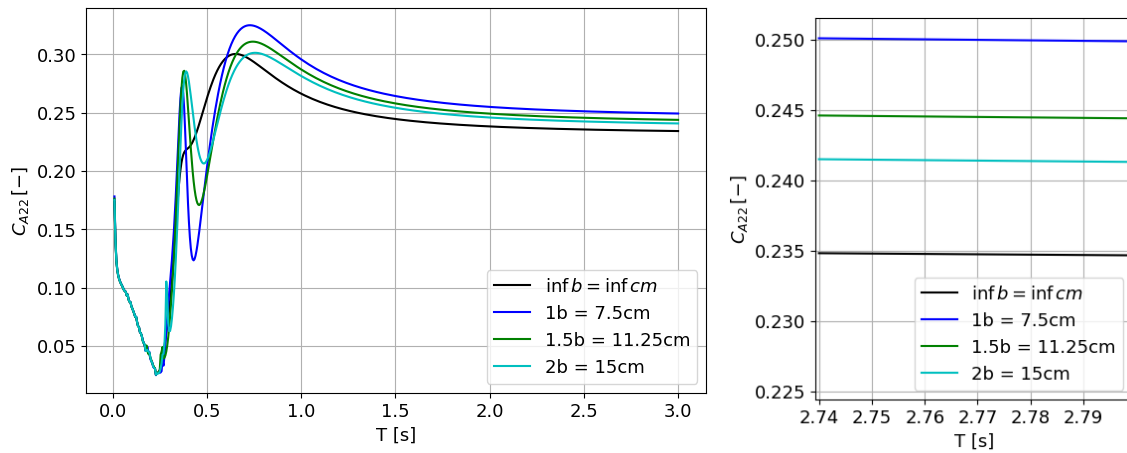
### E.2.1 The added mass coefficients in surge, $C_{A11}$



(a) The added mass coefficient  $C_{A11}$  plotted for period  $T \leq 3$  seconds. (b) The added mass coefficient  $C_{A11}$  plotted for long crested waves and close to convergence.

Figure E.7: The added mass coefficient in surge  $C_{A11}$  for the large-draft models analysed in WAMIT.  $C_{A11}$  is plotted with three gap distance configurations, in addition to the infinite gap distance that is denoted ' $inf b$ '.

## E.2.2 The added mass coefficient in sway, $C_{A22}$

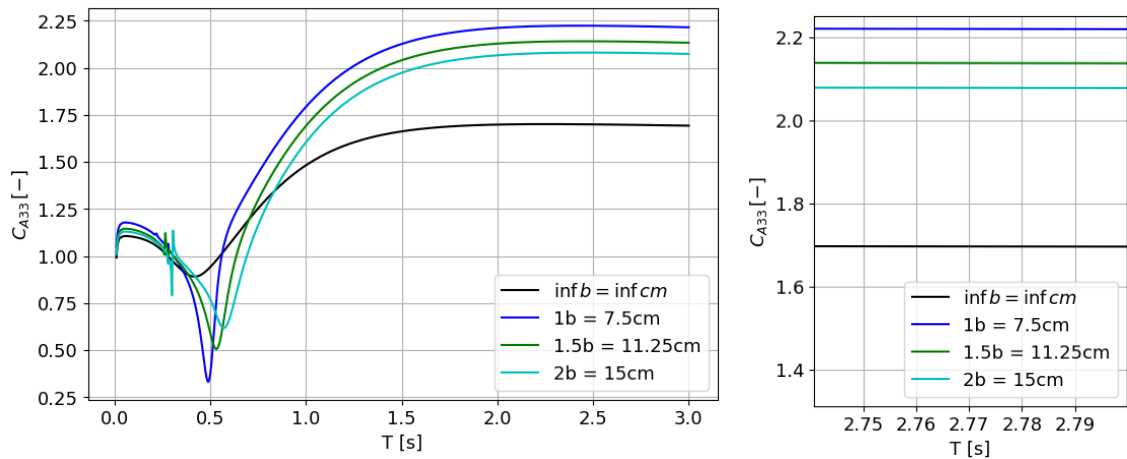


(a) The added mass coefficient  $C_{A22}$  plotted for period  $T \leq 3$  seconds.

(b) The added mass coefficient  $C_{A22}$  plotted for long crested waves and close to convergence.

Figure E.8: The added mass coefficient in sway  $C_{A22}$  for the large-draft models analysed in WAMIT.  $C_{A22}$  is plotted with three gap distance configurations, in addition to the infinite gap distance that is denoted 'inf b'.

## E.2.3 The added mass coefficient in heave, $C_{A33}$

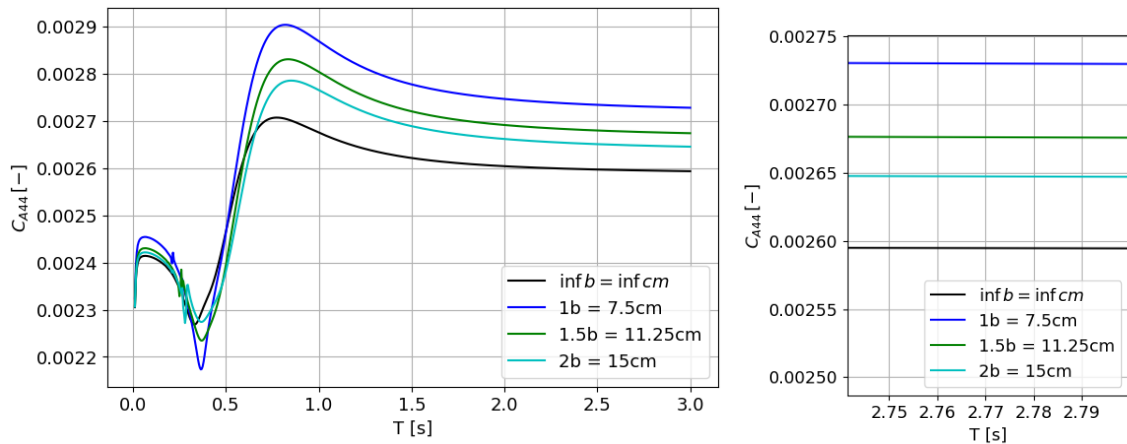


(a) The added mass coefficient  $C_{A33}$  plotted for period  $T \leq 3$  seconds.

(b) The added mass coefficient  $C_{A33}$  plotted for long crested waves and close to convergence.

Figure E.9: The added mass coefficient in heave  $C_{A33}$  for the large-draft models analysed in WAMIT.  $C_{A33}$  is plotted with three gap distance configurations, in addition to the infinite gap distance that is denoted 'inf b'.

## E.2.4 The added mass coefficient in roll, $C_{A44}$

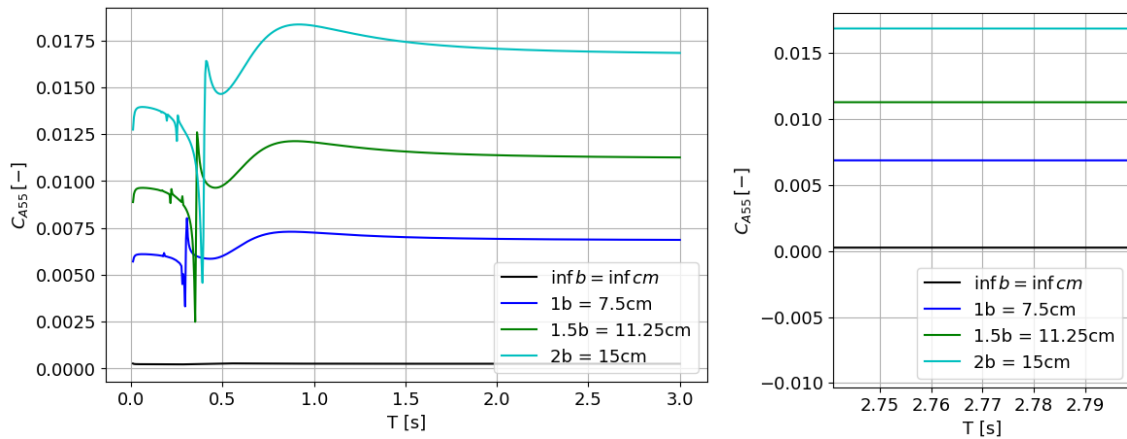


(a) The added mass coefficient  $C_{A44}$  plotted for period  $T \leq 3$  seconds.

(b) The added mass coefficient  $C_{A44}$  plotted for long crested waves and close to convergence.

Figure E.10: The added mass coefficient in roll  $C_{A44}$  for the large-draft models analysed in WAMIT.  $C_{A44}$  is plotted with three gap distance configurations, in addition to the infinite gap distance that is denoted ' $inf\ b$ '.

## E.2.5 The added mass coefficient in pitch, $C_{A55}$

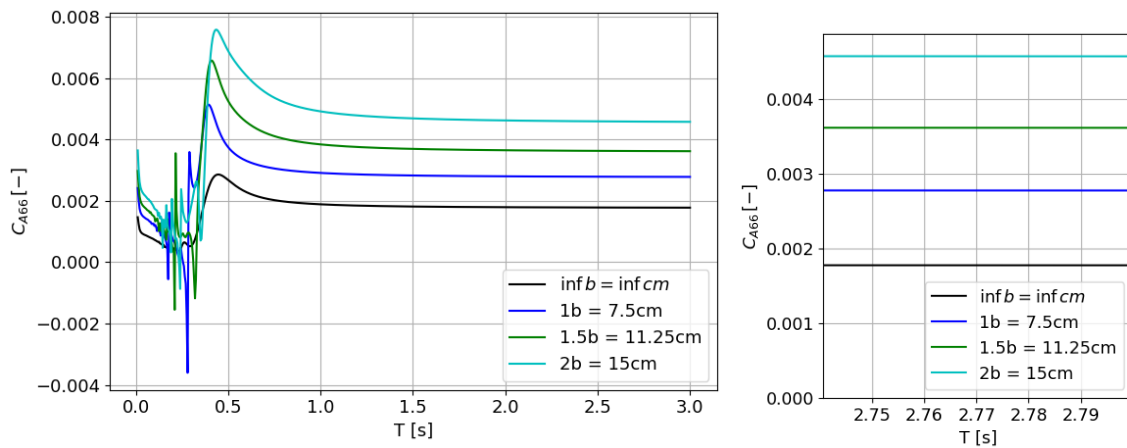


(a) The added mass coefficient  $C_{A55}$  plotted for period  $T \leq 3$  seconds.

(b) The added mass coefficient  $C_{A55}$  plotted for long crested waves and close to convergence.

Figure E.11: The added mass coefficient in pitch  $C_{A55}$  for the large-draft models analysed in WAMIT.  $C_{A55}$  is plotted with three gap distance configurations, in addition to the infinite gap distance that is denoted ' $inf\ b$ '.

## E.2.6 The added mass coefficient in yaw, $C_{A66}$



(a) The added mass coefficient  $C_{A66}$  plotted for period  $T \leq 3$  seconds.

(b) The added mass coefficient  $C_{A66}$  plotted for long crested waves and close to convergence.

Figure E.12: The added mass coefficient in yaw  $C_{A66}$  for the large-draft models analysed in WAMIT.  $C_{A66}$  is plotted with three gap distance configurations, in addition to the infinite gap distance that is denoted ' $inf b$ '.

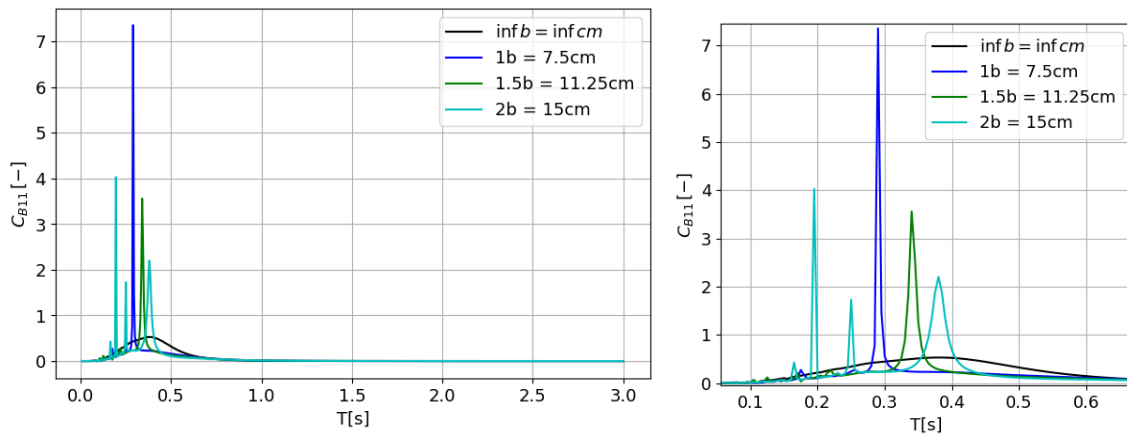


# Appendix F

## Damping coefficients in 6 Degrees Of Freedom (DOF)

### F.1 Small-draft models

#### F.1.1 The damping coefficients in surge, $C_{B11}$

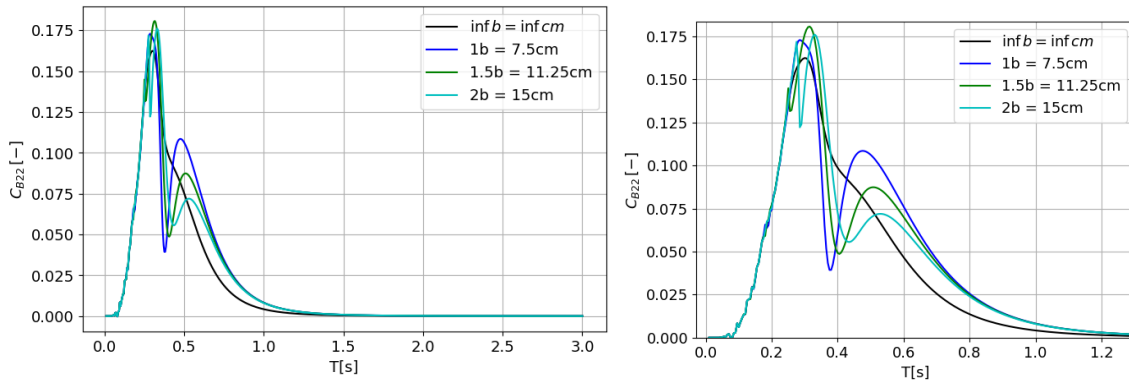


(a) The damping coefficient  $C_{B11}$  plotted for period  $T \leq 3$  seconds.

(b) The damping coefficient  $C_{B11}$  plotted for long crested waves and close to convergence.

Figure F.1: The damping coefficient in surge  $C_{B11}$  for the small-draft models analysed in WAMIT.  $C_{B11}$  is plotted with three gap distance configurations, in addition to the infinite gap distance that is denoted '*inf b*'.

### F.1.2 The damping coefficient in sway, $C_{B22}$

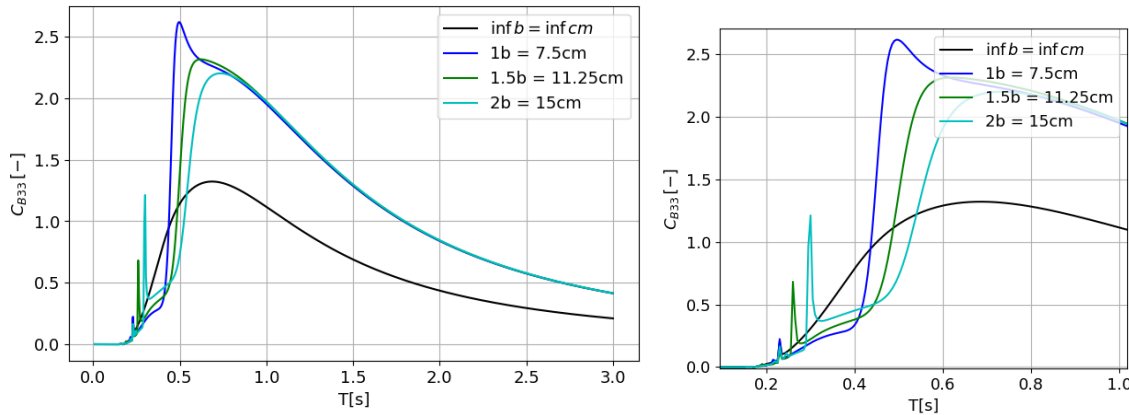


(a) The damping coefficient  $C_{B22}$  plotted for period  $T \leq 3$  seconds.

(b) The damping coefficient  $C_{B22}$  plotted for long crested waves and close to convergence.

Figure F.2: The damping coefficient in sway  $C_{B22}$  for the small-draft models analysed in WAMIT.  $C_{B22}$  is plotted with three gap distance configurations, in addition to the infinite gap distance that is denoted 'inf b'.

### F.1.3 The damping coefficient in heave, $C_{B33}$

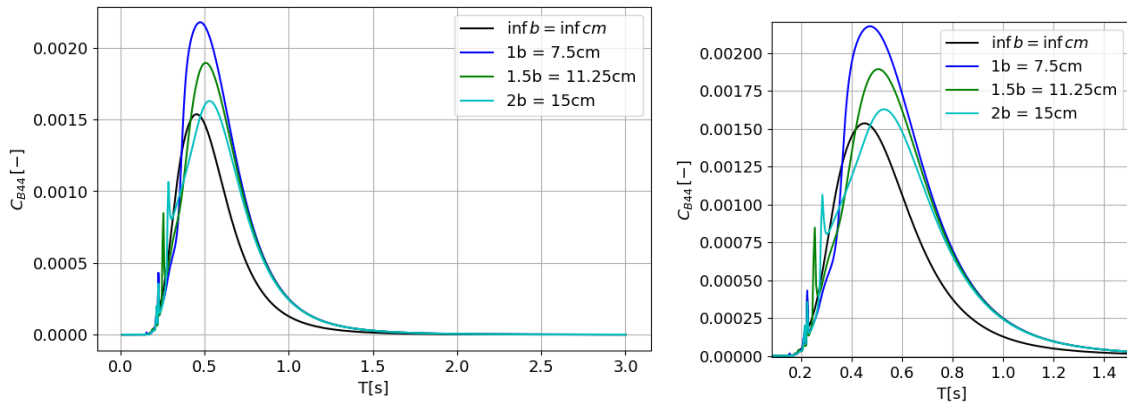


(a) The damping coefficient  $C_{B33}$  plotted for period  $T \leq 3$  seconds.

(b) The damping coefficient  $C_{B33}$  plotted for long crested waves and close to convergence.

Figure F.3: The damping coefficient in heave  $C_{B33}$  for the small-draft models analysed in WAMIT.  $C_{B33}$  is plotted with three gap distance configurations, in addition to the infinite gap distance that is denoted 'inf b'.

### F.1.4 The damping coefficient in roll, $C_{B44}$

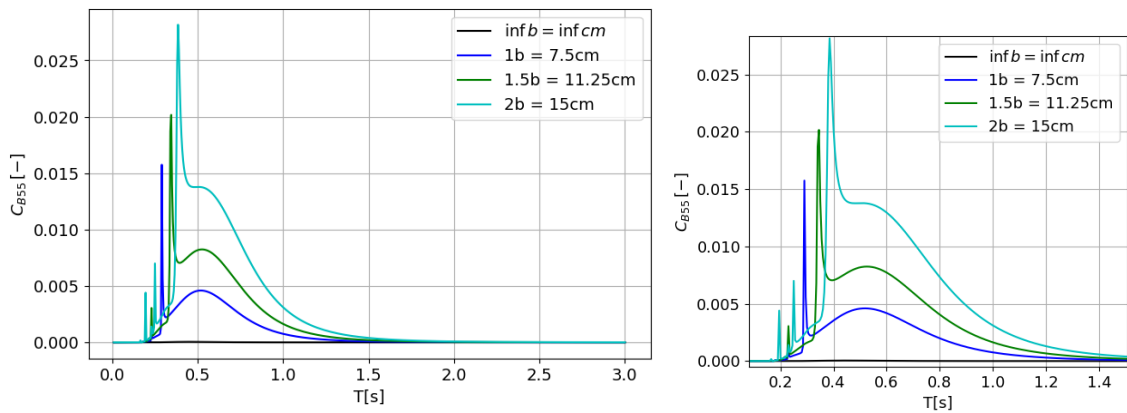


(a) The damping coefficient  $C_{B44}$  plotted for period  $T \leq 3$  seconds.

(b) The damping coefficient  $C_{B44}$  plotted for long crested waves and close to convergence.

Figure F.4: The damping coefficient in roll  $C_{B44}$  for the small-draft models analysed in WAMIT.  $C_{B44}$  is plotted with three gap distance configurations, in addition to the infinite gap distance that is denoted 'inf b'.

### F.1.5 The damping coefficient in pitch, $C_{B55}$

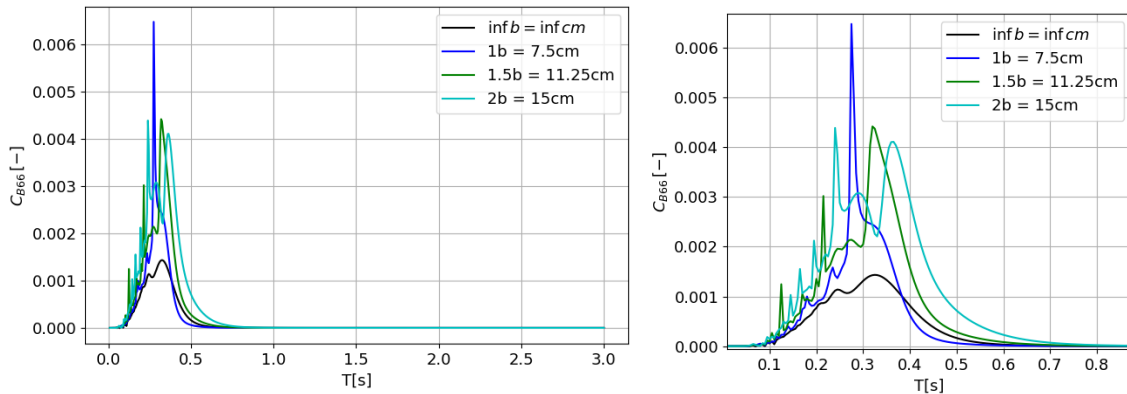


(a) The damping coefficient  $C_{B55}$  plotted for period  $T \leq 3$  seconds.

(b) The damping coefficient  $C_{B55}$  plotted for long crested waves and close to convergence.

Figure F.5: The damping coefficient in pitch  $C_{B55}$  for the small-draft models analysed in WAMIT.  $C_{B55}$  is plotted with three gap distance configurations, in addition to the infinite gap distance that is denoted 'inf b'.

## F.1.6 The damping coefficient in yaw, $C_{B66}$



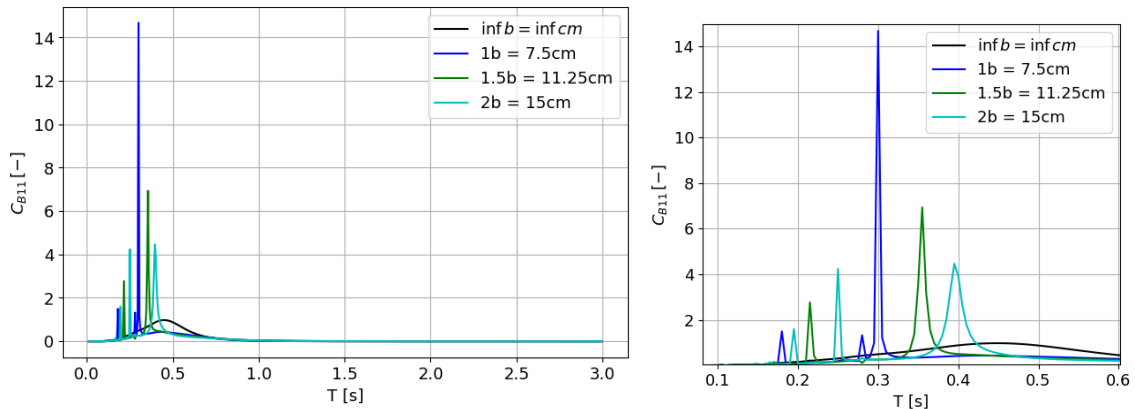
(a) The damping coefficient  $C_{B66}$  plotted for period  $T \leq 3$  seconds.

(b) The damping coefficient  $C_{B66}$  plotted for long crested waves and close to convergence.

Figure F.6: The damping coefficient in yaw  $C_{B66}$  for the small-draft models analysed in WAMIT.  $C_{B66}$  is plotted with three gap distance configurations, in addition to the infinite gap distance that is denoted ' $inf\ b$ '.

## F.2 Large-draft models

### F.2.1 The damping coefficients in surge, $C_{B11}$

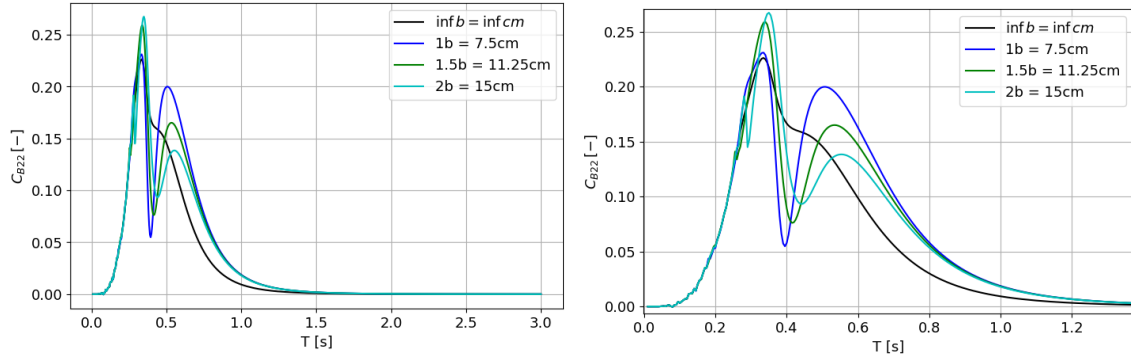


(a) The damping coefficient  $C_{B11}$  plotted for period  $T \leq 3$  seconds.

(b) The damping coefficient  $C_{B11}$  plotted for long crested waves and close to convergence.

Figure F.7: The damping coefficient in surge  $C_{B11}$  for the large-draft models analysed in WAMIT.  $C_{B11}$  is plotted with three gap distance configurations, in addition to the infinite gap distance that is denoted ' $inf\ b$ '.

## F.2.2 The damping coefficient in sway, $C_{B22}$

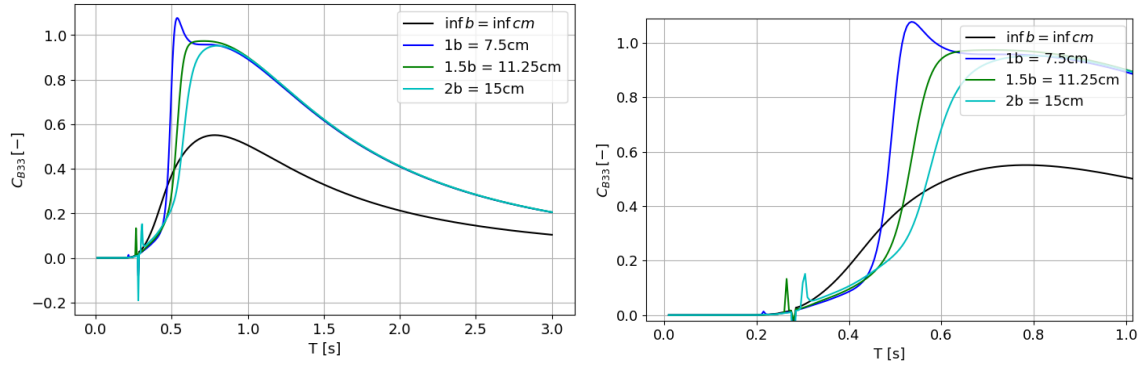


(a) The damping coefficient  $C_{B22}$  plotted for period  $T \leq 3$  seconds.

(b) The damping coefficient  $C_{B22}$  plotted for long crested waves and close to convergence.

Figure F.8: The damping coefficient in sway  $C_{B22}$  for the large-draft models analysed in WAMIT.  $C_{B22}$  is plotted with three gap distance configurations, in addition to the infinite gap distance that is denoted 'inf b'.

## F.2.3 The damping coefficient in heave, $C_{B33}$

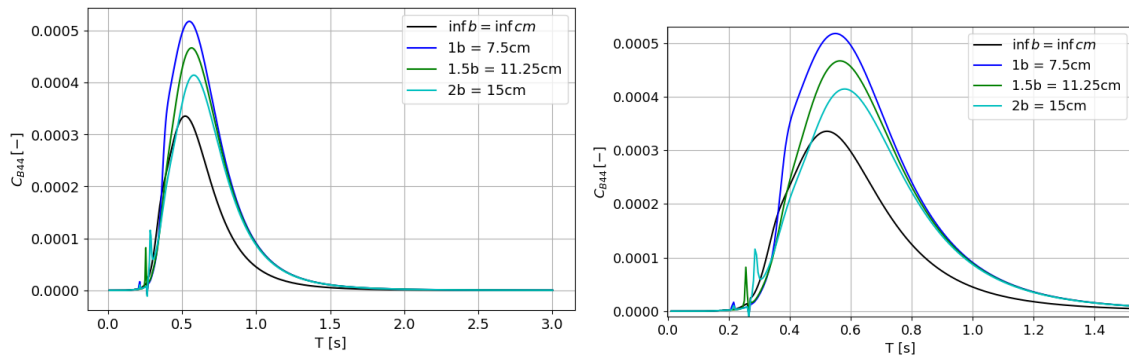


(a) The damping coefficient  $C_{B33}$  plotted for period  $T \leq 3$  seconds.

(b) The damping coefficient  $C_{B33}$  plotted for long crested waves and close to convergence.

Figure F.9: The damping coefficient in heave  $C_{B33}$  for the large-draft models analysed in WAMIT.  $C_{B33}$  is plotted with three gap distance configurations, in addition to the infinite gap distance that is denoted 'inf b'.

## F.2.4 The damping coefficient in roll, $C_{B44}$

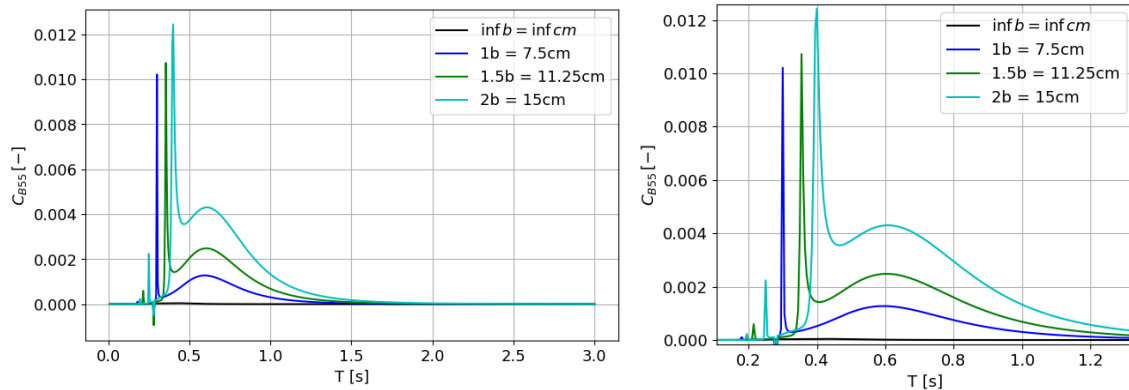


(a) The damping coefficient  $C_{B44}$  plotted for period  $T \leq 3$  seconds.

(b) The damping coefficient  $C_{B44}$  plotted for long crested waves and close to convergence.

Figure F.10: The damping coefficient in roll  $C_{B44}$  for the large-draft models analysed in WAMIT.  $C_{B44}$  is plotted with three gap distance configurations, in addition to the infinite gap distance that is denoted 'inf b'.

## F.2.5 The damping coefficient in pitch, $C_{B55}$

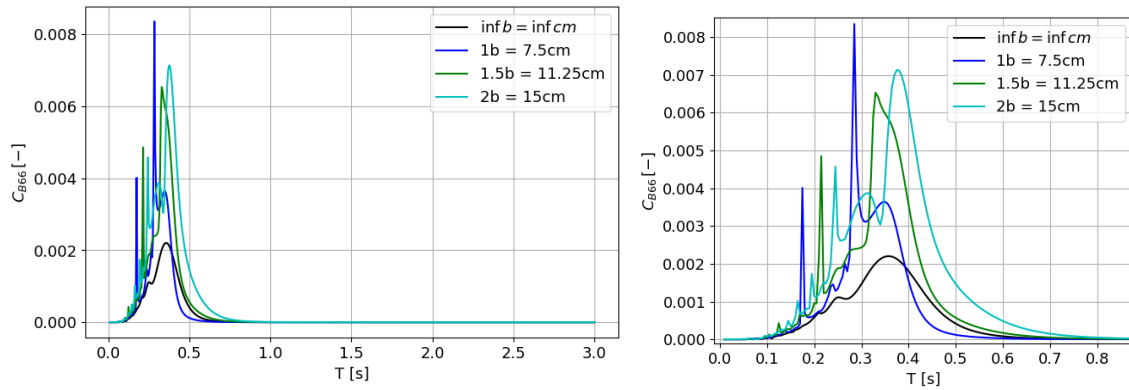


(a) The damping coefficient  $C_{B55}$  plotted for period  $T \leq 3$  seconds.

(b) The damping coefficient  $C_{B55}$  plotted for long crested waves and close to convergence.

Figure F.11: The damping coefficient in pitch  $C_{B55}$  for the large-draft models analysed in WAMIT.  $C_{B55}$  is plotted with three gap distance configurations, in addition to the infinite gap distance that is denoted 'inf b'.

## F.2.6 The damping coefficient in yaw, $C_{B66}$



(a) The damping coefficient  $C_{B66}$  plotted for period  $T \leq 3$  seconds.

(b) The damping coefficient  $C_{B66}$  plotted for long crested waves and close to convergence.

Figure F.12: The damping coefficient in yaw  $C_{B66}$  for the large-draft models analysed in WAMIT.  $C_{B66}$  is plotted with three gap distance configurations, in addition to the infinite gap distance that is denoted 'inf b'.

# Appendix G

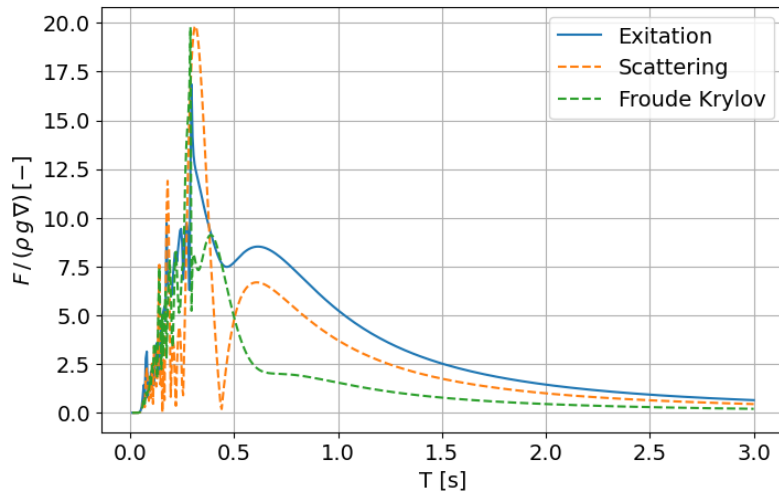
## Exciting forces

### G.1 Small-draft models

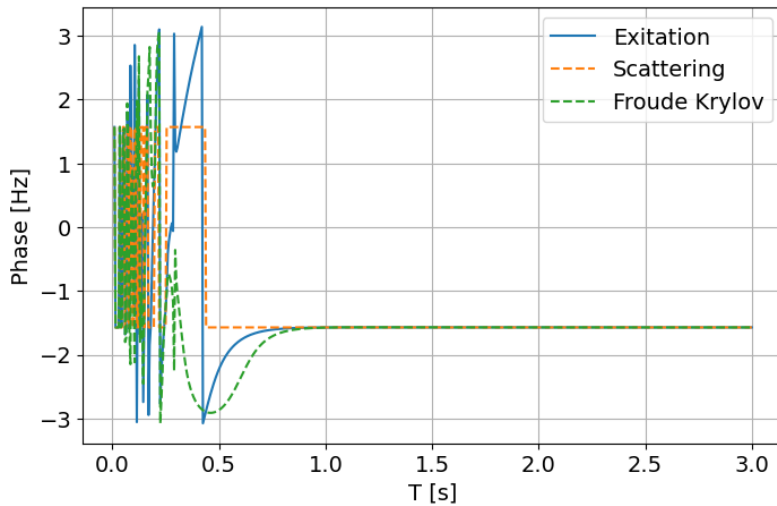


---

### G.1.1 Case 1



(a) Total excitation force coefficient, Froude-Krylov force coefficient and the scattering force coefficient plotted.

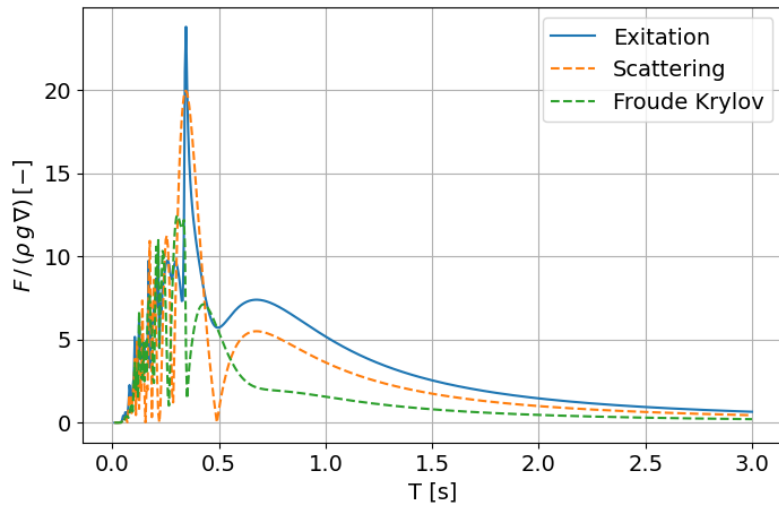


(b) The corresponding phase.

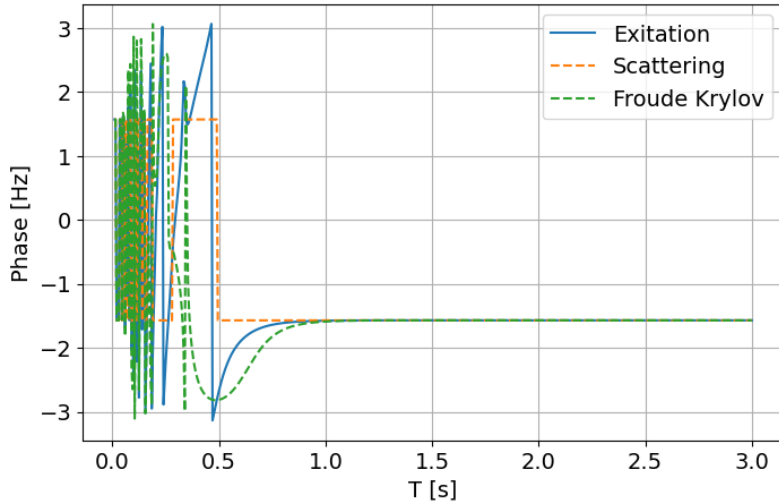
Figure G.1: Total excitation force coefficient, Froude-Krylov force coefficient and the scattering force coefficient plotted with the corresponding phase for period  $T \leq 3$  seconds. The case presented is for case 1 gap distance with small-draft models,  $H/b = 1.5/7.5$ .

---

## G.1.2 Case 2



(a) Total excitation force coefficient, Froude-Krylov force coefficient and the scattering force coefficient plotted.

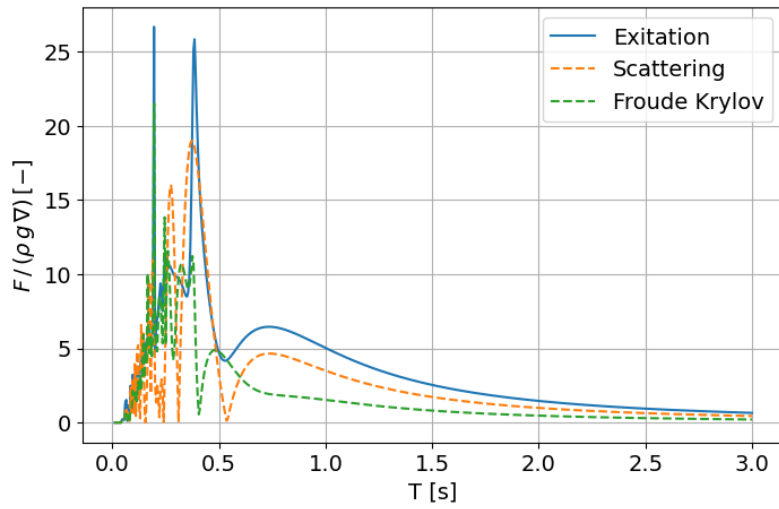


(b) The corresponding phase.

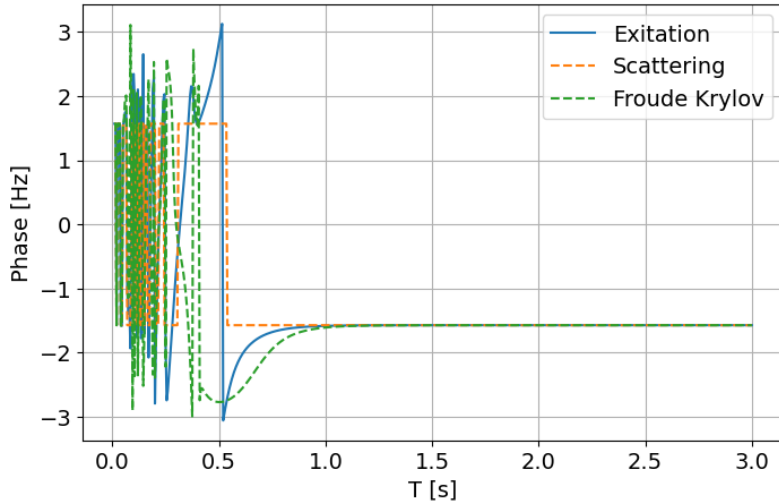
Figure G.2: Total excitation force coefficient, Froude-Krylov force coefficient and the scattering force coefficient plotted with the corresponding phase for period  $T \leq 3$  seconds. The case presented is for case 2 gap distance with small-draft models,  $H/b = 1.5/11.25$ .

---

### G.1.3 Case 3



(a) Total excitation force coefficient, Froude-Krylov force coefficient and the scattering force coefficient plotted.



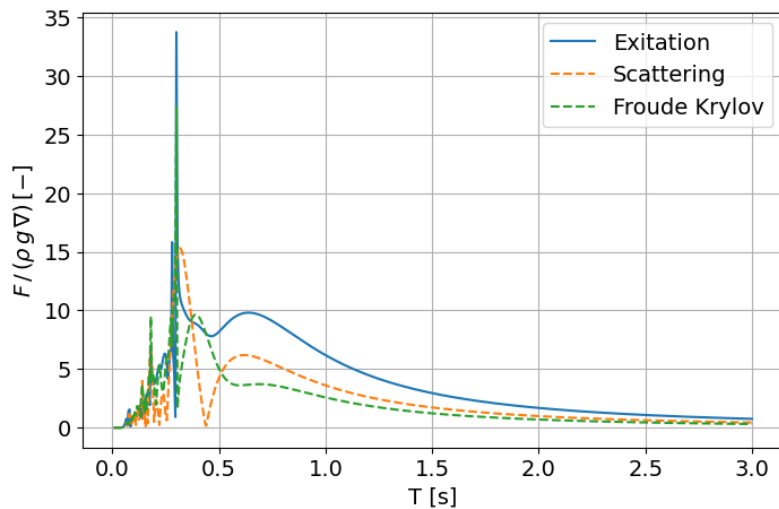
(b) The corresponding phase.

Figure G.3: Total excitation force coefficient, Froude-Krylov force coefficient and the scattering force coefficient plotted with the corresponding phase for period  $T \leq 3$  seconds. The case presented is for case 3 gap distance with small-draft models,  $H/b = 1.5/15$ .

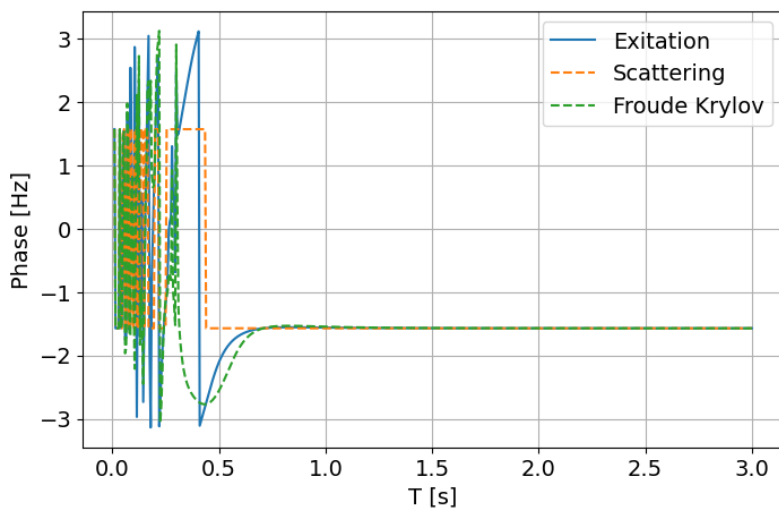
---

## G.2 Large-draft models

### G.2.1 Case 1



(a) Total excitation force coefficient, Froude-Krylov force coefficient and the scattering force coefficient plotted.

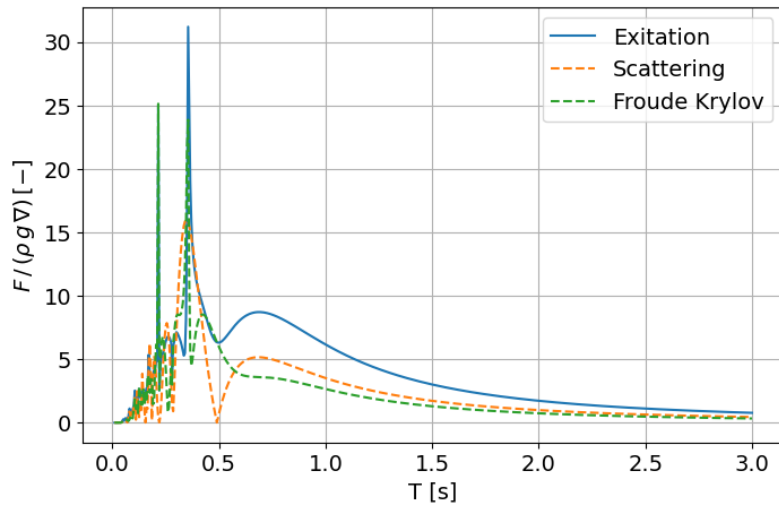


(b) The corresponding phase.

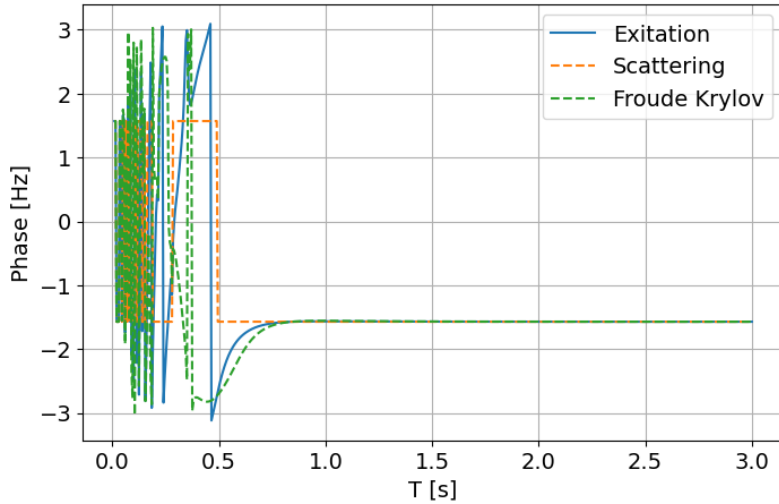
Figure G.4: Total excitation force coefficient, Froude-Krylov force coefficient and the scattering force coefficient plotted with the corresponding phase for period  $T \leq 3$  seconds. The case presented is for case 1 gap distance with large-draft models,  $H/b = 3/7.5$ .

---

## G.2.2 Case 2



(a) Total excitation force coefficient, Froude-Krylov force coefficient and the scattering force coefficient plotted.

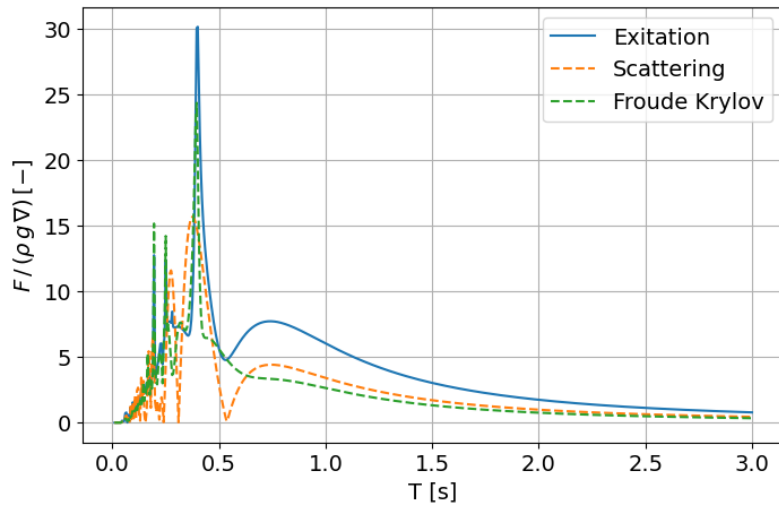


(b) The corresponding phase.

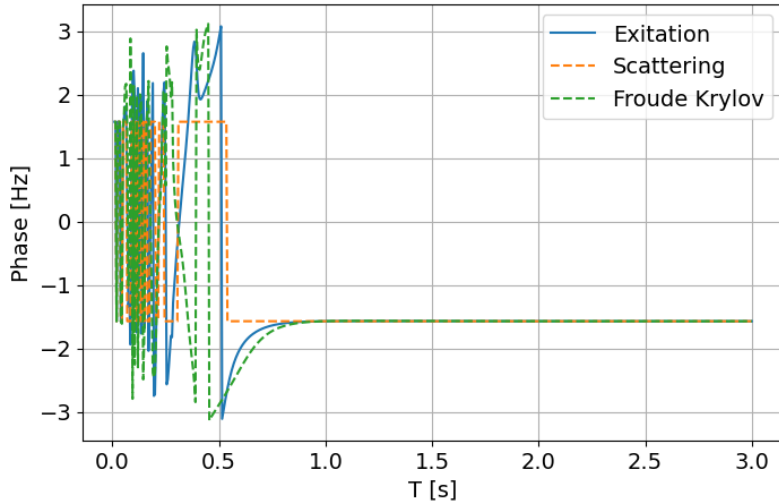
Figure G.5: Total excitation force coefficient, Froude-Krylov force coefficient and the scattering force coefficient plotted with the corresponding phase for period  $T \leq 3$  seconds. The case presented is for case 2 gap distance with large-draft models,  $H/b = 3/11.25$ .

---

### G.2.3 Case 3



(a) Total excitation force coefficient, Froude-Krylov force coefficient and the scattering force coefficient plotted.



(b) The corresponding phase.

Figure G.6: Total excitation force coefficient, Froude-Krylov force coefficient and the scattering force coefficient plotted with the corresponding phase for period  $T \leq 3$  seconds. The case presented is for case 3 gap distance with large-draft models,  $H/b = 3/15$ .

# Appendix H

## Force component, $F^\omega$ s with unit Newton [N]

### H.1 Case 1, small-draft models

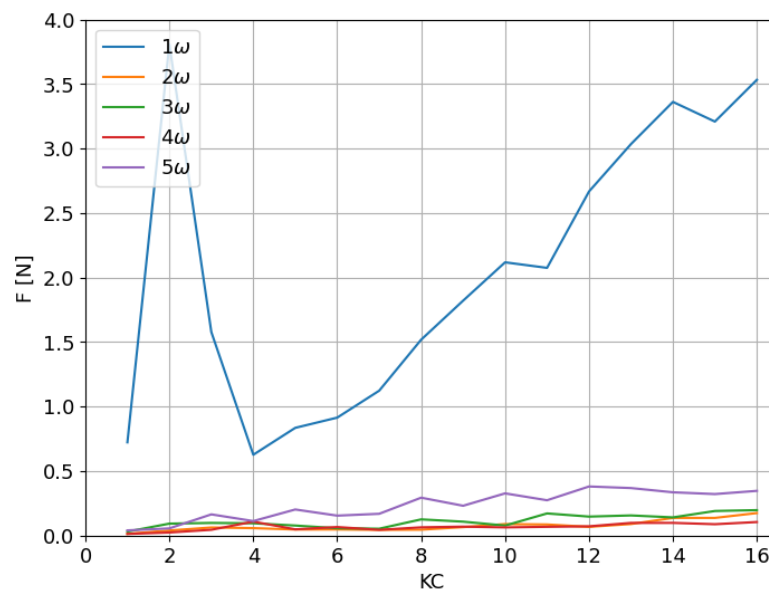


Figure H.1: The force components  $F^\omega$  for case 1 for the small-draft models and are plotted for  $KC \leq 16$ . Case 1 small,  $H/b = 1.5/7.5$ .

---

## H.2 Case 1, large-draft models

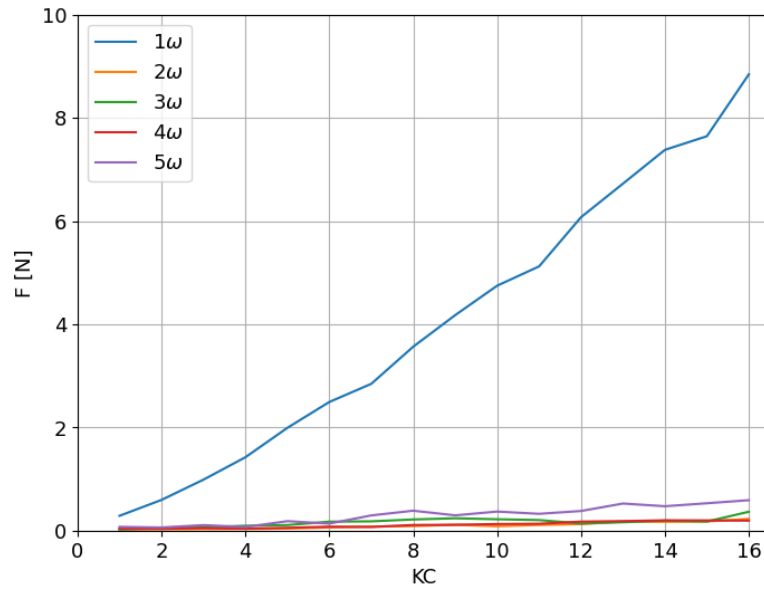


Figure H.2: The force components  $F^\omega$  for case 1 for the large-draft models and are plotted for  $KC \leq 16$ . Case 1 large,  $H/b = 3/7.5$ .

## H.3 Case 2, small-draft models

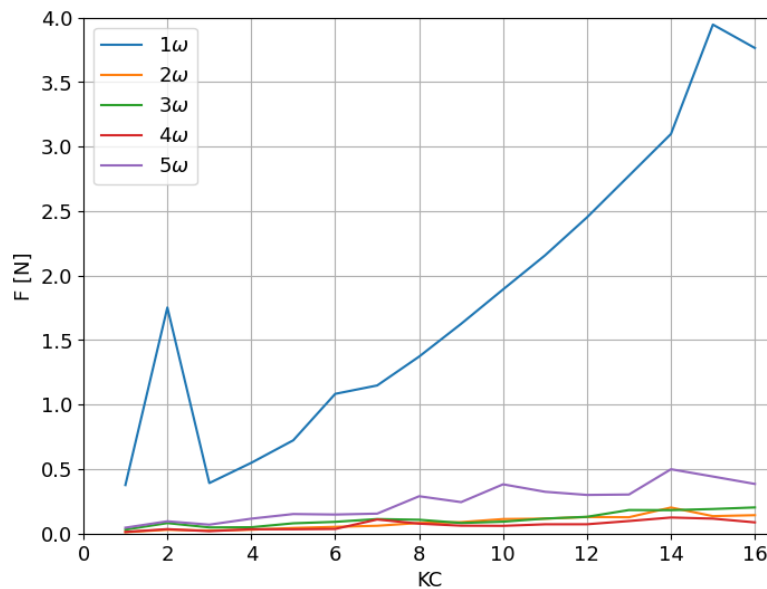


Figure H.3: The force components  $F^\omega$  for case 2 for the small-draft models and are plotted for  $KC \leq 16$ . Case 2 small,  $H/b = 1.5/11.25$ .



---

## H.4 Case 2, large-draft models

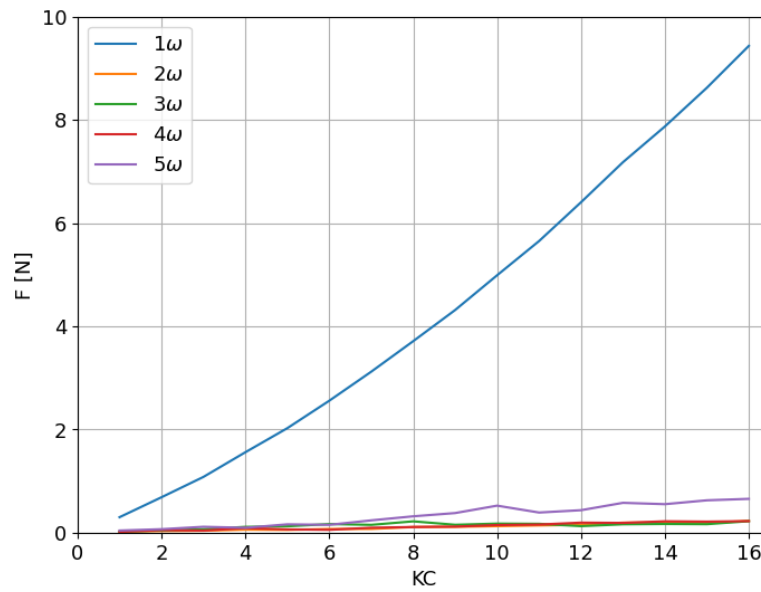


Figure H.4: The force components  $F^\omega$  for case 2 for the large-draft models and are plotted for  $KC \leq 16$ . Case 2 large,  $H/b = 3/11.25$ .

## H.5 Case 3, small-draft models

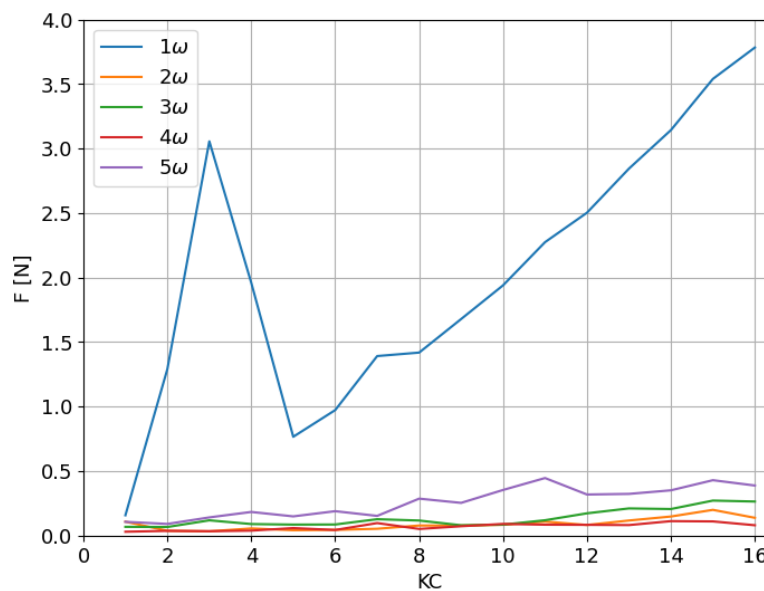


Figure H.5: The force components  $F^\omega$  for case 3 for the small-draft models and are plotted for  $KC \leq 16$ . Case 3 small,  $H/b = 1.5/15$ .

---

## H.6 Case 3, large-draft models

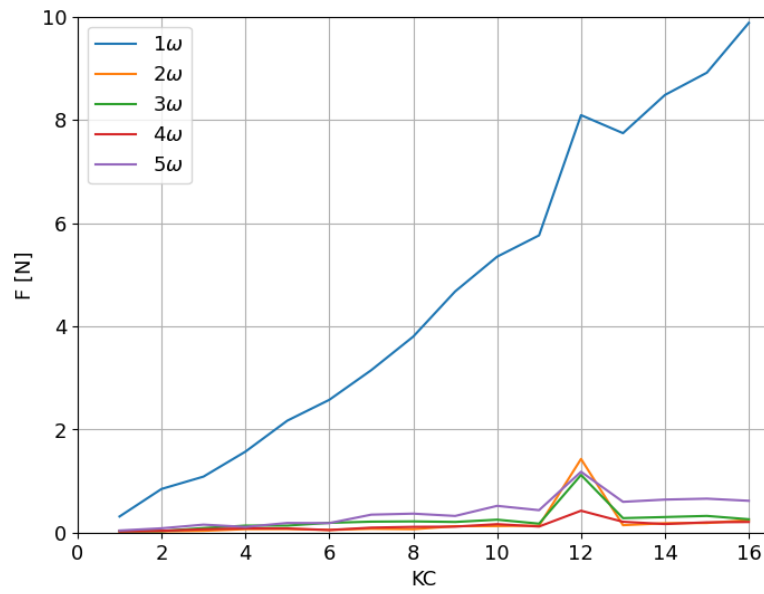


Figure H.6: The force components  $F^\omega$  for case 3 for the large-draft models and are plotted for  $KC \leq 16$ . Case 3 large,  $H/b = 3/15$ .

# Appendix I

The added mass component  $C_A$  and the drag coefficient  $C_D$  measured with small-draft models, plotted for  $KC = [1, 16]$

## I.1 Case 1

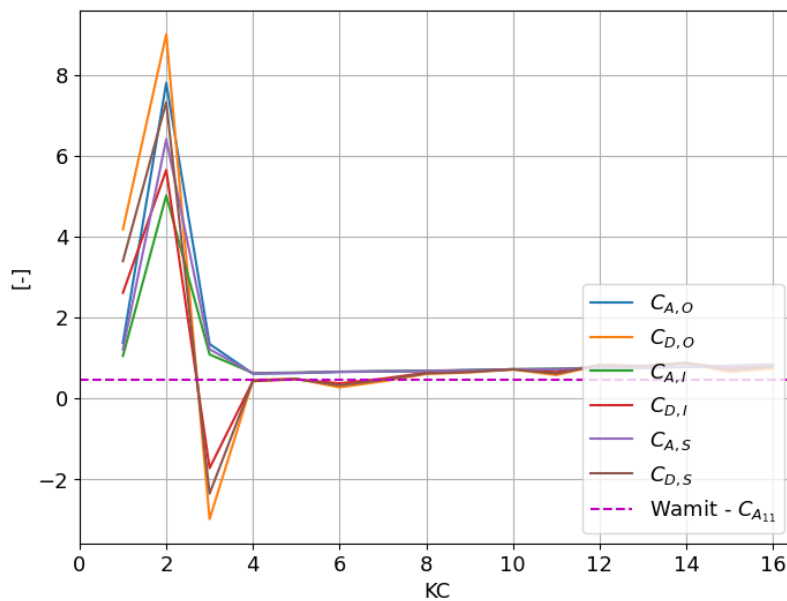


Figure I.1: Case 1 with small-draft models,  $H/b = 1.5/7.5$  The added mass  $C_A$  and drag coefficient  $C_D$  of the small-draft models attached to the outer and inner plate, measuring  $C_{A,O}$  and  $C_{A,I}$  plate. The sum  $C_{A,S}$  compared to  $C_{A11}$  from WAMIT.

---

## I.2 Case 2

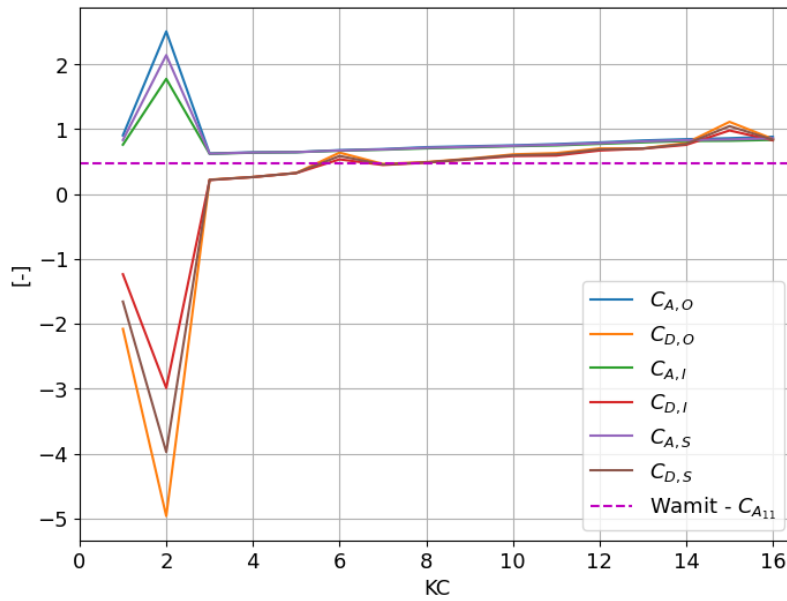


Figure I.2: Case 2 with small-draft models,  $H/b = 1.5/11.5$  The added mass  $C_A$  and drag coefficient  $C_D$  of the small-draft models attached to the outer and inner plate, measuring  $C_{A,O}$  and  $C_{A,I}$  plate. The sum  $C_{A,S}$  compared to  $C_{A11}$  from WAMIT.

## I.3 Case 3

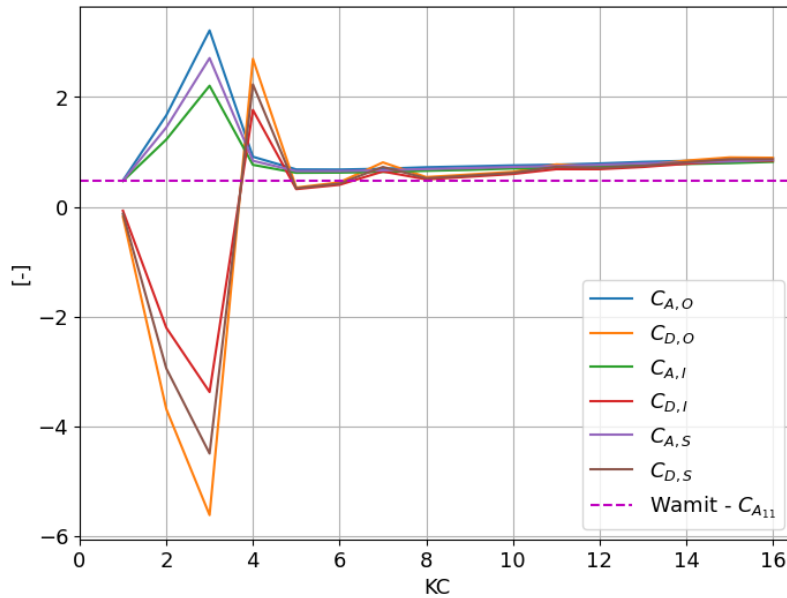


Figure I.3: Case 3 with small-draft models,  $H/b = 1.5/15$  The added mass  $C_A$  and drag coefficient  $C_D$  of the small-draft models attached to the outer and inner plate, measuring  $C_{A,O}$  and  $C_{A,I}$  plate. The sum  $C_{A,S}$  compared to  $C_{A11}$  from WAMIT.

# Appendix J

## Frequency spectra of the Hammer test

### J.1 Plates without models

#### J.1.1 Striking the tank in Y-direction

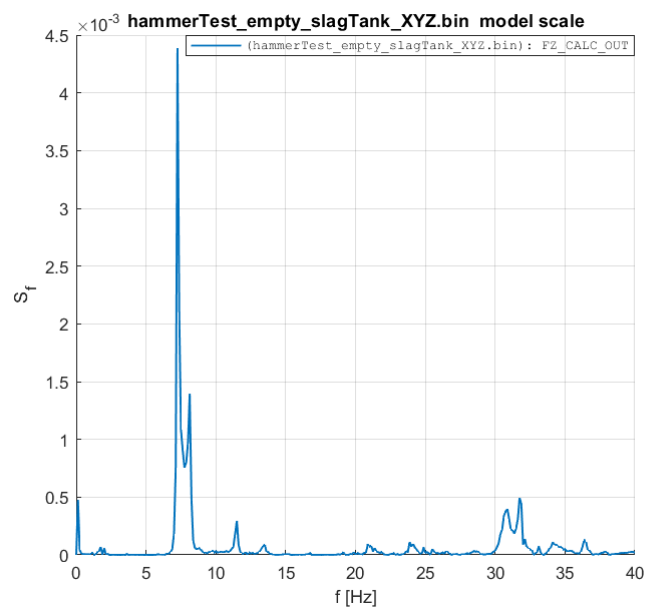


Figure J.1: Spectral analysis of the forces in Z-direction of the outer plate without models, when striking the tank in Y-direction.

---

### J.1.2 Striking the tank in Z-direction

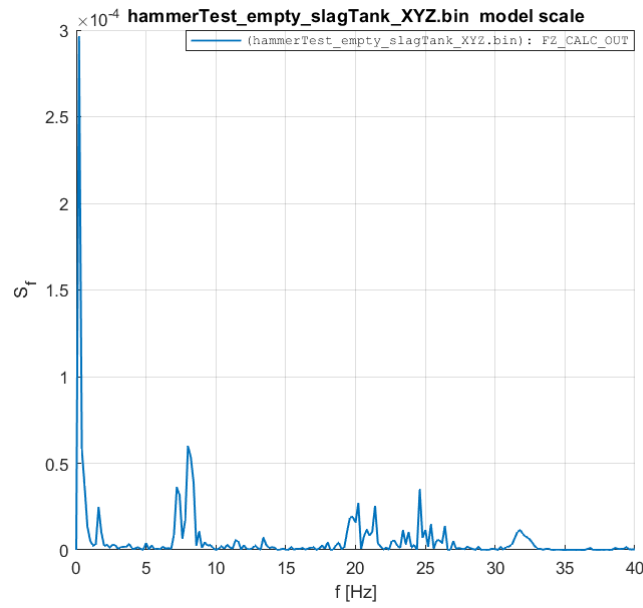


Figure J.2: Spectral analysis of the forces in Z-direction of the outer plate without models, when striking the tank in Z-direction.

### J.1.3 Striking the stronghold in X-direction

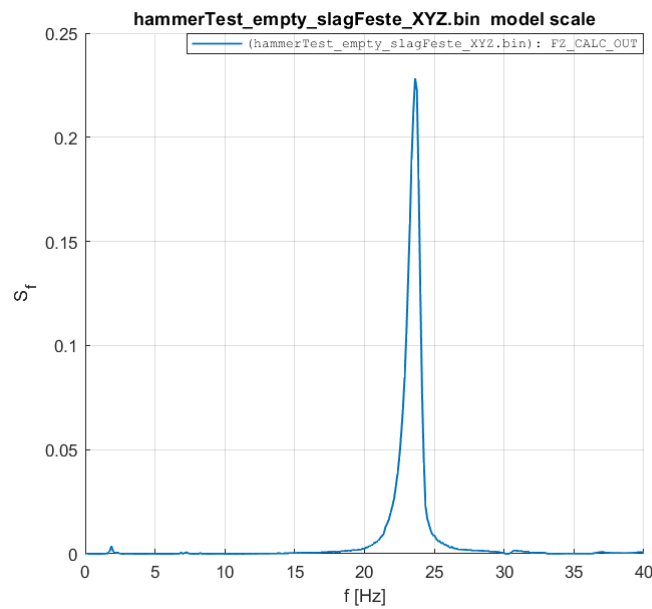


Figure J.3: Spectral analysis of the forces in Z-direction of the outer plate without models, when striking the stronghold in X-direction.

---

### J.1.4 Striking the stronghold in Y-direction

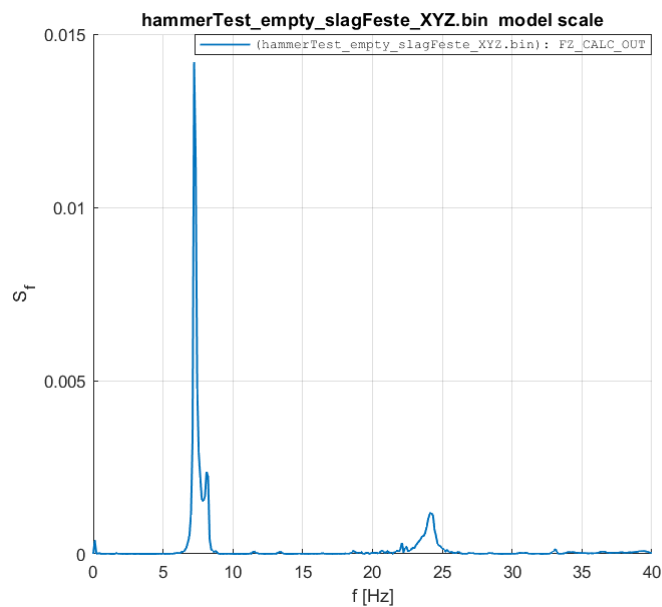


Figure J.4: Spectral analysis of the forces in Z-direction of the outer plate without models, when striking the stronghold in Y-direction.

### J.1.5 Striking the stronghold in Z-direction

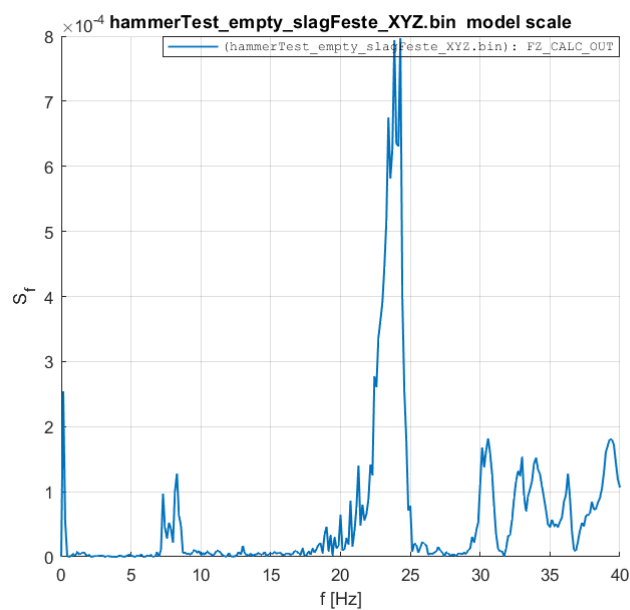


Figure J.5: Spectral analysis of the forces in Z-direction of the outer plate without models, when striking the stronghold in Z-direction.

---

## J.1.6 Striking the rig in X-direction

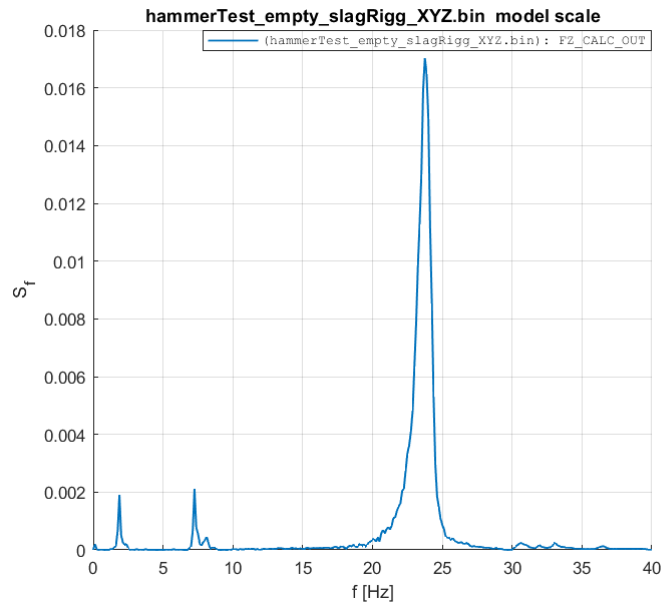


Figure J.6: Spectral analysis of the forces in Z-direction of the outer plate without models, when striking the rig in X-direction.

## J.1.7 Striking the rig in Y-direction

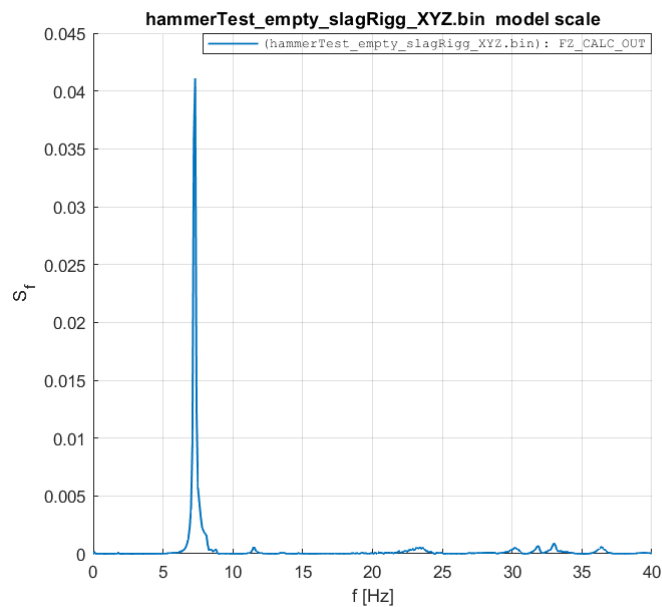


Figure J.7: Spectral analysis of the forces in Z-direction of the outer plate without models, when striking the rig in Y-direction.



---

### J.1.8 Striking the rig in Z-direction

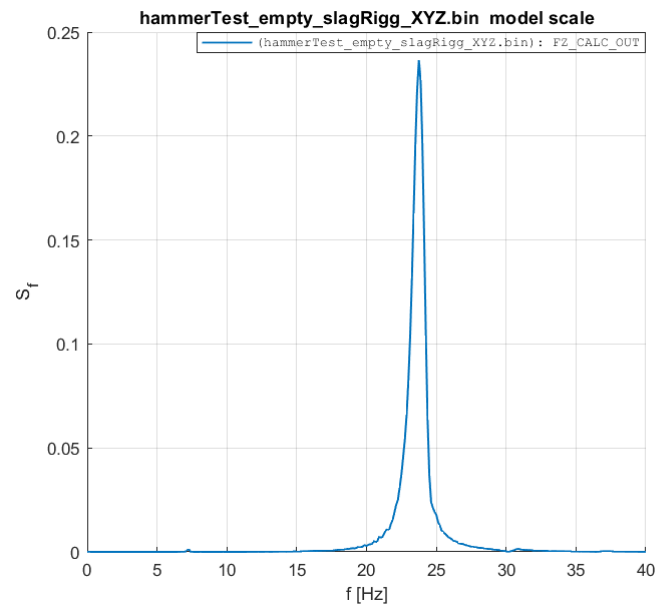


Figure J.8: Spectral analysis of the forces in Z-direction of the outer plate without models, when striking the rig in Z-direction.

### J.1.9 Striking the inner plate in X-direction, measuring at outer plate

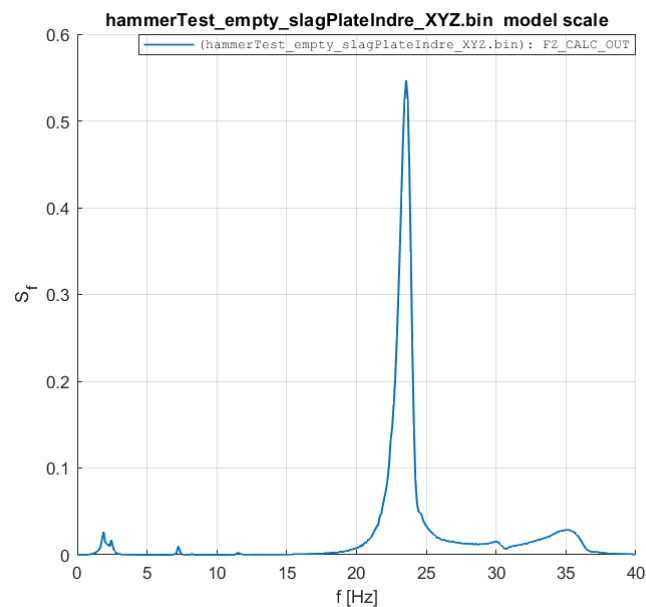


Figure J.9: Spectral analysis of the forces in Z-direction of the outer plate without models, when striking the inner plate in X-direction.

---

### J.1.10 Striking the inner plate in X-direction, measuring at inner plate

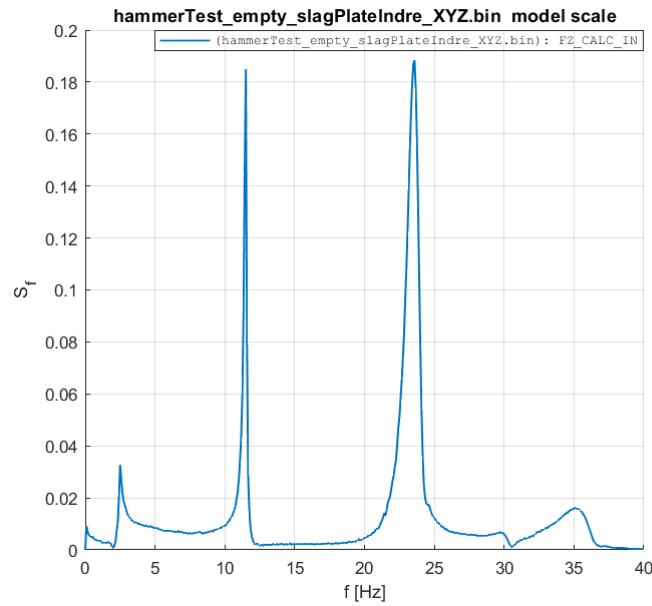


Figure J.10: Spectral analysis of the forces in Z-direction of the inner plate without models, when striking the inner plate in X-direction.

### J.1.11 Striking the inner plate in Y-direction, measuring at outer plate

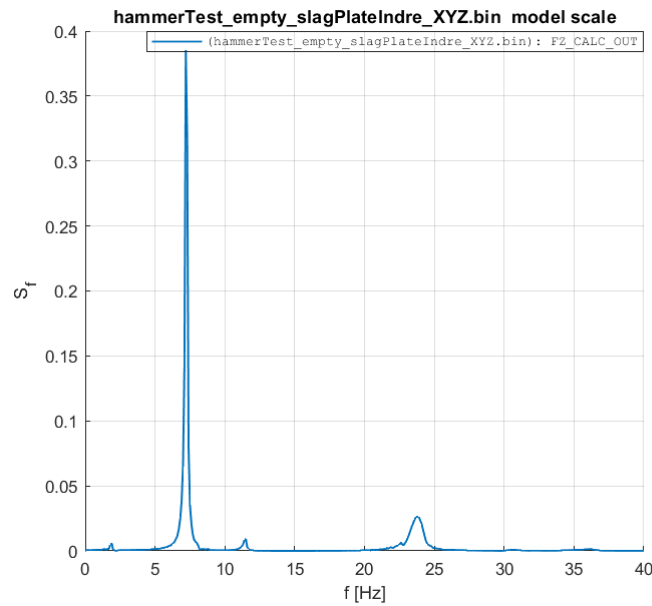


Figure J.11: Spectral analysis of the forces in Z-direction of the outer plate without models, when striking the inner plate in Y-direction.

---

### J.1.12 Striking the inner plate in Y-direction, measuring at inner plate

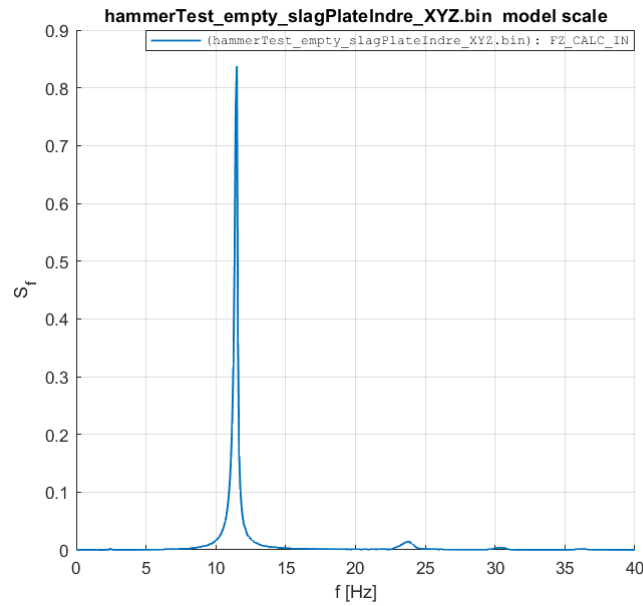


Figure J.12: Spectral analysis of the forces in Z-direction of the inner plate without models, when striking the inner plate in Y-direction.

### J.1.13 Striking the outer plate in X-direction, measuring at outer plate

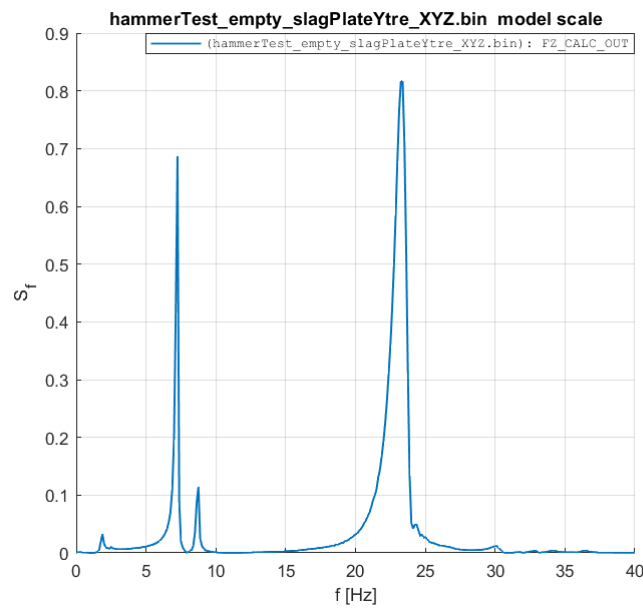


Figure J.13: Spectral analysis of the forces in Z-direction of the outer plate without models, when striking the outer plate in X-direction.

---

### J.1.14 Striking the outer plate in X-direction, measuring at inner plate

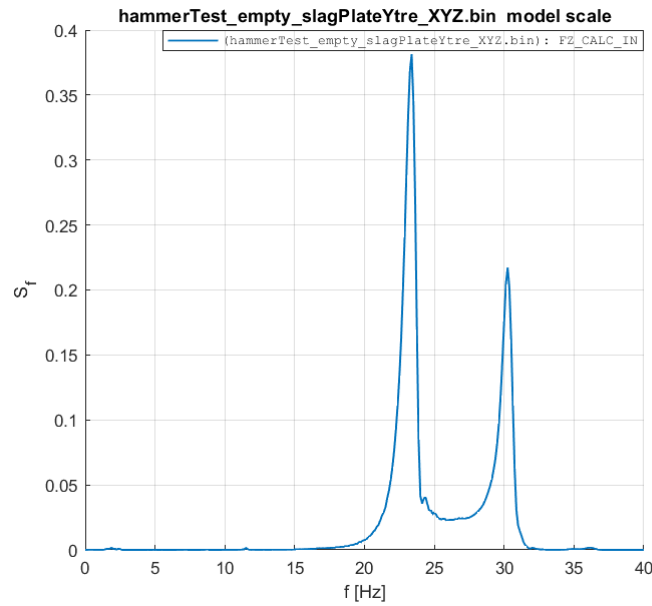


Figure J.14: Spectral analysis of the forces in Z-direction of the inner plate without models, when striking the outer plate in X-direction.

### J.1.15 Striking the outer plate in Y-direction, measuring at outer plate

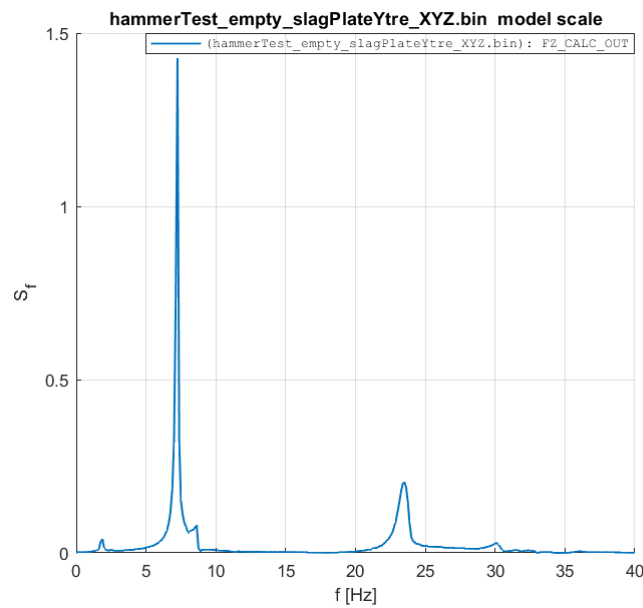


Figure J.15: Spectral analysis of the forces in Z-direction of the outer plate without models, when striking the outer plate in Y-direction.

---

### J.1.16 Striking the outer plate in Y-direction, measuring at inner plate

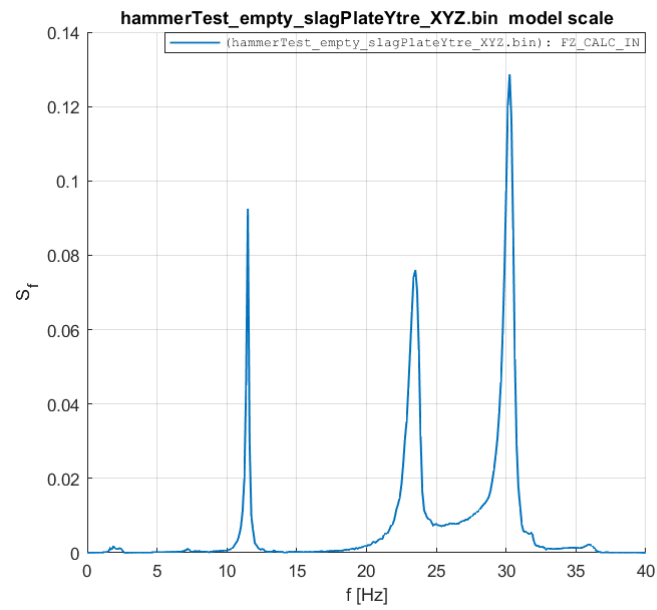


Figure J.16: Spectral analysis of the forces in Z-direction of the inner plate without models, when striking the outer plate in Y-direction.

---

## J.2 Plates with small-draft models

### J.2.1 Striking the tank in Y-direction

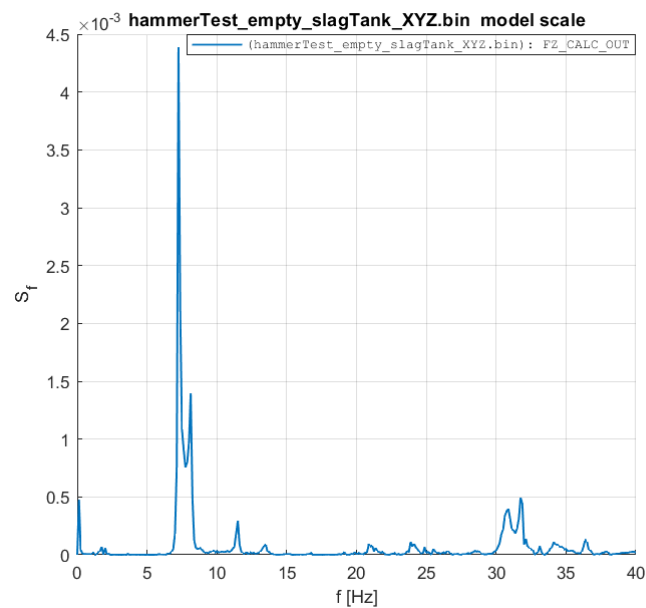


Figure J.17: Spectral analysis of the forces in Z-direction of the outer plate with small-draft models, when striking the tank in Y-direction.

### J.2.2 Striking the tank in Z-direction

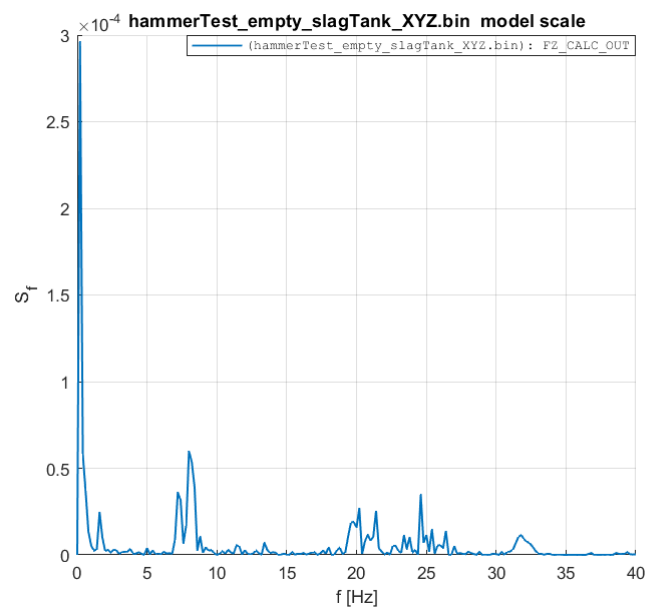


Figure J.18: Spectral analysis of the forces in Z-direction of the outer plate with small-draft models, when striking the tank in Z-direction.

---

### J.2.3 Striking the stronghold in X-direction

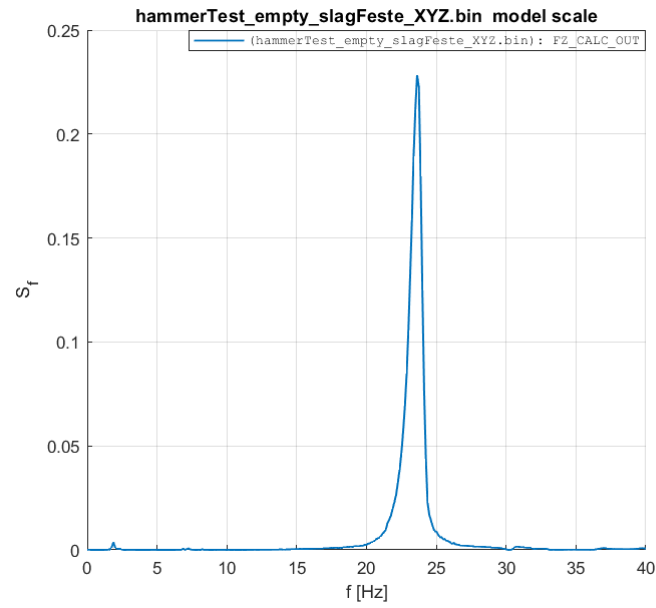


Figure J.19: Spectral analysis of the forces in Z-direction of the outer plate with small-draft models, when striking the stronghold in X-direction.

### J.2.4 Striking the stronghold in Y-direction

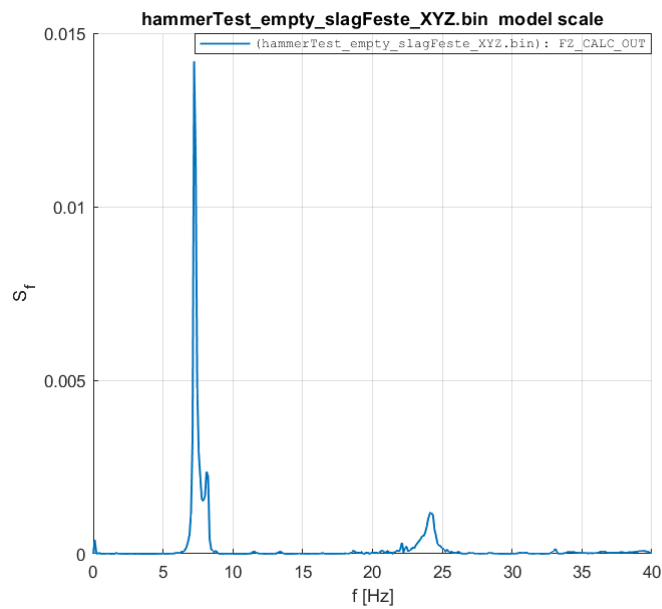


Figure J.20: Spectral analysis of the forces in Z-direction of the outer plate with small-draft models, when striking the stronghold in Y-direction.

---

## J.2.5 Striking the stronghold in Z-direction

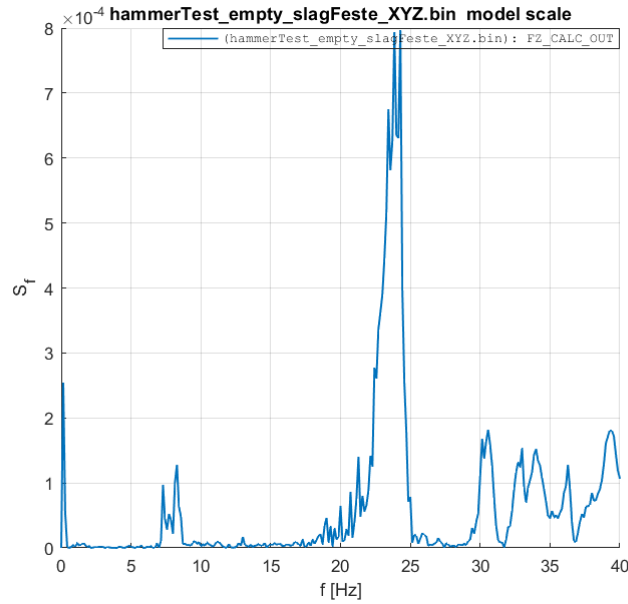


Figure J.21: Spectral analysis of the forces in Z-direction of the outer plate with small-draft models, when striking the stronghold in Z-direction.

## J.2.6 Striking the rig in X-direction

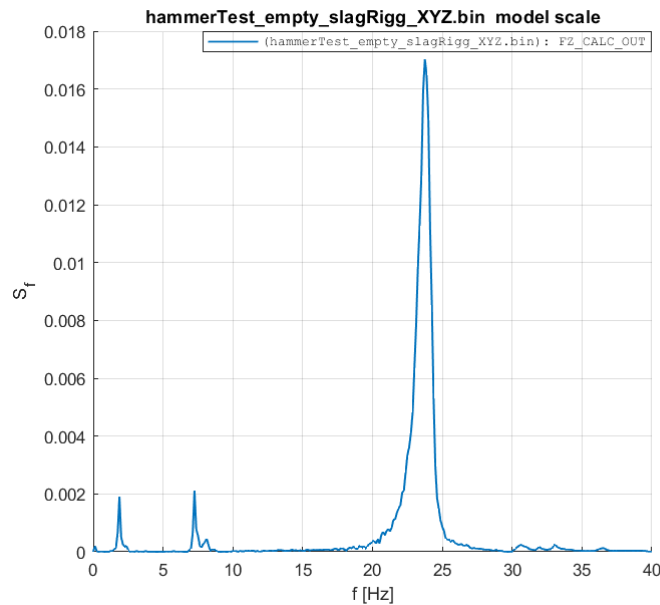


Figure J.22: Spectral analysis of the forces in Z-direction of the outer plate with small-draft models, when striking the rig in X-direction.



---

## J.2.7 Striking the rig in Y-direction

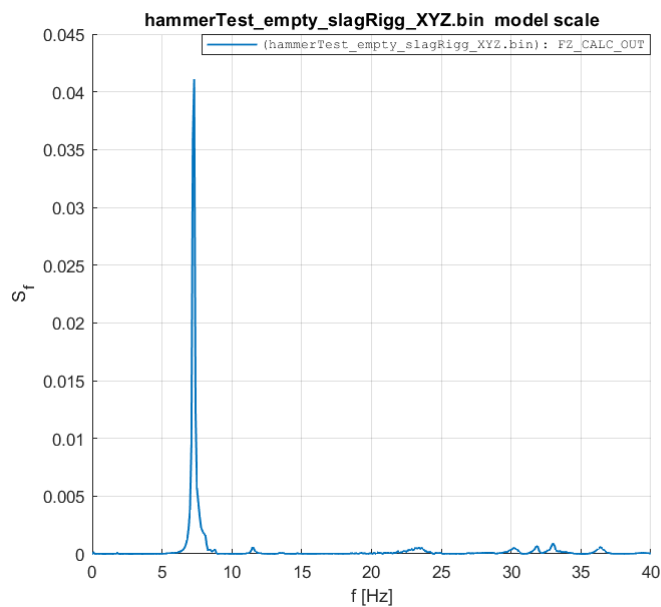


Figure J.23: Spectral analysis of the forces in Z-direction of the outer plate with small-draft models, when striking the rig in Y-direction.

## J.2.8 Striking the rig in Z-direction

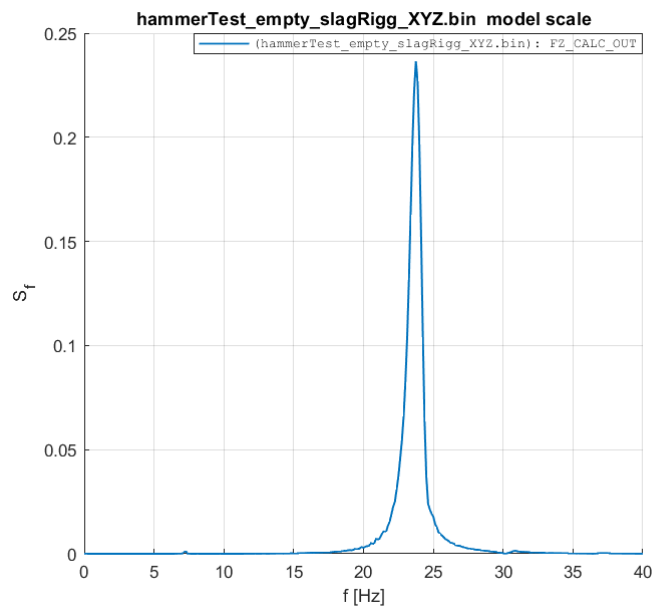


Figure J.24: Spectral analysis of the forces in Z-direction of the outer plate with small-draft models, when striking the rig in Z-direction.

---

### J.2.9 Striking the inner plate in X-direction, measuring at outer plate

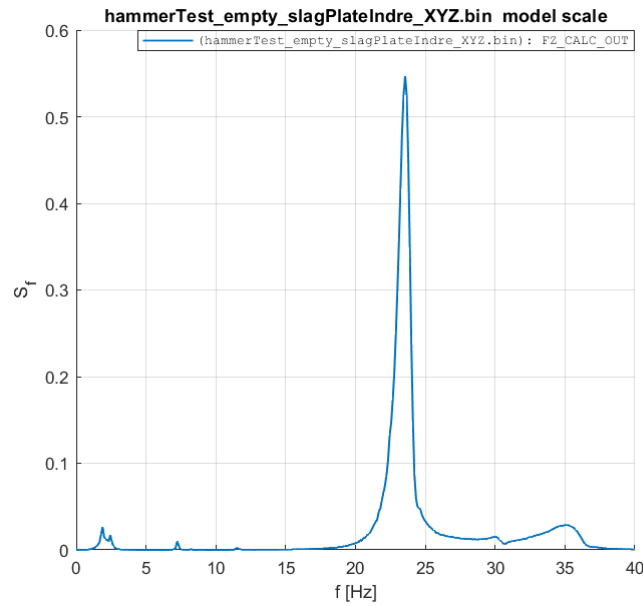


Figure J.25: Spectral analysis of the forces in Z-direction of the outer plate with small-draft models, when striking the inner plate in X-direction.

### J.2.10 Striking the inner plate in X-direction, measuring at inner plate

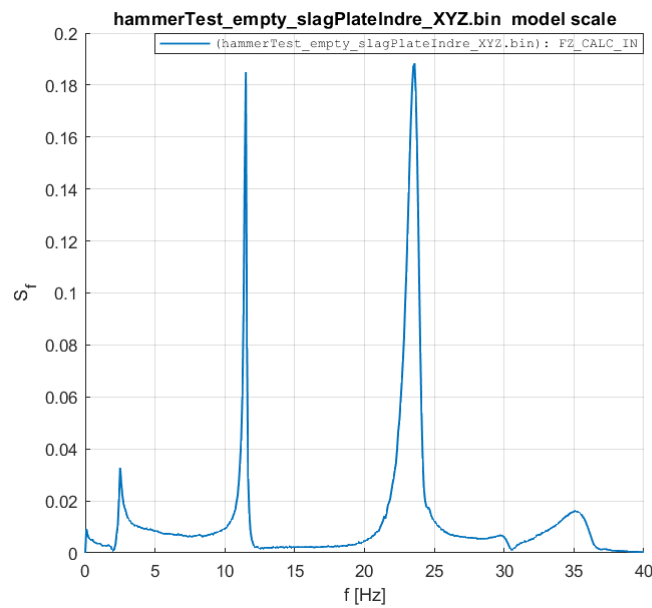


Figure J.26: Spectral analysis of the forces in Z-direction of the inner plate with small-draft models, when striking the inner plate in X-direction.

---

### J.2.11 Striking the inner plate in Y-direction, measuring at outer plate

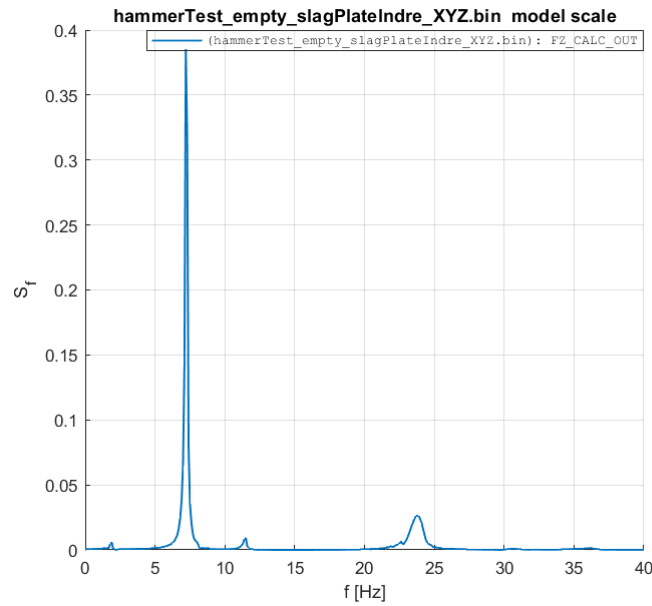


Figure J.27: Spectral analysis of the forces in Z-direction of the outer plate with small-draft models, when striking the inner plate in Y-direction.

### J.2.12 Striking the inner plate in Y-direction, measuring at inner plate

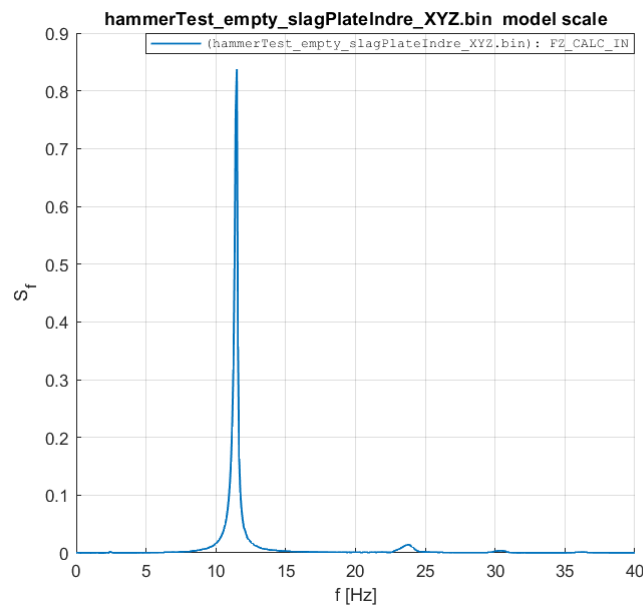


Figure J.28: Spectral analysis of the forces in Z-direction of the inner plate with small-draft models, when striking the inner plate in Y-direction.

---

### J.2.13 Striking the outer plate in X-direction, measuring at outer plate

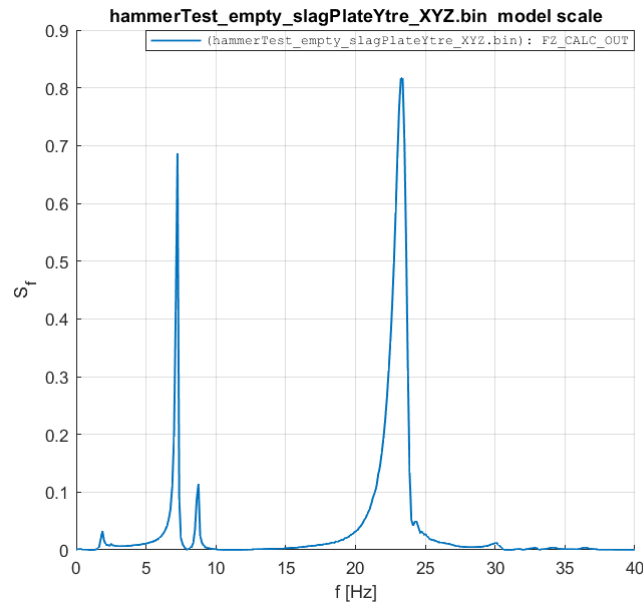


Figure J.29: Spectral analysis of the forces in Z-direction of the outer plate with small-draft models, when striking the outer plate in X-direction.

### J.2.14 Striking the outer plate in X-direction, measuring at inner plate

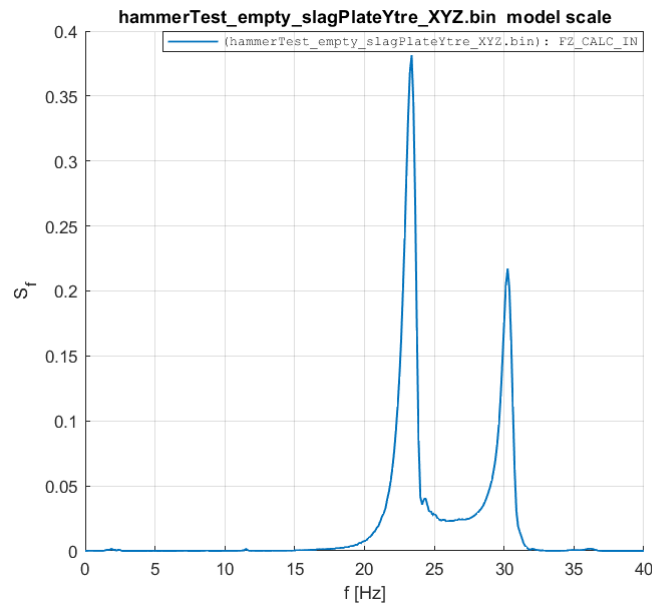


Figure J.30: Spectral analysis of the forces in Z-direction of the inner plate with small-draft models, when striking the outer plate in X-direction.

---

### J.2.15 Striking the outer plate in Y-direction, measuring at outer plate

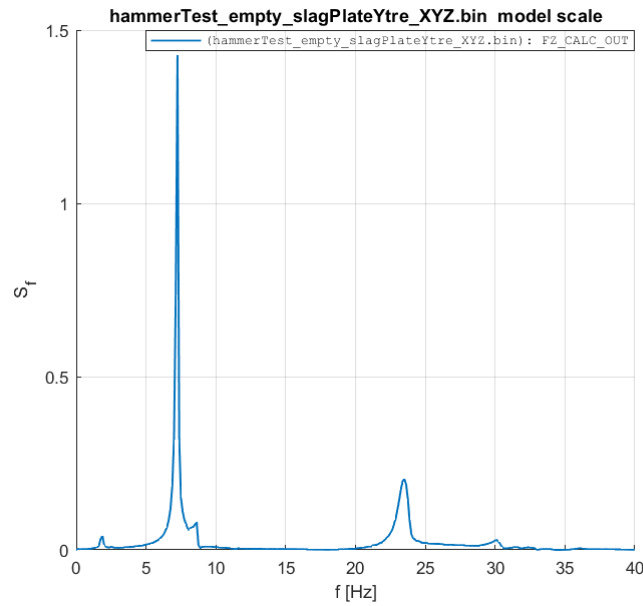


Figure J.31: Spectral analysis of the forces in Z-direction of the outer plate with small-draft models, when striking the outer plate in Y-direction.

### J.2.16 Striking the outer plate in Y-direction, measuring at inner plate

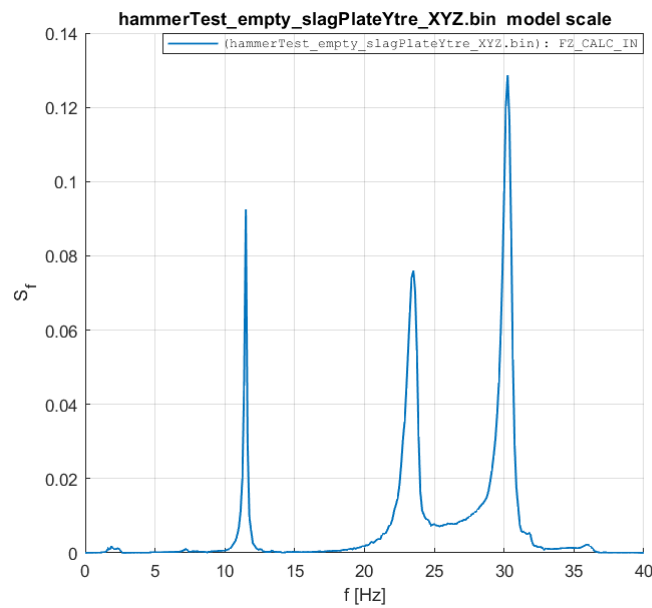


Figure J.32: Spectral analysis of the forces in Z-direction of the inner plate with small-draft models, when striking the outer plate in Y-direction.

---

## J.3 Plates with large-draft models

### J.3.1 Striking the tank in Y-direction

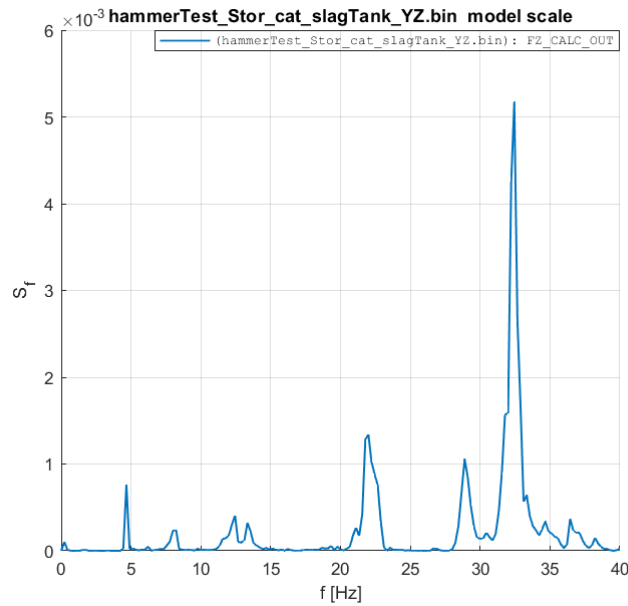


Figure J.33: Spectral analysis of the forces in Z-direction of the outer plate with large-draft models, when striking the tank in Y-direction.

### J.3.2 Striking the tank in Z-direction

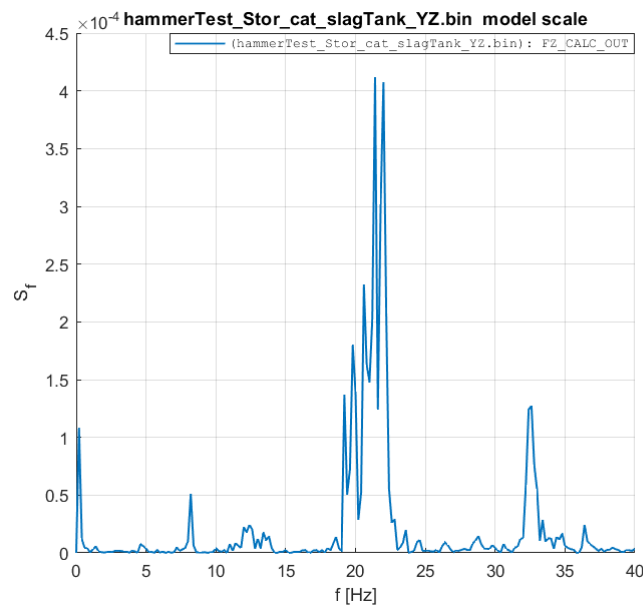


Figure J.34: Spectral analysis of the forces in Z-direction of the outer plate with large-draft models, when striking the tank in Z-direction.

---

### J.3.3 Striking the stronghold in X-direction

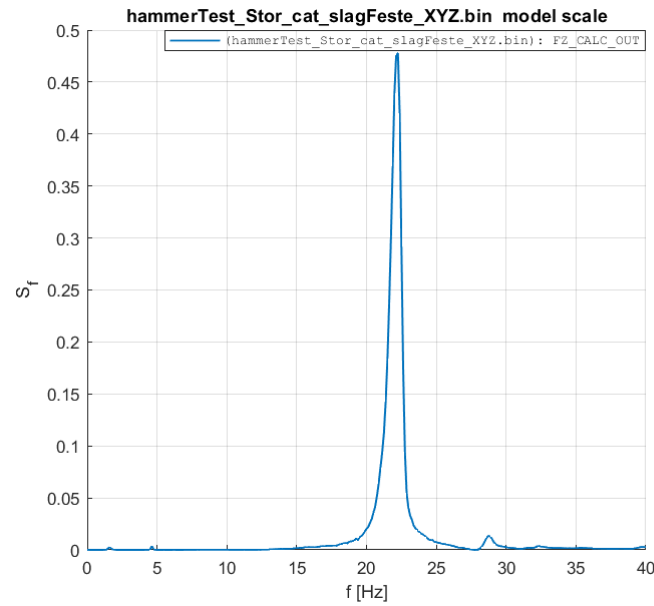


Figure J.35: Spectral analysis of the forces in Z-direction of the outer plate with large-draft models, when striking the stronghold in X-direction.

### J.3.4 Striking the stronghold in Y-direction

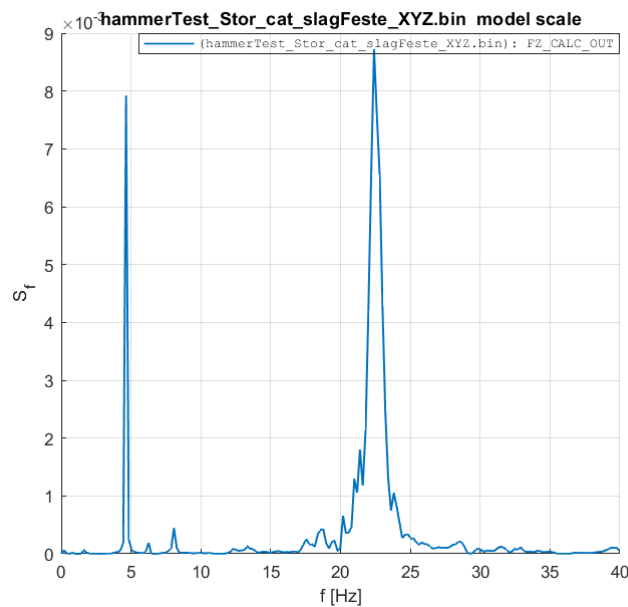


Figure J.36: Spectral analysis of the forces in Z-direction of the outer plate with large-draft models, when striking the stronghold in Y-direction.

---

### J.3.5 Striking the stronghold in Z-direction

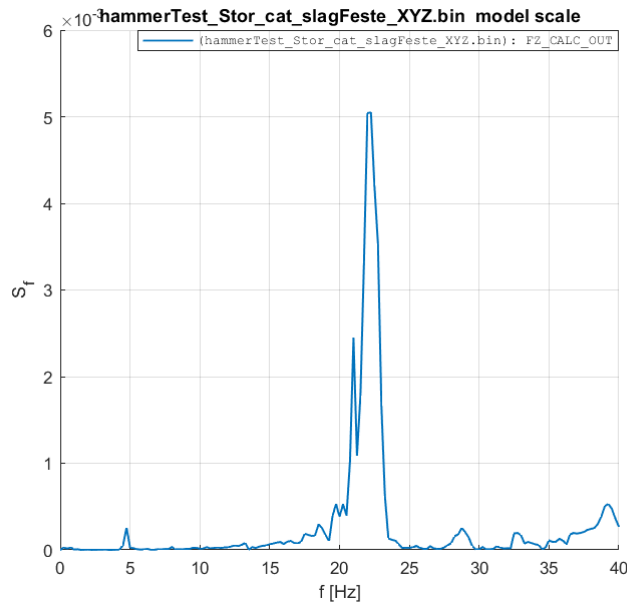


Figure J.37: Spectral analysis of the forces in Z-direction of the outer plate with large-draft models, when striking the stronghold in Z-direction.

### J.3.6 Striking the rig in X-direction

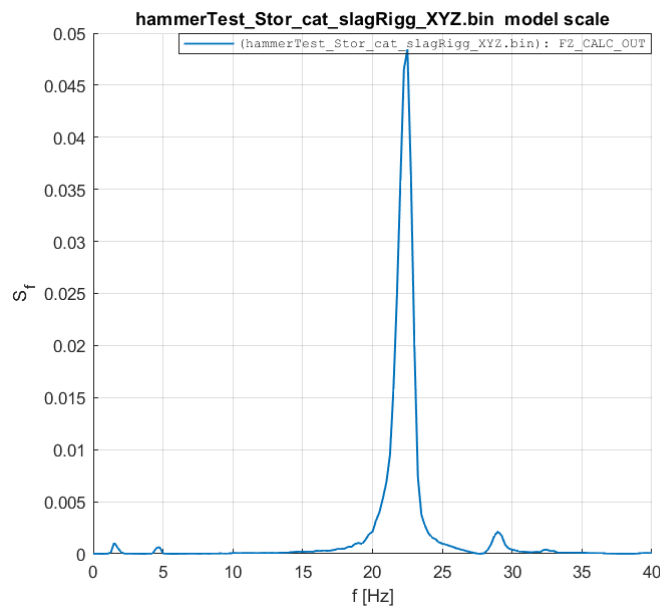


Figure J.38: Spectral analysis of the forces in Z-direction of the outer plate with large-draft models, when striking the rig in X-direction.



---

### J.3.7 Striking the rig in Y-direction

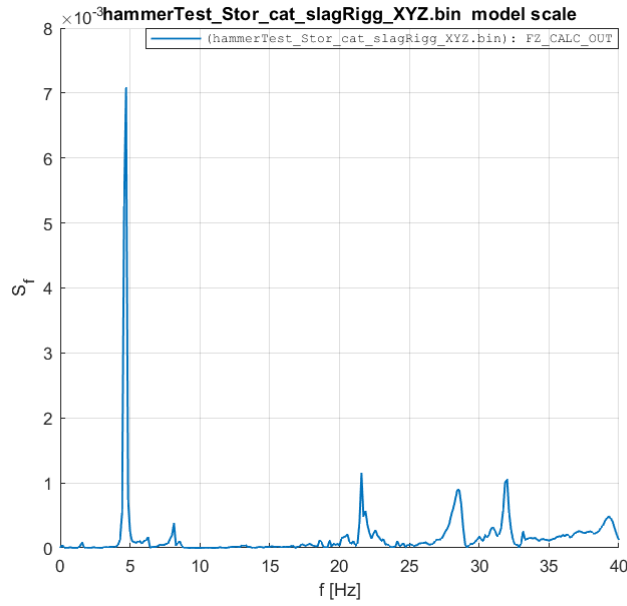


Figure J.39: Spectral analysis of the forces in Z-direction of the outer plate with large-draft models, when striking the rig in Y-direction.

### J.3.8 Striking the rig in Z-direction

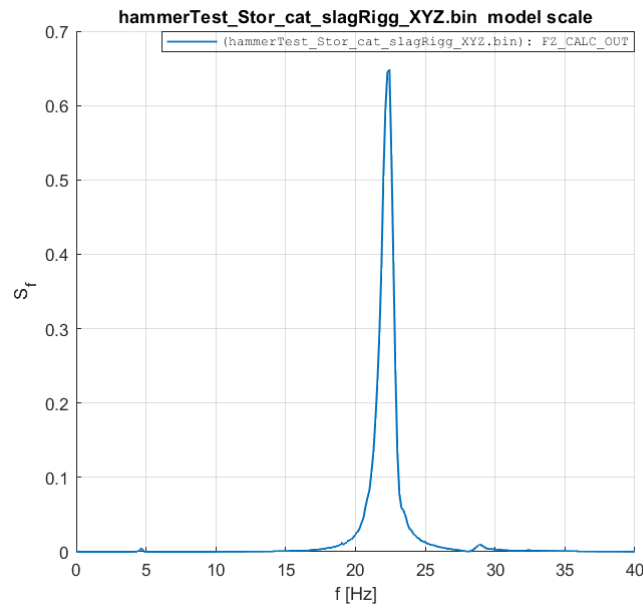


Figure J.40: Spectral analysis of the forces in Z-direction of the outer plate with large-draft models, when striking the rig in Z-direction.

---

### J.3.9 Striking the inner plate in X-direction, measuring at outer plate

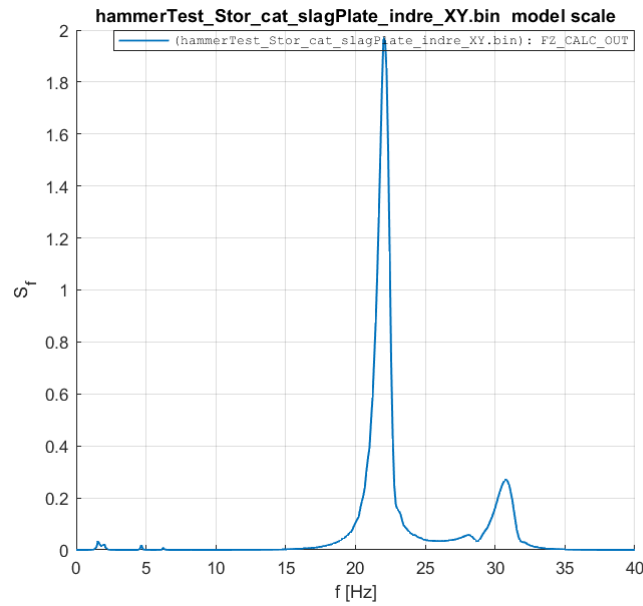


Figure J.41: Spectral analysis of the forces in Z-direction of the outer plate with large-draft models, when striking the inner plate in X-direction.

### J.3.10 Striking the inner plate in X-direction, measuring at inner plate

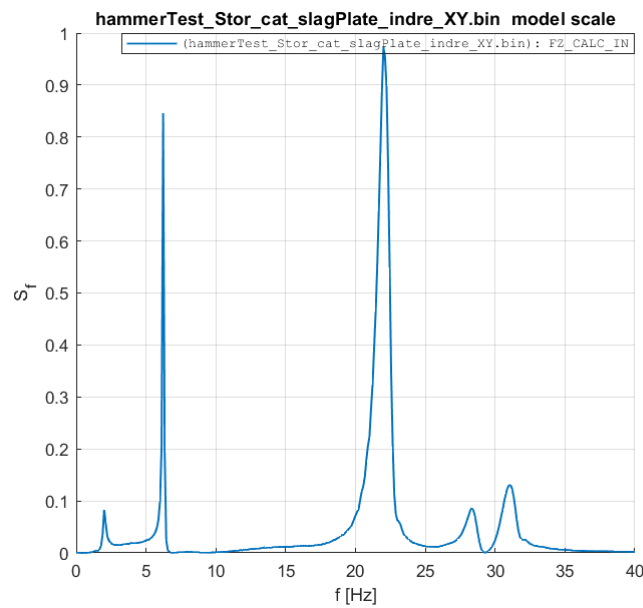


Figure J.42: Spectral analysis of the forces in Z-direction of the inner plate with large-draft models, when striking the inner plate in X-direction.

---

### J.3.11 Striking the inner plate in Y-direction, measuring at outer plate

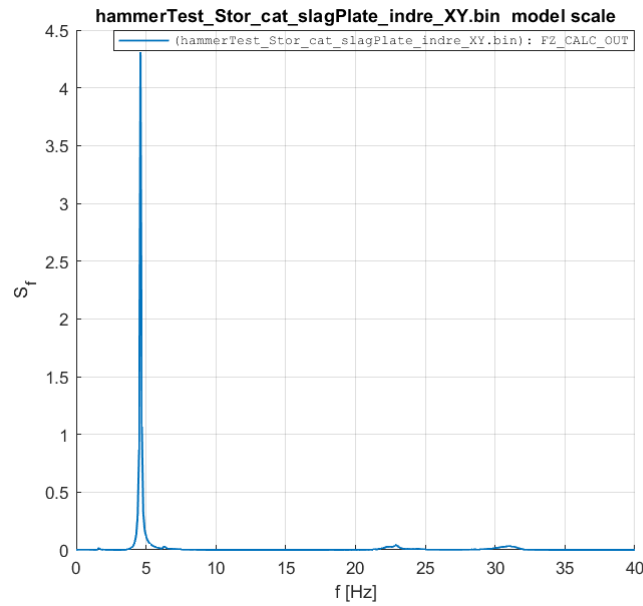


Figure J.43: Spectral analysis of the forces in Z-direction of the outer plate with large-draft models, when striking the inner plate in Y-direction.

### J.3.12 Striking the inner plate in Y-direction, measuring at inner plate

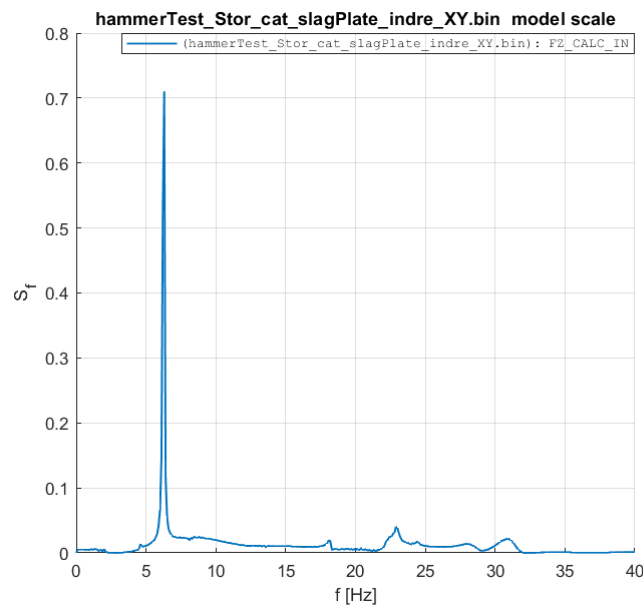


Figure J.44: Spectral analysis of the forces in Z-direction of the inner plate with large-draft models, when striking the inner plate in Y-direction.

---

### J.3.13 Striking the outer plate in X-direction, measuring at outer plate

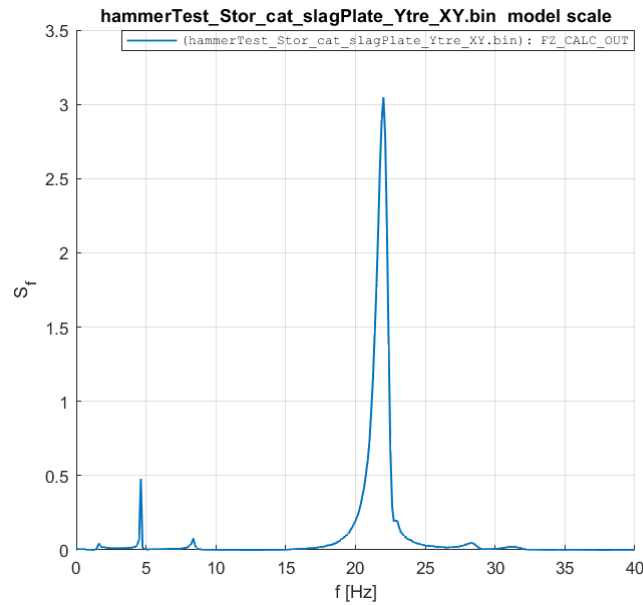


Figure J.45: Spectral analysis of the forces in Z-direction of the outer plate with large-draft models, when striking the outer plate in X-direction.

### J.3.14 Striking the outer plate in X-direction, measuring at inner plate

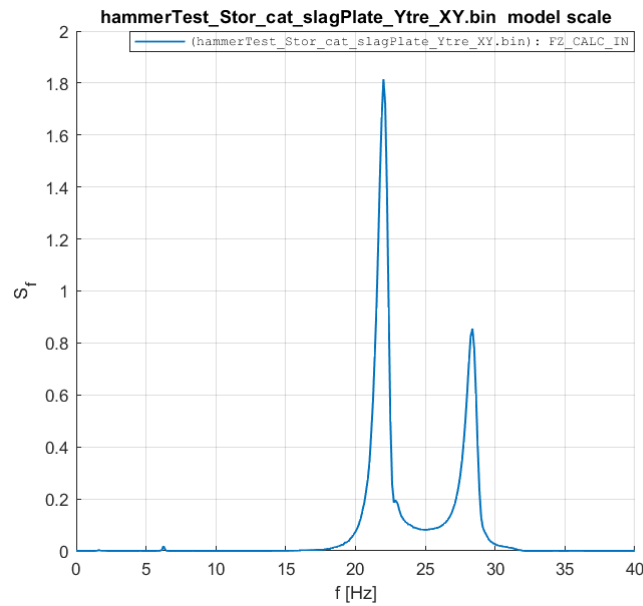


Figure J.46: Spectral analysis of the forces in Z-direction of the inner plate with large-draft models, when striking the outer plate in X-direction.

---

### J.3.15 Striking the outer plate in Y-direction, measuring at outer plate

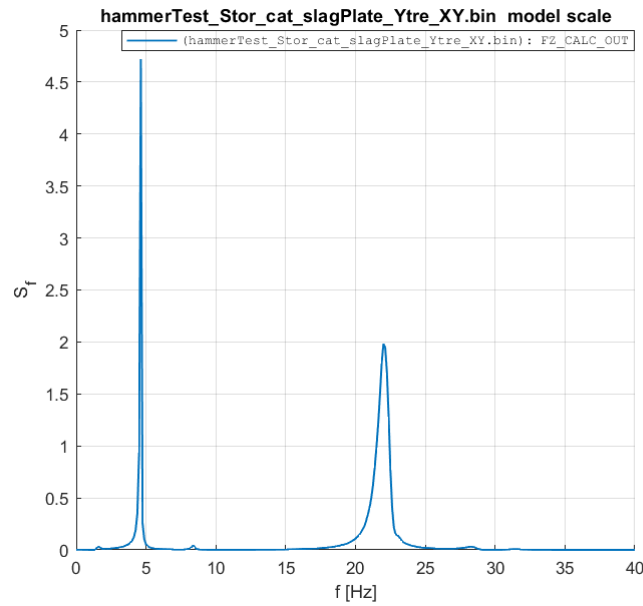


Figure J.47: Spectral analysis of the forces in Z-direction of the outer plate with large-draft models, when striking the outer plate in Y-direction.

### J.3.16 Striking the outer plate in Y-direction, measuring at inner plate

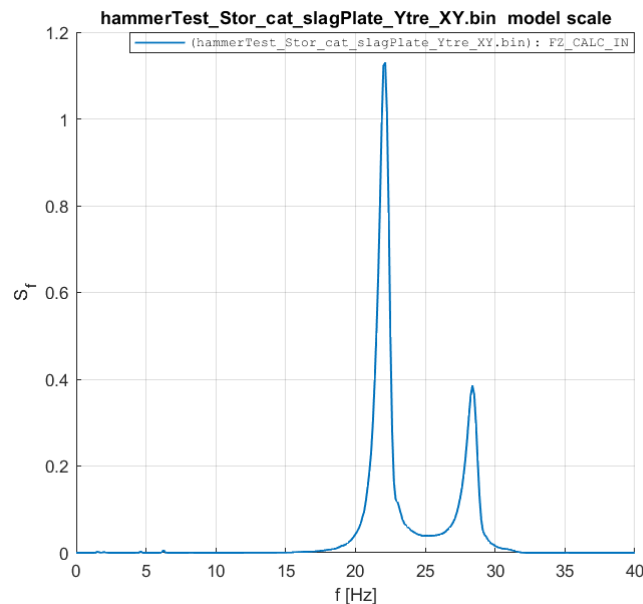


Figure J.48: Spectral analysis of the forces in Z-direction of the inner plate with large-draft models, when striking the outer plate in Y-direction.



 **NTNU**

Norwegian University of  
Science and Technology